UNIVERSITÀ DEGLI STUDI DI PADOVA

Dipartimento di Fisica e Astronomia "Galileo Galilei"

Master Degree in Astrophysics and Cosmology

Final Dissertation

Emission from neutron stars with condensed surface: a systematic analysis

Thesis supervisor:
Prof. Roberto Turolla
Thesis co-supervivor:
Prof. Roberto Taverna

Candidate:
Camilla Missoni
Student ID 2054779

Academic Year 2022/2023

Abstract

Amongst the various classes of neutron stars, magnetars are the ones hosting the strongest magnetic fields. The study of their emission in the X-ray band allows to achieve unprecedented knowledge of the physical processes in the presence of ultra-strong magnetic fields. In particular, magnetar emission is expected to be highly polarized. Thanks to the recently launched Imaging X-ray Polarimetry Explorer (IXPE), polarimetric measurements in the X-ray band are finally possible, opening an entirely new window in the investigation of magnetar physics, as well as allowing an insight into QED effects in strong magnetic fields such as vacuum birefringence.

The focus of this thesis is on the emission properties of neutron stars with a condensed surface. Magnetic condensation is expected to set in for large enough fields ($B > 10^{13} - 10^{14}$ G) and relatively low temperatures ($T < 1$ keV), such as those found in magnetars. In this work we present a systematic analysis of the radiation emitted from sources with a condensed surface, accounting for different geometries and physical parameters.

Contents

Chapter 1

Introduction

Neutron stars are the remnants of massive stars in the mass range $10 \lesssim M/M_\odot \lesssim 25$ and they are characterized by a mass of $M_{\rm NS} \sim 1$–$2\,M_\odot$ and a radius of $R_{\rm NS} \sim 10$–13 km. They can be classified into different categories, depending on their observed properties.
Magnetars are a peculiar class of young neutron stars, characterized by ultra-strong magnetic fields. Such strong magnetic fields imply that the phenomenon of magnetic condensation could appear in these sources. In fact, the electrons are confined in the transverse direction, so that the Coulomb forces that bind them along the field direction are more effective, resulting in the atoms attaining a cylindrical structure. The atoms consequently form molecular chains in the field direction through covalent bonding; these then combine with one another and eventually constitute a three-dimensional condensate. This phase transition depends on the cohesive properties of the matter: in the case in which the requirements are met, which is expected for some sources, the gaseous atmosphere condensates and the star is said to be "naked", affecting the spectral properties of the radiation emitted from it. The emission properties of the condensed surface can be studied considering the two limiting cases of free ions, neglecting the Coulomb interactions between them, and fixed ions, neglecting the ion motion. The real emission properties are likely to lie between these two limits.

The presence of strong magnetic fields also implies that the thermal radiation from these sources is expected to be polarized, due to the effects of the magnetic field on the properties of both the plasma and the vacuum in which the photons propagate. Quantum electro-dynamics (QED) has an important impact on the polarization of the sources, depending on the viewing geometry and the surface emission mechanism.
One of the predictions of QED is vacuum birefringence. In the presence of strong magnetic fields, photons are expected to be linearly polarized in two normal modes (extraordinary and ordinary, depending on the orientation of the electric field vector with respect to the magnetic field at the emission point and the propagation direction). However, the magnetic field is thought not to be uniform on the surface, so that, even if the radiation is highly polarized at emission, the polarization degree is observed to be much lower, since the polarization direction is generally different from point to point on the surface: the observer then collects polarized photons from all possible directions, resulting in an overall depolarized radiation. If the magnetic field is of the order of the quantum critical field, the QED effect of vacuum birefringence becomes relevant and the vacuum behaves as a birefringent medium: as a consequence, the direction of the polarization vector of the photons changes throughout the propagation and adapts to the varying magnetic field direction, maintaining the polarization mode of emission. This process takes place up to very large distances, i.e. the so-called adiabatic radius, from the star surface: at these distances, the magnetic field likely becomes more uniform, so that the observed polarization degree can be sizeable. The detection of polarization in the thermal emission from a source is then extremely valuable, since it can provide the first ever experimental evidence of vacuum birefringence. At the same time, the polarization observables can be compared with emission models and help in uncovering the physical conditions of the star surface and atmosphere, as well as of the geometry of the source. Furthermore, polarization measurements can provide an independent estimate of the magnetic field strength and topology. Neutron stars, and particularly magnetars, are the most promising targets for these polarimetric studies, which received new impulse from the launch of IXPE, the first mission devoted to the study of polarimetry in

the X-ray range (2–8 keV).

The goal of this thesis is to offer a systematic analysis of the properties of radiation emitted from highly-magnetized neutron stars endowed with a ultra-strong magnetic field, accounting for different geometrical and physical parameters, in order to better understand the effects of magnetic condensation and vacuum birefringence on the emission properties.

The thesis is organized as follows. Chapter 2 gives a general description of neutron stars and their classification, focusing on the properties of magnetars. Chapter 3 describes the effects of a strong magnetic field on the state of matter and on the interaction and propagation of radiation both in a plasma and in vacuum. In particular, Section 3.1 analyzes more in detail the physics of magnetic condensation and its effects on the emitted radiation, while Section 3.2 deals with the polarization of radiation and the effects of QED. Chapter 4 describes the numerical tools used in this work to compute the spectral and polarimetric properties of the emission from condensed surfaces in the presence of a strong magnetic field (Section 4.1) and to perform the systematic study of the outgoing radiation from these sources (Section 4.2). Chapter 5 presents the main results. Chapter 6 offers a summary of the work and discusses future perspectives.

Chapter 2

Neutron stars

Neutron stars (NSs) are the extremely compact and dense remnants which form at the endpoint of the evolution of massive stars with $10 \lesssim M/M_\odot \lesssim 25$. They were theoretically conceived in the 1930s by Baade and Zwicky [1]. Their mass is in the range ~ 1–$2\,M_\odot$, with $M_{\rm min} \sim 0.1\,M_\odot$ for the star to be hydrostatically stable, and their radius is $R_{\rm NS} \sim 10$–13 km. The values of M and R are derived from the hydrostatic equilibrium equation for a given equation of state $p(\rho, T)$, where p, ρ and T are respectively the pressure, the energy density and the temperature.

The pressure profile of neutron stars is given by the Tolman-Oppenheimer-Volkoff (TOV) equation:

$$\frac{dp(r)}{dr} = -\frac{Gm(r)}{c^2 r^2}\left(\rho + \frac{p}{c^2}\right)\left(1 + \frac{4\pi r^3 p}{c^2 m(r)}\right)\left(1 - \frac{2G}{c^2}\frac{m(r)}{r}\right)^{-1}, \tag{2.1}$$

with G the gravitational constant, $m(r) = 4\pi \int_0^r \rho(r') r'^2 dr'$ the rest mass and energy contained inside the radius r, and c the speed of light. On the right-hand side, the term in front would give the classical equation for hydrostatic equilibrium, the first two terms in parenthesis are the special relativistic corrections, and the last term is the correction for general relativity (GR). The system of equations is closed by considering the equation of state: it is then possible to build a model for the neutron star.

The observed emission of neutron stars can be explained by considering a rapid rotation (small period P) and a strong magnetic field (B). These quantities can be estimated by considering the conservation of the angular momentum and of the flux, respectively. Considering the collapse from a massive star to a neutron star, the momentum conservation is defined by:

$$I_* \omega_* = I_{\rm NS} \omega_{\rm NS}\,, \tag{2.2}$$

with I the moment of inertia and $\omega = 2\pi/P$ the angular velocity, from which we get the ratio of the periods:

$$\frac{P_{\rm NS}}{P_*} = \frac{M_{\rm NS} R_{\rm NS}^2}{M_* R_*^2} \sim 10^{-6}\,; \tag{2.3}$$

considering $P_* \sim 10^6$ s and $R_* \sim 10^6$ km typical values for the neutron star progenitor, then $P_{\rm NS} \sim 10^{-3}$ s, so the neutron star rotates very fast.
On the other hand, for the magnetic flux conservation:

$$\begin{aligned} &B_* \,\Delta\Omega\, R_*^2 \sim B_{\rm NS}\,\Delta\Omega\, R_{\rm NS}^2\,, \\ &\frac{B_{\rm NS}}{B_*} \sim \left(\frac{R_*}{R_{\rm NS}}\right)^2 \sim 10^{10}\,, \end{aligned} \tag{2.4}$$

where $\Delta\Omega$ is the solid angle. Considering $B_* \sim 10^2$ G, then $B_{\rm NS} \sim 10^{12}$ G, which is indeed very strong. Such strong magnetic fields induce an electromagnetic effect of slowing down the rotation of the neutron star ($\dot{P}{>}0$) through angular momentum losses.

The power emitted from rapidly rotating stars with strong magnetic fields is given by the magnetic equivalent of the Larmor formula for accelerated particles:

$$\mathcal{P} = \frac{2|\ddot{m}|^2}{3c^3}\,, \tag{2.5}$$

where $\vec{m}$ is the magnetic moment and $|\ddot{\vec{m}}| = \omega^2 |\vec{m}| \sin\alpha_B$, with α_B the angle between B and the rotation axis. From this we find the luminosity:

$$L = \frac{\sin^2 \alpha_B \, B_0^2 \, \omega^4 R^6}{6c^3} \,, \tag{2.6}$$

with $B_0 = 2m/R^3$.
The rotational energy is given by:

$$E_{\rm rot} = \frac{1}{2} I \omega^2 \sim \frac{4\pi^2}{5} \frac{MR^2}{P^2} \,, \tag{2.7}$$

assuming a homogeneous sphere, $I = 2/5\, MR^2$. Then:

$$\frac{dE_{\rm rot}}{dt} = I\omega\dot{\omega} = \frac{8\pi^2}{5} \frac{MR^2}{P^3} \dot{P} \,. \tag{2.8}$$

Equating the expressions 2.6 and 2.8, we find a relation between the magnetic field strength and the period and period derivative:

$$B_0 = \left(\frac{3c^3 I}{8\pi^2 R^6} \right)^{1/2} (P\dot{P})^{1/2} \simeq 3.2 \times 10^{19} \, (P\dot{P})^{1/2} \, \mathrm{G} \,. \tag{2.9}$$

The period evolution is in general described through the function $P(t) = ct^{1/n-1}$, where $n = \omega\ddot{\omega}/\dot{\omega}^2$ is the *braking index*, equal to 3 for magneto-dipolar braking. From this expression we can evaluate the period derivative:

$$\dot{P} = \frac{P}{t(n-1)} \,, \tag{2.10}$$

from which we define the *characteristic age*:

$$\tau = \frac{1}{n-1} \frac{P}{\dot{P}} = \frac{P}{2\dot{P}} \,, \tag{2.11}$$

where the last equality holds for $n = 3$. This estimate of the age of neutron stars is only an approximation and is usually a poor proxy of the star's true age.
From Equations 2.9 and 2.11 one can see that P and $\dot{P}$ are important quantities in order to determine the properties of neutron stars, such as age and magnetic field strength. For this reason, NSs are usually classified as a function of their values of period and period derivative: Figure 2.1 shows a P-$\dot{P}$ diagram for the different classes of neutron stars, which will be described below. The diagram also presents the lines at which B and τ of Equations 2.9 and 2.11 are constant.

Observations of neutron stars, made predominantly in the radio wavelengths of the electromagnetic spectrum, result in remarkably different properties. We can therefore speak of *NS-zoo* as the ensemble of the various classes in which neutron stars have been divided into.

Radio pulsars (PSRs) are defined by regular pulses in the radio band and are the most populated out of all the NS classes. These source are also known as **rotation-powered pulsars (RPPs)**, given that their power is a consequence of the loss of rotational energy. Concurrently, some PSRs have a pulsating activity observable beyond the radio wavelength (mostly in the X-rays, like PSR J1420-6048, [3]): the name *rotation-powered* therefore gives a more precise description of the class. The periods of the pulses are in the range $P \sim 0.001$–8 s, while the magnetic field strength is $B \sim 10^8$–10^{13} G. Measurements of P and $\dot{P}$ are obtained from the arrival time of the radio pulses. The X-ray emission is divided into thermal and non-thermal contributions. The thermal emission, which is common to almost all NSs (except for the very cool ones), is either due to the residual cooling after the NS-formation, or to surface reheating caused by currents in the magnetosphere. On the other hand, non-thermal emission, usually described with a power law, comes from the magnetosphere and is normally more highly-pulsed than in the thermal case.
There also exists a sub-class of RPPs, the **millisecond pulsars (MSPs)**, which have periods shorter than ~ 20 ms and $B \lesssim 10^{10}$ G, and are believed to be powered by accretion phenomena. These sources have a different evolutionary history and are thought to be originated from recycling processes.

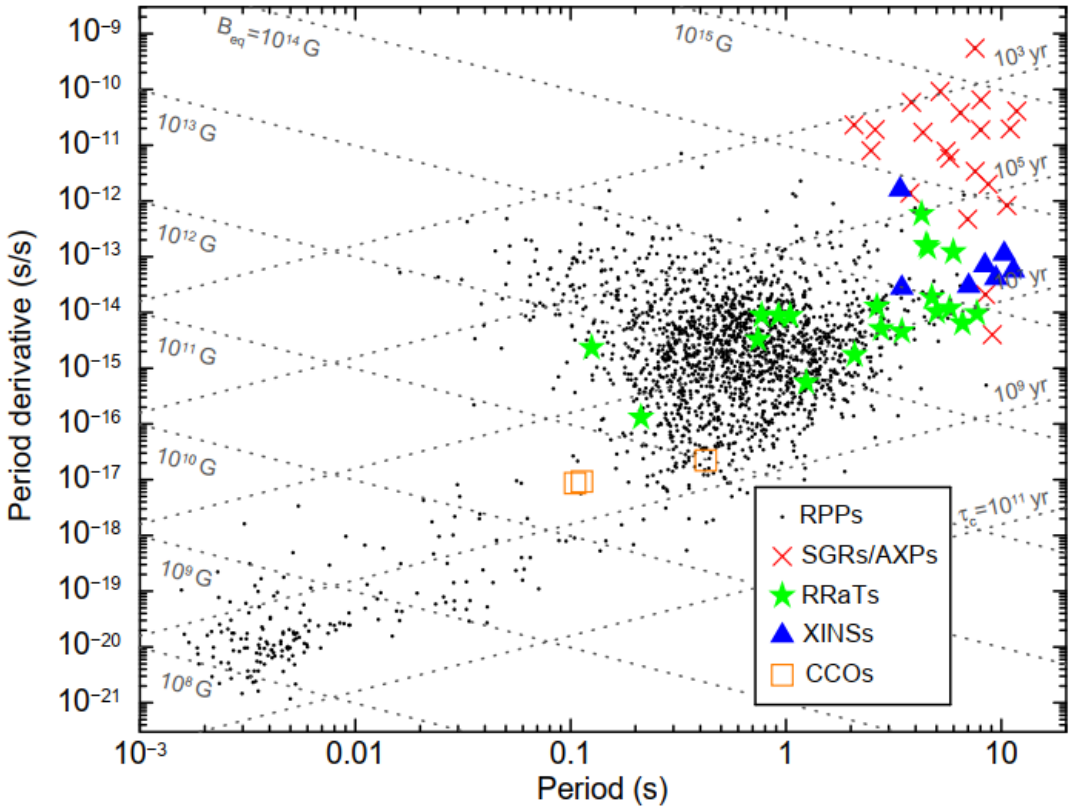

Figure 2.1: P-$\dot{P}$ diagram for about 2300 neutron stars, from [2]. The superimposed dotted lines show the loci of constant characteristic age τ and surface dipolar magnetic field B.

Rotating radio transients (RRATs), discovered relatively recently [4], are also rotationally-powered, but do not have an observable periodic emission. They instead show unpredictable short radio bursts: from their phase constancy it is possible to deduce an underlying periodicity, possibly making these sources an extreme form of RPPs, although this conclusion is still highly uncertain due to contrasting observations. There are roughly 70 RRATs known, whose periods and magnetic field strengths are generally higher than average, with $P \sim 1$–10 s and $B \sim 10^{12}$–10^{13} G.

Magnetars, young isolated NSs, are characterized by outbursts in X- and soft-γ rays. They are powered by the decay of a very large magnetic field with strength $B \sim 10^{14}$–10^{15} G, derived from the long periods ($P \sim 2$–12 s) and large period derivatives ($\dot{P} \sim 10^{-13}$–10^{-10} s s^{-1}). Historically, magnetars were divided into two groups, **anomalous X-ray pulsars (AXPs)** and **soft-gamma repeaters (SGRs)**, according to how they were first discovered. The luminosity of these sources, mostly in the X-rays (~ 1–100 keV), is usually larger than that of rotation-powered NSs of similar age, meaning that some heating mechanism has to be present in magnetars, either in the core or in the crust. There are currently about 30 known objects in this class [5], some of which also show a counterpart in IR and/or optical, but there could also be a large unseen population of quiescent magnetars, justified by the discovery of magnetars with transient properties [6]. A more detailed description of magnetars is given below, in Section 2.1.

High-B rotation-powered pulsars have spin-down inferred magnetic field $B > 4 \times 10^{13}$ G. Their X-ray properties are similar to those of lower-B RPPs of the same age, but at the same time they could be interpreted as those of quiescent magnetars: these sources could therefore constitute a link between magnetars and RPPs.

There is a peculiar group of isolated neutron stars (INSs), called **X-ray dim isolated neutron stars (XDINSs)** or ***magnificent seven***, since only seven sources of this type have been observed up to now, all in proximity of the Solar System ($\lesssim 500$ pc). Their spectra are purely thermal and no radio counterpart has been observed. They are characterized by $P \sim 1$–10 s and $B \sim 10^{12}$–10^{13} G, from which a large characteristic age (Equation 2.11) is derived: this, alongside the fact that the spectra are thermal,

may suggest that XDINSs are aged magnetars.

Central compact objects (CCOs), named after their location at the center of supernova remnants, are quite young and have peculiar properties. The periods are short ($P \sim 0.1$–0.4 s) and the magnetic field strength can be as low as $B \sim 10^{10}$ G: for this reason, they were also known as *anti-magnetars*. There are currently 8 known CCOs, with no observed counterpart beyond the X-rays. Like XDINSs, they are radio-quiet and their emission is powered by the release of residual heat.

Figure 2.1 shows the position of the different classes of NSs in the P-$\dot{P}$ diagram, summarizing the properties described above.
There seems to be a problem with the birth rates of neutron stars: those of RRATs and XDINSs, unless they are overestimated, are thought to be even higher than that of PSRs, but the sum of the birth rates of all the classes cannot exceed the core-collapse supernova rate in the Galaxy. This means that there must be some evolutionary links between the different types of NSs, as mentioned above, unless there are other channels for neutron star formation that we are not aware of. This issue has not been completely understood, yet.

The internal structure of neutron stars comprises of:

- Core
  - inner: the density is $\rho \gtrsim 5.6 \times 10^{14}\,\mathrm{g\ cm^{-3}}$ and the composition is uncertain, with possibly exotic particles being present;
  - outer: the density is $1.4 \times 10^{14}\,\mathrm{g\ cm^{-3}} \lesssim \rho \lesssim 5.6 \times 10^{14}\,\mathrm{g\ cm^{-3}}$ and the extension is of several kilometers, with most of the mass of the NS contained in it. The outer core is approximated by models of matter made of neutrons, protons, electrons and muons ($npe\mu$, [7]);
- Crust: divided into inner and outer, with a total thickness of $\sim$1 km and a crystalline lattice;
- Envelope: made of degenerate electrons and neutrons, with neutron-rich nuclei, i.e. the number of neutrons exceeds that of protons, which are arranged in a crystalline lattice. The outer part of the envelope is the gaseous atmosphere.

The magnetic field plays a relevant role in shaping the emission properties of neutron stars. As suggested by [8], the magnetic field could either be already there at the birth of the NS (*fossil field*, inherited from the progenitor and amplified during the collapse), or be generated by a convective dynamo in the first ~ 10 s of the proto-neutron star's life. The internal field configuration is believed to be produced by a superposition of current systems in the core and in the crust, with different contributions for each class of NSs. The field is then thought to experience a strong decay over time, after which the period freezes at an asymptotic value, dependent on the initial B, the NS mass and the crust resistivity. This decay is shown in Figure 2.2.
If there indeed exists an evolutionary link between the various classes of NSs, the evolution of B is necessary to explain why the magnetic field strength decreases for younger sources. At the same time, magnetar emission is powered by magnetic energy, so that a dissipation of the magnetic field is expected. The evolution of the magnetic field occurs through a series of quasi-equilibrium states [10]:

$$\frac{\partial \vec{B}}{\partial t} = -\nabla \times \left(\frac{c^2}{4\pi\sigma}\nabla \times \vec{B}\right) + \nabla \times \left(-\frac{\vec{j}}{n_e e} \times \vec{B}\right) + \nabla \times (\vec{v_a} \times \vec{B})\,, \tag{2.12}$$

with n_e the electron number density and e the electron charge. The three terms on the right-hand side are, respectively:

- Ohmic diffusion, with $\sigma = j/E$ the electric conductivity and $\vec{j}$ the electric current density;
- Field advection with Hall drift: B is carried by the electron fluid, which drifts with respect to the ions with velocity $-\vec{j}/n_e e$;
- Ambipolar diffusion: B and the electron-proton fluid drift with respect to neutrons with velocity $\vec{v_a}$, which is a dissipative process.

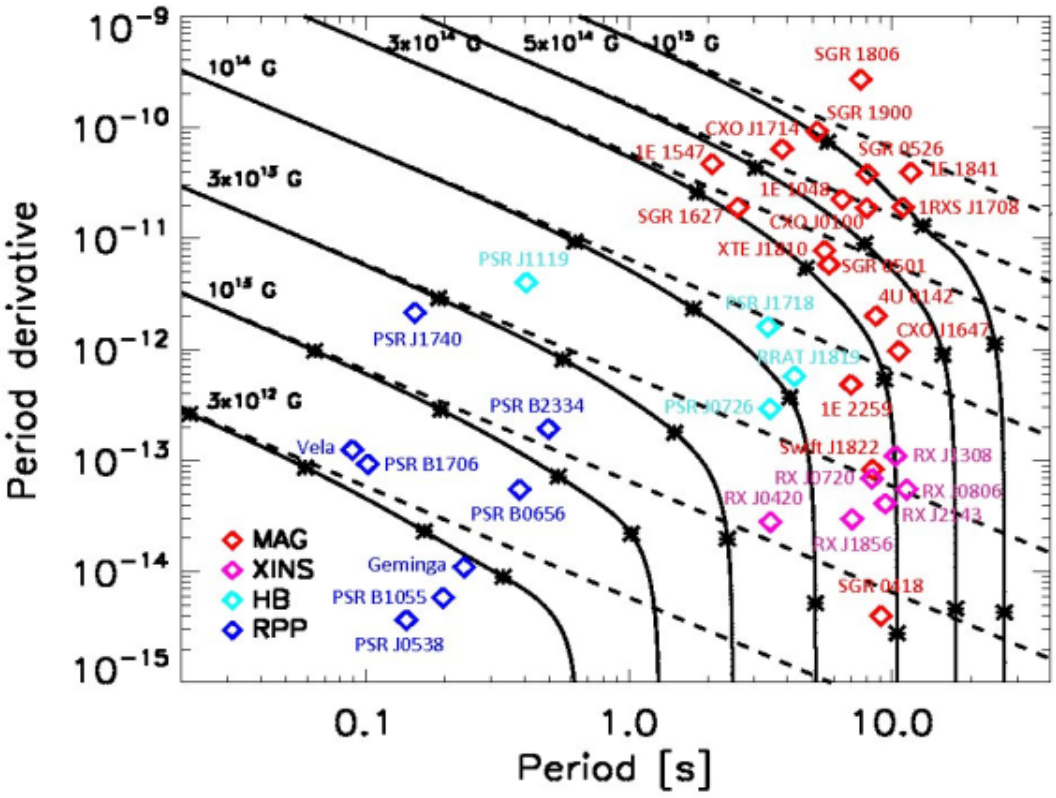

Figure 2.2: Modified P-$\dot{P}$ from [9] containing the evolutionary tracks of neutron stars with different initial magnetic fields, where the asterisks indicate the real ages of the sources: 10^3 yr, 10^4 yr, 10^5 yr, 5×10^5 yr.

Neutron stars are born hot, with temperature $T \sim 10^{11}$ K, but reach $\sim$ few$\times10^9$ K shortly after. The cooling that NSs experience is due to an initial phase of neutrino losses (with a rate proportional to the ratio of total neutrino luminosity and heat capacity, [11]), lasting $\sim 10^5$ years, followed by photon cooling once the neutrino energy losses become smaller than the energy lost through electromagnetic radiation, as an effect of the lower temperature.

An important progress in the study of neutron stars has been made by considering the magnetic and the thermal evolutions as coupled [12]. Implementing the theory of NSs with magneto-thermal evolutionary models might help in explaining the great diversity in the properties of the various classes: macrophysical quantities such as initial B, mass and envelope composition (which is unknown) could play a pivotal role in governing the evolution of neutron stars.

2.1 Magnetars

We now consider the class of magnetars a little more in detail. They are young neutron stars with great variability, resulting in bursts of different duration and energy outputs, across the electromagnetic spectrum: in particular, X- and soft-γ rays are the ranges in which they were first discovered in 1979. Apart from the X-ray pulses, some magnetars are also observable in the optical and radio bands: the radio activity might constitute a link between these sources and high-B radio pulsars, even though the properties are quite different. *Glitches* are also quite frequent: they are sudden spin-ups, after which the star can recover partially, fully or, in some cases, it can over-recover, producing an overall spin-down effect. *Anti-glitches* have also been observed in some cases, but their origin remains debated.
Originally, the class of magnetars was divided into two groups of sources, as mentioned above. SGRs

were initially linked to gamma-ray bursts (GRBs), but they have softer spectra and a repeated emission which is not observed in GRBs. After the discovery of AXPs in the 1980s, it took many years for them to be related to SGRs: it is now widely accepted that the two do not represent distinguished classes, but rather one unique category, that is indeed that of magnetars. This was first postulated by [13].
The emission of magnetars is powered by the decay of a very large internal magnetic field, and not by rotation as is the case of many other NS classes, hence the name. The external field of these sources can be inferred from the spin-down, a consequence of magnetic dipole braking consisting in electromagnetic losses due to a rotating dipole, through the formula defined in the previous section (Equation 2.9). It is still unclear as to why B is so high.
The spin-down occurs on a timescale of roughly a few thousand of years, reinforcing the idea that these objects are rather young: this is confirmed by their confinement in the galactic plane, as well as by their association, in some cases, with supernova remnant shells. The spin-down luminosity $\dot{E}$ (Equation 2.8) is usually lower than the quiescent X-ray luminosity, supporting the fact that the source of energy in magnetars is not rotation. Other aspects in support of this are the already-mentioned large periods and period derivatives; moreover, the evidence that magnetars are isolated NSs indicates that the energy is not powered by accretion either.

Spectra

Magnetars can be divided into two categories, depending on their variability.
Transient magnetars, 11 known [9], are very faint when in quiescence. In many cases, the discovery of the source follows a sudden increase of the flux, $\sim$ 10–1000 times over the quiescent level, a phenomenon known as *outburst*, along with the emission of short bursts. The X-ray spectrum is thermal (a power-law tail is observed in some sources), with the temperature being much higher with respect to the quiescent phase: this is probably due to a heat deposition in a region of the surface, which then cools down and shrinks with time. Some transient sources have been observed in radio: in this case, the flux decays much in the same way as in the X-rays, but with a delayed onset. Contrarily to radio-silent magnetars, some transient sources have $L_{\rm X}<\dot{E}$.
Persistent magnetars, on the other hand, have a high X-ray luminosities, with $L_{\rm X} \sim 10^{31}$–10^{36} erg/s in the energy range $\sim$ 0.2–10 keV. Their spectra can be modelled by different components: absorbed blackbody (BB, $kT \sim 0.1$–0.5 keV) plus power law (PL, $\Gamma \sim 2$–4), two blackbodies or, much more rarely, two power laws. The BB component (thermal), dominant at lower energies, is believed to originate from the cooling surface of the star, while the non-thermal part (PL) is thought to be due to magnetospheric effects of reprocessing of the thermal photons through resonant up-scattering, as will be discussed below. For sources with a larger spin-down rate, or equivalently a stronger B, the photon index Γ that defines the trend of the PL decreases. Also, some sources show different power laws in the soft- and in the hard-X ray ranges. An example of spectral fit can be seen in Figure 2.3. All of the models cited above are phenomenological and should not be considered as a measurements of the physical properties of the star, but they indicate that the emission is not described by a simple planckian. The study of spectra can help retrieving information on the surface magnetic field and on its evolution, as well as on the chemical composition of the NS.

Burst activity

The bursting activity of magnetars, observed in hard-X and soft-γ rays, comprises of different types of events.

Short bursts are the most common ones, lasting between few milliseconds and few seconds and reaching peak luminosities of $L \sim 10^{36}$–10^{42} erg/s. Their light curves are generally single-peaked, with a slower decay with respect to the rise, but their shape is variable. The spectra, for which many models have been used, are harder than the persistent emission. Sources for which a statistical analysis of the bursting activity has been made, i.e. which emitted a sufficient number of bursts, show a power-law distribution of the burst fluences. Short bursts sometimes come in bunches, defining the so-called *burst forests* or *burst storms*.

Giant flares are very rare (only 3 known cases up to now, [9]) and are extremely bright, reaching an energy release of $E \sim 10^{47}$ erg. Their overall properties are similar: the initial hard peak of $\sim$ 0.1–1 s is

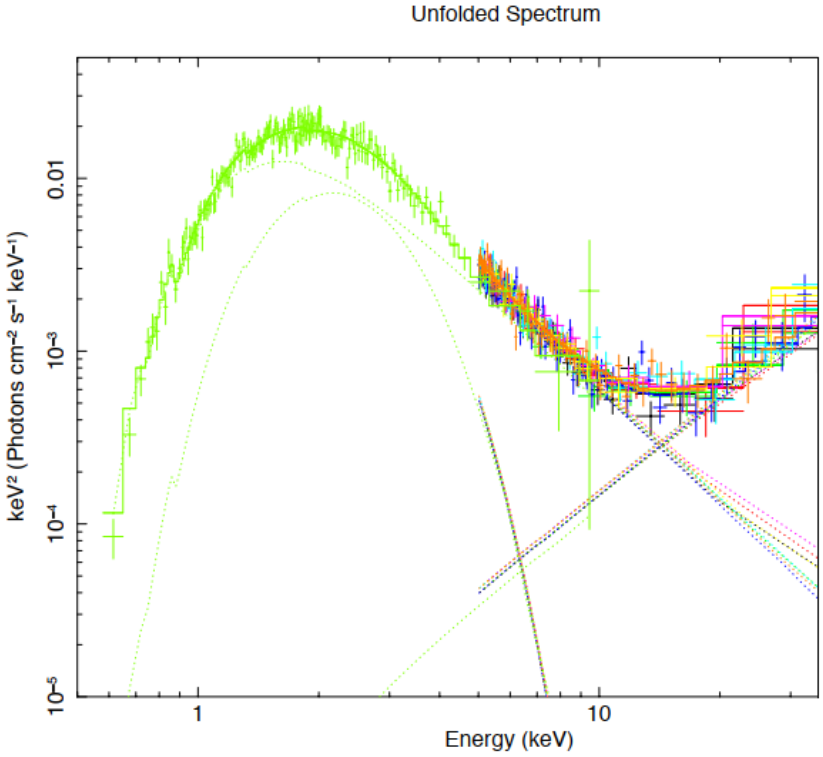

Figure 2.3: Example of broadband phase-averaged X-ray spectrum of the magnetar 1E 2259+586, taken from [14]. The spectrum was obtained from combined observations with Swift and NuSTAR. The figure shows a best-fit model consisting of an absorbed blackbody plus two power-law components.

followed by an extended decaying tail of ∼hundreds of seconds and by an abrupt end.
The tails are characterized by quasi-periodic oscillations (QPOs), induced by seismic vibrations of the star. These are composed of torsional shear oscillations of the crust and torsional Alfvén oscillations of the liquid core: they are thought to be coupled, therefore we speak of global magneto-elastic oscillations. The discovery of QPOs opened up the field of asteroseismology, the study of stellar interiors in neutron stars: this can lead to constrain the interior magnetic field strength and geometry.

The trigger mechanism of bursts is still unclear. Few possibilities have been formulated, but it is still uncertain whether they each apply to different types of bursts or if there is a common origin. The trigger theories are:

- Internal instability and magnetic reconfigurations give a sudden ejection of magnetic energy from the core to the magnetosphere;
- Gradual deformation of the magnetosphere which builds up free magnetic energy;
- Rapid plastic deformation of the crust as a consequence of the decay of the core field.

Magnetic field

The combination of magneto-hydrodynamics effects and neutrino cooling results in the presence of a liquid core with a radius of roughly 10 km and a solid crust $\sim$ 1 km thick [14]. The interior of the NS is an excellent conductor and the magnetic field is therefore frozen in the electron fluid, evolving slowly. This evolution depends on density and temperature and it is described by Equation 2.12. As a consequence, crustal stresses gradually accumulate, originating surface motions and eventually bursts. The field is believed to reside in the crust, in the core or both.

The internal field has to be strong enough to sustain the magnetar activity and its topology must allow the magnetic energy to be released: an active magnetar thus needs to have both a toroidal and a poloidal component in the magnetic field, which are thought to be approximately of the same order. The crustal field decays substantially over $\sim 10^3$–10^5 yr.
The external field of persistent magnetars is thought to be not a simple dipole. The magnetosphere is expected to be locally twisted, even though global twists are usually considered for simplicity, caused by magnetally-induced crustal displacements. Thus, the field is non-potential ($\nabla \times B \neq 0$), requiring supporting currents to flow along the closed field lines. The twist produces an external toroidal component B_ϕ. In order to have the potential drop needed to accelerate the charges for the conduction currents, the twist decays, with a typical timescale of ∼1 yr. An axisymmetric globally-twisted dipole magnetic field, in polar components, is given by:

$$\vec{B} = (B_r,\, B_\theta,\, B_\phi) = \frac{B_P}{2}\Big(\frac{r}{R_{\rm NS}}\Big)^{-p-2}\left[-f',\ \frac{pf}{\sin\theta},\ \sqrt{\frac{Cp}{p+1}}\frac{f^{1+\frac{1}{p}}}{\sin\theta}\right], \tag{2.13}$$

with r the radial coordinate and θ the magnetic colatitude; the derivative $'$ is made with respect to $\cos\theta$, B_P is the polar value of the magnetic field, $R_{\rm NS}$ is the radius of the neutron star, C is a constant and $0 < p \leq 1$ is the radial index, which fixes the amount of shear of the field. Also, $f = f(\cos\theta)$ satisfies the Grad-Shafranov equation

$$(1-\mu^2)f'' + p(p+1)f + Cf^{1+2/p} = 0\,. \tag{2.14}$$

Both f and the eigenvalue C are easily computed once p is fixed. Varying the radial index results in a sequence of magnetostatic and globally-twisted dipole fields: $p = 0$ gives a split monopole; as p increases the ratio of B_ϕ with respect to the other components decreases; $p = 1$ corresponds to an untwisted dipole. The twist angle, defining the amount of angular displacement of a field line from the northern to the southern magnetic emispheres, is given by:

$$\Delta\phi_{_{N-S}} = \lim_{\theta\to 0} 2\int_\theta^{\pi/2} \frac{B_\phi}{B_\theta}\frac{d\theta}{\sin\theta} = \left[\frac{C}{p(1+p)}\right]^{1/2} \lim_{\theta\to 0}\int_\theta^{\pi/2}\frac{f^{1/p}}{\sin\theta}\,d\theta\,, \tag{2.15}$$

As explained in [15], in [16] and in [17], the magnetospheric plasma is characterized by resonant Compton scattering (RCS): a particle of charge Ze and mass m, with resonant frequency $\omega_c = ZeB/mc$ (the so-called *cyclotron frequency*), scatters a photon of frequency ω. In the specific case of magnetars, the density of charged particles flowing along the closed lines of the external field is sufficient for them to scatter at the resonance to higher energies, with this effect being more efficient as the twist angle increases. This has an observable effect on the thermal spectra, in the appearance of a hard tail at high energies (PL component).

Polarization

This topic will be discussed in more detail in Section 3.2. Due to a quantum electro-dynamics effect, photons in a strongly magnetized environment are expected to be linearly polarized in two normal modes: the ordinary (O), with the electric field parallel to the plane of photon propagation ($\vec{k}$) and $\vec{B}$, and the extraordinary (X), with $\vec{E}$ perpendicular to the k-B plane.

The X-ray radiation from magnetars is expected to be polarized, because [9]:

- for the radiative processes, the cross sections involving X-polarized photons are suppressed with respect to the ones for the O-mode photons, for $\omega < \omega_c$, so thermal photons can have an intrinsic polarization, depending on the emission model;
- the photons which propagate in a strongly magnetized vacuum maintain the same polarization mode (*adiabatic evolution*) up to a distance greater than the radius at which scatterings occur ($\sim 10\,R_{\rm NS}$), meaning that we can treat the effects of QED and RCS separately.

Polarization measurements can help in constraining the physical parameters of the magnetar magnetospheres, with the polarization observables (polarization degree Π_L and polarization angle χ_{pol}) being strongly dependent also on the viewing geometry and on the magnetospheric twist angle.

The study of magnetars is crucial for their relevance to many branches of astrophysics. Future missions will allow a more detailed analysis of the emission of these sources, on a broader electromagnetic spectrum range, thus granting a better understanding of their properties, as well as of many processes in the physics of strong magnetic fields.

Chapter 3

Physics in strong magnetic fields

The physics in strong magnetic fields is described in detail in [18] and [10]; a more recent review is the one by [19].

A useful quantity when describing strong-field environments is the quantum critical field strength,

$$B_{\rm QED} = m_e^2 c^3/e\hbar = 4.414 \times 10^{13}\,{\rm G}\,, \tag{3.1}$$

with m_e the mass of the electron and $\hbar$ the reduced Planck constant. The critical field, that corresponds to the magnetic field at which the electron cyclotron energy $\hbar\omega_c = \hbar eB/m_e c$ equals its rest mass $m_e c^2$. We can define

$$\beta = \frac{B}{B_{\rm QED}} = \frac{\hbar\omega_c}{m_e c^2} \tag{3.2}$$

as a dimensionless magnetic field parameter. When $\beta \gtrsim 1$, such that the electron cyclotron energy exceeds its rest mass, the field is called *superstrong*, profoundly affecting physical processes. Magnetars are the only environment in which these effects can be measured and tested.
The presence of a strong magnetic field affects the radiative processes which occur around neutron stars; besides, B has a robust effect on the thermal structure of NSs. In particular, the envelope experiences an anisotropic heat transport, resulting in a non-uniform surface temperature distribution ($T_{\rm pole} \neq T_{\rm equator}$).

There are physical limits to the value that the magnetic field strength can attain. One of them, as described in [20], is due to the fact that the magnetic pressure in a NS has to be low enough not to blow the star apart, so:

$$\frac{4\pi R^3}{3}\frac{B^2}{8\pi} < \frac{GM^2}{R}\,, \tag{3.3}$$

with the left-hand term being the magnetic energy and the right-hand term the gravitational binding energy. From this one gets the condition $B < 10^{18}$ G.

Charged particles

Considering a uniform magnetic field, the motion of a charged particle (mass m_i and charge e_i) in the classical non-relativistic regime is a helical orbit of radius

$$r = \frac{m_i c v_\perp}{|e_i|B}\,, \tag{3.4}$$

where $v_\perp$ is the particle velocity perpendicular to the direction of B, and frequency ω_c. Moving to a quantum mechanics description, the transverse motion of the particle is quantized in *Landau levels*, with energy

$$E_\perp = \Big(n_{\rm L} + \frac{1}{2}\Big)\hbar\omega_c\,, \tag{3.5}$$

with $n_{\rm L} = 0, 1, 2, ...$, while the longitudinal motion is continuous. The Landau level spacing is the basic energy quantum, equal to the particle's cyclotron energy. The total energy, considering also the

contributions of spin and kinetic energy along the field direction z, is:

$$E_n = \Big(n_{\rm L} + \frac{1}{2}\Big)\hbar\omega_c + \frac{1}{2}\sigma_{\rm z}\hbar\omega_c + \frac{p_{\rm z}^2}{2m_e}\,, \tag{3.6}$$

with $\sigma_{\rm z} = \pm 1$ representing the spin degeneracy and p_z the momentum along z. For $\beta \gtrsim 1$, the transverse motion is relativistic. However, the non-relativistic treatment still holds as long as the binding energy (i.e. the energy required to remove a particle from a system of particles) is much lower than the rest mass energy, $E_{\rm binding} \ll m_e c^2$, for which the relativistic effects become a small correction. In this case, the particle is in the Landau ground level and the energy is simply $E \sim m_e c^2 + p_{\rm z}^2/2m_e$, with $p_{\rm z} \ll m_e c^2$. Also, the Landau wave function is the same for both the relativistic and the non-relativistic regimes.

Matter

When studying matter in the presence of a strong magnetic field, it is useful to introduce another quantity:

$$B_0 = \frac{m_e^2 e^3 c}{\hbar^3} = \alpha^2 B_{\rm QED} = 2.3505 \times 10^9\,{\rm G}\,, \tag{3.7}$$

where $\alpha = 1/137$ is the fine-structure constant. B_0 is obtained by equating the cyclotron energy to the Hartree unit of energy ($m_e e^4/\hbar^2$, the electric potential energy of the hydrogen atom in its ground state). We then define the dimensionless magnetic field strength:

$$b = \frac{B}{B_0} = 425.44\, B_{12}\,, \tag{3.8}$$

with $B_{12} = B/10^{12}$ G. B is said to be *strong* when $b \gg 1$; in this case the cyclotron energy is much bigger than the Coulomb energy (i.e. the electric potential energy) and B changes the properties of matter. In this conditions, the Coulomb forces are treated as a perturbation of the magnetic forces, and the electron is in the ground Landau level. The electrons are extremely confined in the transverse direction, meaning that the Coulomb forces are more effective in binding them along B. As a result, the atom gains a cylindrical shape. This is crucial in the formation of condensates, as it will be discussed in Section 3.1.

In general, the energy spectrum is specified by the quantum numbers m, measuring the mean transverse separation between the electron and the proton, and ν, which gives the number of nodes in the wavefunction along the B-direction. Let us consider the constituents of matter more in detail:

- H atoms: the electron is in the ground Landau level (*adiabatic approximation*) and the Coulomb potential is a perturbation;
- Hydrogenic atoms (one electron and nuclear charge Z): the adiabatic approximation is valid for $b \gg Z^2$. The energy levels are:

  $$E_m \sim -0.16 A Z^2 \Big[\ln \frac{1}{Z^2}\Big(\frac{b}{2m+1}\Big)\Big]^2\,, \tag{3.9}$$

  where with A the mass number, for $b \gg (2m+1)Z^2$. The overall energy of the atom is approximately given by the sum of all the eigenvalues E_m;
- Multi-e^- atoms: these are the generalization of the hydrogenic atoms, with the electrons at the lowest available energy levels;
- Molecules: they are different from the zero-field case, because the exclusion principle is not valid when B is very large. The spins of the electrons are anti-parallel to B, meaning that to create a H_2 molecule one atom has to be excited to the $m = 2$ state through a small activation energy, with a covalent bond between the two atoms. This is the *tightly-bound state* of the hydrogen molecule. The *weakly-bound state* is given by both electrons in the $m = 0$ state, but one with $\nu = 0$ and the other with $\nu = 1$: in this case, no activation energy is needed for the molecule to be formed. Since the exclusion principle is not valid, H_N molecules can be formed as well: as N increases, the number of the occupied Landau orbitals is larger and the transverse size of the molecule is bigger. The molecular excitation can be:

– electronic, where the electrons occupy orbitals other than $(m_1, m_2) = (0, 1)$;

– aligned vibrational;

– transverse rotational: this is the high-field analogy to the rotational excitation.

Another difference with respect to the zero-field case, for which $\Delta\varepsilon_{\rm el} \gg \hbar\omega_{\rm vib} \gg \hbar\omega_{\rm rot}$, respectively the excitation energies in the electronic, vibrational and rotational cases, is that the excitations in the presence of a strong B-field are all comparable.

Radiative processes

Radiative processes in neutron stars are extensively described in [20] and [10]. In the strong-field scenario ($\beta \gtrsim 1$) a relativistic quantum description of the radiative processes is required, even for non-relativistic particles. The radiative transitions dominate over the collisions, thus controlling the Landau state populations.
What follows is a brief description of the radiative processes taking place in NSs with superstrong magnetic fields.

- Cyclotron absorption: a photon excites a particle to a higher Landau state. The required energy to go from the ground state to the n-th state is:

$$E_n = \frac{(1 + 2n\beta \sin^2\theta)^{1/2} - 1}{\sin^2\theta}\,, \tag{3.10}$$

  with θ the angle between the photon propagation and the field direction. As said above, the radiative processes dominate over the collisional, so the result of this transition is a scattering (second-order) rather than a true absorption (first-order);

- Cyclotron emission: this is the inverse process of the cyclotron absorption, a downward transition between Landau levels. When the particle energy is relativistic, it is called *synchrotron* radiation: in this case the emission is dominated by high harmonics. In the strong-B regime the energy is often radiated in one large transition, rather than through small steps. The cyclotron decay rate is high enough that nearly all the particles reside in the ground state;

- Compton scattering: when a photon is scattered by an electron, which then spontaneously decays. This scattering is called *resonant* if the e^- is excited to a higher Landau state. This process usually dominates over the absorption, where the de-excitation of the electron is collisional. The cross section of this process depends on the photon energy and on the angle of incidence;

- Pair production and annihilation: one-photon production (annihilations) is a first order transition, in which energy and momentum cannot be both conserved: B can absorb (supply) the extra momentum needed by a photon to create (be created by) an $e^- - e^+$ pair. This can take place only in discrete Landau states kinematically allowed by the energy-momentum conservation equations:

$$\begin{aligned} \epsilon &= E_n + E_{n'} \\ \epsilon\,\cos\theta &= p + q \end{aligned} \tag{3.11}$$

  where p is the parallel momentum of the electron and q the one of the positron, $E_n = (1+p^2+2n\beta)^{1/2}$ and $E_{n'} = (1 + p^2 + 2n'\beta)^{1/2}$, with n and n' denoting the Landau states. As the photon energy increases and for larger transverse magnetic field strengths, the probability of the process increases. For $B \gtrsim 10^{12}$ G, the one-photon transition is dominant over the two-photon one;

- Bound pair creation: a photon adiabatically converts into positronium (a hydrogen-like atom composed of an electron and a positron, stable to annihilation), after an evolution through mixed photon-positronium states;

- Photon splitting: this is a third-order process where one photon converts into two or more photons of lower energy and whose rate depends on the magnetic field strength. This transition can come to dominate over the pair production.

- Resonant Bremsstrahlung: this is a cooling process, in which an electron in the ground state is collisionally excited and de-excited through spontaneous emission, producing a cyclotron photon.

Bound pair creation and photon splitting, as well as the one-photon production/annihilation, are processes which do not conserve the energy-momentum in field-free space: the parallel momentum and the total energy are strictly conserved only for strong fields.

Effects of the magnetic field

We define a *magnetic temperature*:

$$T_B = \frac{\Delta E_B}{k_B} = \frac{m_e c^2}{k_B}\left(\sqrt{1+2n\beta+2\beta} - \sqrt{1+2n\beta}\right), \tag{3.12}$$

where the energy difference ΔE_B is between the Landau levels n and $n+1$, and k_B is the Boltzmann constant. When the density reaches the *critical magnetic density* $\rho_B = 7045\, A/ZB_{12}^{3/2}$ g cm^{-3}, then the Fermi temperature is equal to the magnetic one, $T_F = T_B$. The Fermi temperature can be obtained from the Fermi energy, $E_{\rm Fermi} = p_f^2/2m_e$, dividing by the Boltzmann constant. The Fermi momentum p_f can be estimated from $n_e = 2p_f eB/h^2 c$.
Depending on the value of density and temperature, the Landau quantization has different effects on the thermodynamic properties of the gas, both for electrons and for ions:

- $\rho \lesssim \rho_B$ and $T \lesssim T_B$: the electrons are mostly in the ground Landau state. B modifies essentially all the properties of the gas and is called *strongly quantizing*. The quantization becomes important when the cyclotron energy, so the level spacing, is bigger than both the Fermi energy and the thermal energy ($\sim k_B T$);
- $\rho \gtrsim \rho_B$ and $T \lesssim T_B$: the electrons are degenerate and occupy many Landau levels, whose spacing is greater than the thermal width. B is *weakly quantizing* and only slightly affects the bulk properties of the gas;
- $T \gtrsim T_B$ or $\rho \gg \rho_B$: many Landau levels are occupied, with the thermal width larger than their spacing. In this case, the Landau level effects are smeared out: B does not affect the thermodynamic properties and is called *non-quantizing*.

The different regimes just described can be visualized in the diagram of Figure 3.1.

3.1 Condensed surface

Physics of condensed matter

We have already mentioned how, in the case of a strong magnetic field strength, the electrons are extremely confined in the direction transverse to B, making the Coulomb forces more effective in binding them along the field direction. The atoms attain a cylindrical structure and form molecular chains along B, through covalent bonding. These linear chains can then combine with one another through quadrupole-quadrupole interaction, and parallel chains can eventually result in the formation of three-dimensional condensates. The presence of a condensate on a neutron star strongly depends on the cohesive properties of the surface matter, which is expected to be in a condensed state for heavy elements. A condensed surface is formed when the temperature is low enough (this might happen only in certain regions on the surface, e.g. in the case of equatorial belts, which are expected to be colder for a dipole magnetic field) and/or B is strong enough.

In general, magnetized condensed matter (H, He) at zero pressure can be described by the uniform electron gas model. The degenerate electrons are in the ground Landau level when $E_{\rm Fermi} < E_{\rm cyclotron}$. The energy per cell is then defined as:

$$E_S(r_i) = \frac{3\pi^2 Z^3}{8b^2 r_i^6} - \frac{0.9Z^2}{r_i}, \tag{3.13}$$

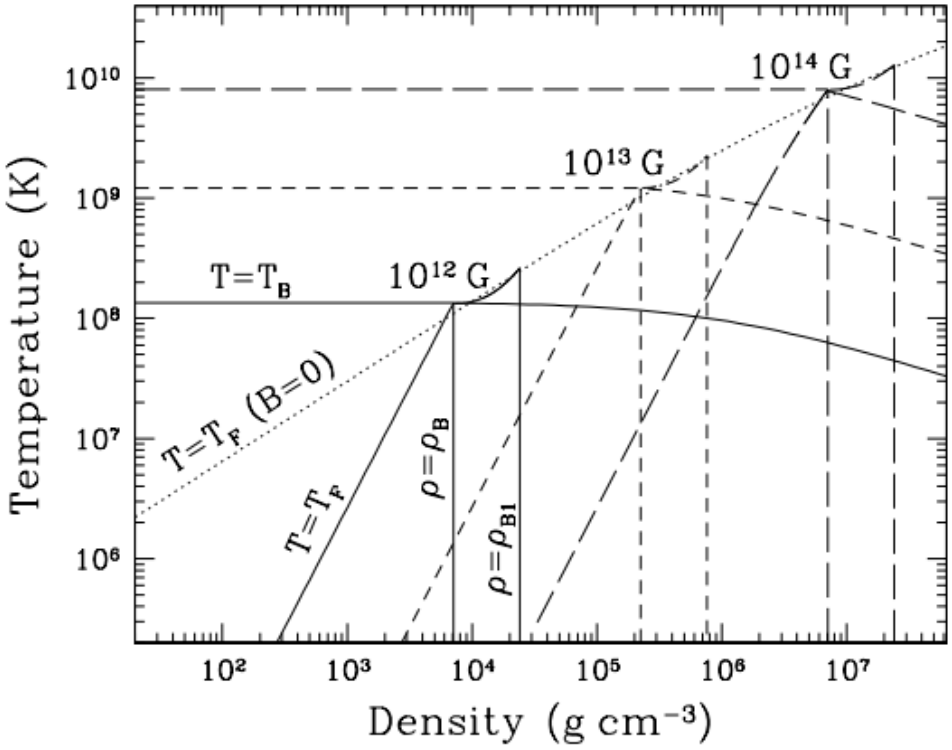

Figure 3.1: This diagram, taken from [10], illustrates the different temperature and density regimes of the magnetic field effects on the thermodynamic properties of a free-electron gas. Solid lines are for $B = 10^{12}$ G, short-dashed lines for $B = 10^{13}$ G and long-dashed lines for $B = 10^{14}$ G. The vertical lines are defined at $\rho = \rho_B$, defined in the text, and $\rho = \rho_{B1}$, below which only the $n_L = 0, 1$ levels are occupied. The Fermi temperature is outlined both below ρ_B and for $\rho_B < \rho < \rho_{B1}$. The magnetic temperature T_B, defined in Equation 3.12, is also shown. The Fermi temperature at B=0 is represented by a dotted line.

with the first term being the kinetic energy and the second one the Coulomb part; $r_i = (3/4\pi n_i)^{1/3}$ is the Wigner-Seitz radius and $n_i = \rho/m_i = \rho/Am_P$ is the ion number density. From the condition of zero pressure it follows:

$$\frac{dE_S}{dr_i} = 0\,, \tag{3.14}$$

from which we get the expressions for radius and energy at zero pressure:

$$\begin{aligned} r_{i,0} &\sim 1.90\, Z^{1/5} b^{-2/5} \\ E_{S,0} &\sim -0.395\, Z^{9/5} b^{2/5}\,. \end{aligned} \tag{3.15}$$

The *cohesive energy* Q_S, needed to pull an atom out of the bulk condensed matter at zero pressure, is defined as the difference between the atomic ground-state energy and the energy per cell of the condensed-matter ground state, $Q_S = E_1 - E_S$. Another possible definition is: $Q_S = Q_\infty + \Delta E_S$, where $Q_\infty \sim 0.76 b^{0.37} - 0.16(\ln b)^2$ is the cohesive energy for the linear chain, and $\Delta E_S = |E_{S,0}| - |E_\infty|$ is the energy difference between the one-dimensional chain and the 3D condensed matter. This difference can be estimated by calculating the quadrupole-quadrupole bond between the linear chains: the chain-chain interaction, then, plays a crucial role in determining whether the condensed matter is bound ($\Delta E_S > 0$) or not.

For $Z \gtrsim 6$, the chains are unbound: in this case, the lattice structure and the cohesive properties are different from the ones of H and He described above. For $Z \gtrsim 10$ the upper limit for the cohesive energy is $Q_S \lesssim Z^{9/5} B_{12}^{2/5}$ eV, so it increases for larger values of B. In the case of iron ($Z = 26$), if B is sufficiently large ($b \gg 2Z^3$) the chains are bound similarly to the case of H and He, through covalent bonding

along the field direction, and there is a weak cohesion between chains, allowing a phase transition for low enough temperatures.

From the thermodynamic point of view, magnetic condensation is a plasma phase transition due to strong electrostatic attraction between the charged particles (ions and electrons) in the dense plasma. The *critical temperature* $T_{\rm crit}$ for this transition to happen increases for stronger magnetic field strengths, so the condensation becomes more likely.
An important parameter in the description of a plasma is the *Coulomb cooling parameter*, i.e. the ratio between the electrostatic and the thermal energies, which in the case of ions is:

$$\Gamma = \frac{(Ze)^2}{r_i k_B T} = 22.75 \, \frac{Z^2}{T_6} \Big(\frac{\rho_6}{A} \Big)^{1/3} . \tag{3.16}$$

When $\Gamma \ll 1$ the plasma is a classical Boltzmann gas and is unaffected by B; instead, for $\Gamma \gtrsim 1$ it becomes a strongly-coupled Coulomb liquid. The melting of the Coulomb crystal takes place at $\Gamma = \Gamma_m \sim 175$: when the electron gas is non-uniform, this value becomes dependent on both the density ρ and the nuclear charge Z.

The condensed surface density at zero pressure is defined as:

$$\rho_s \sim 561 \eta A Z^{-3/5} B_{12}^{6/5} \text{ g cm}^{-3} , \tag{3.17}$$

where η is an unknown quantity of order of unity which absorbs the theoretical uncertainties; in the case of an ion sphere model $\eta = 1$.
The density associated to a gas made of free electrons, protons, bound atoms and molecules, is:

$$\rho_g \sim 390 A^{5/2} T^{5/2} \exp \Big(- \frac{Q_S}{T} \Big) \text{ g cm}^{-3} . \tag{3.18}$$

The critical temperature for the phase transition is found through the condition $\rho_s = \rho_g$, which for iron gives the upper limit:

$$k_B T_{\rm crit}^{\rm Fe} \lesssim 0.1 \, Q_S \sim 27 \, B_{12}^{2/5} \text{ eV} . \tag{3.19}$$

As mentioned above, the phase separation is given by $T < T_{\rm crit}$: this limit is however quite uncertain and the preferred condition is then $T < T_{\rm crit}/2$, for which $\rho_g \ll \rho_s$, meaning that the phase transition is unavoidable.
A list of values for $T_{\rm crit}$ with the corresponding field strengths, in the case of Fe-composition, is presented in [21]:

$$\begin{array}{rlcl} T_{\rm crit} \sim & 6 \times 10^5 \text{ K} & \text{for} & B_{12} = \quad 5 \\ & 7 \times 10^5 \text{ K} & & 10 \\ & 2 \times 10^6 \text{ K} & & 100 \\ & 10^7 \text{ K} & & 500 \\ & 2 \times 10^7 \text{ K} & & 1000 \, . \end{array}$$

Figure 3.2 shows the conditions of B and T for the presence of condensation, comparing the cases of hydrogen and iron.

Effects on the emission

In the presence of condensation, the thermal emission comes directly from the metallic surface, without being reprocessed in the gaseous atmosphere: for $T \ll T_{\rm crit}$, the atmosphere density and its optical depth are negligible, and the neutron star is said to be *naked* or *bare*. The resulting spectrum is therefore determined by the emission and reflection properties of the condensed surface. The local flux density is given by the Planck function multiplied by the normalized emissivity. Generally speaking, the overall emission from a condensed liquid surface is reduced from the blackbody one by less than a factor 2 [10]. The emission is even more BB-like for solid surfaces, which are rougher and with a reflectivity close to zero, as is likely the case of Fe.
The spectra may also present mild absorption features, corresponding to the ion cyclotron frequency and

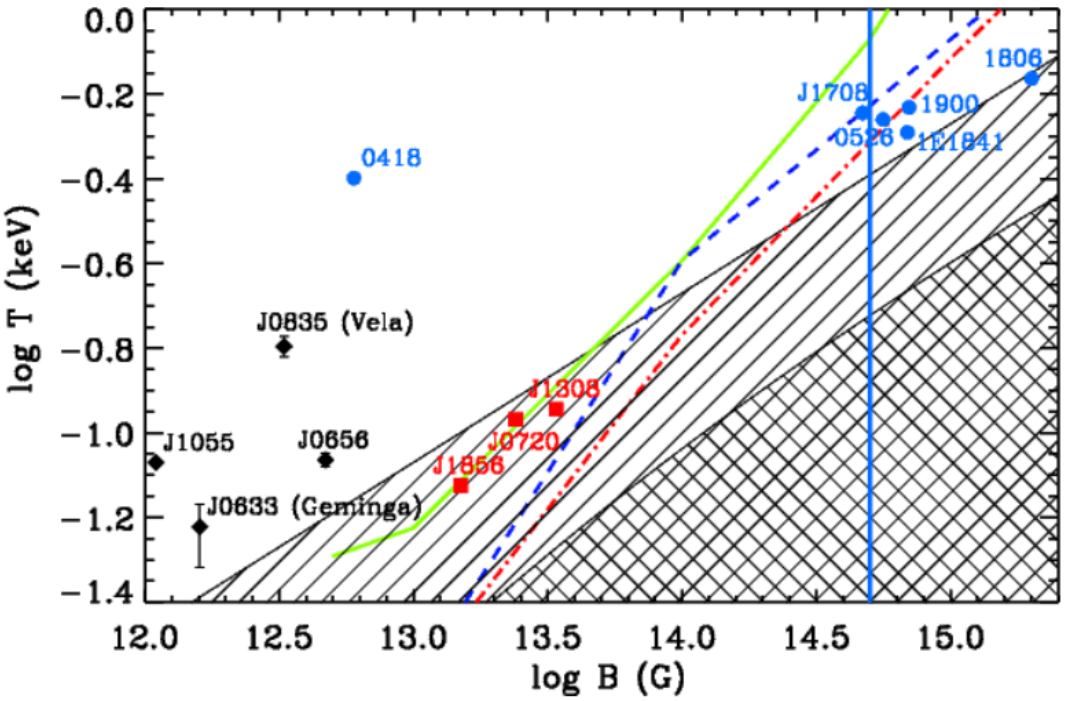

Figure 3.2: This diagram, from [22], shows the critical temperature as a function of the magnetic field strength: condensation is possible in the hatched region for Fe and in the cross-hatched one for H, according to the estimate made by [18]. Different chemical compositions are also represented: He (dash-dotted red line), C (dashed blue) and Fe (solid green), according to the calculations made by [23] and [21]. The spin-down dipolar field and the effective temperature of different sources are also marked: magnetars (cyan filled circles), XDINSs (red squares) and isolated pulsars (black diamonds). The thick vertical line in cyan corresponds to $B = 5 \times 10^{14}$ G.

the electron plasma frequency.
Figure 3.3 shows examples of spectra from a partially/fully ionized atmosphere and from a condensed surface, both compared to the blackbody function.

The emission can be studied considering two limiting cases, described in [24], [19] and [22]: in the free-ions limit the Coulomb interactions between ions are neglected, while in the fixed-ions one the ion motion is frozen and there is no influence from the magnetic forces. The latter can be obtained by setting the ion mass to infinity. The two regimes show different emission trends for energies below the ion cyclotron energy, but are quite similar otherwise. The real emission properties are assumed to lie between these two limits, although this problem has not been fully solved yet.
An example of emission in these limits is shown in Figure 3.4.

Magnetic condensation also affects the polarization of the emitted radiation: it can be seen in Figure 3.5 that the polarization degree is highly reduced in the case of emission from a condensed surface, both in the case of free- and fixed-ions limits, with respect to the atmosphere model.

Presence of an atmospheric layer

The condensed surface of neutron stars is probably a Fe solid surface, where the iron is assumed to be formed at the birth of the NS. There is the possibility of the presence of a H-atmosphere of finite thickness above this solid surface, which would be almost transparent at high energies. Its origin could be of different natures:

- accretion from the interstellar medium: this accretion is less effective for strong magnetic fields and/or high spins;

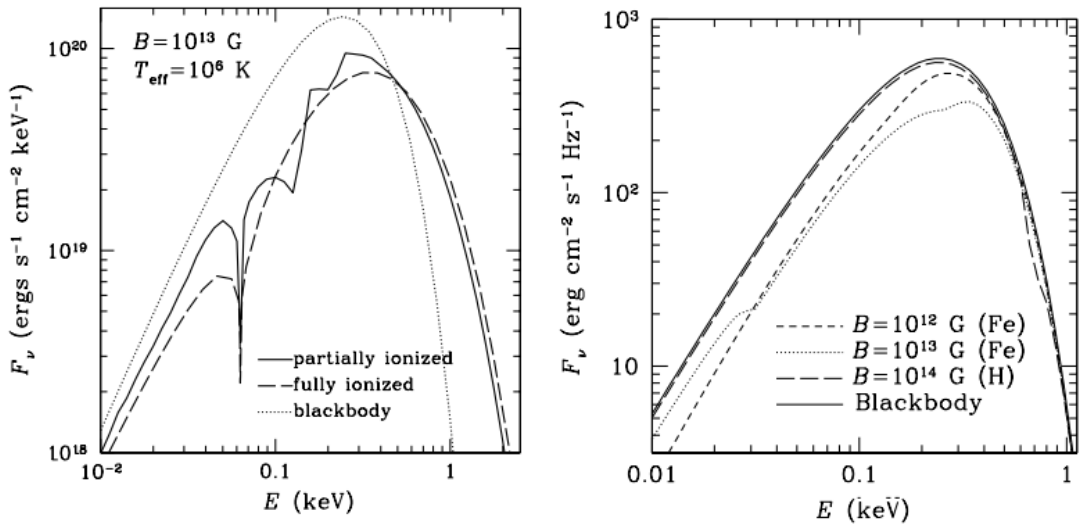

Figure 3.3: The spectral flux is shown as a function of the photon energy, from [10]. *Left:* the cases of a partially ionized H-atmosphere and a fully ionized one compared to the blackbody spectrum. *Right:* spectral flux of a condensed Fe surface in the free-ions limits (see the text), with $B = 10^{12}$ G and $B = 10^{13}$ G, and a condensed H surface with $B = 10^{14}$ G, compared with the BB spectrum, all at $T = 10^6$ K.

- diffusive nuclear burning of a hydrogen layer soon after the formation of the neutron star;
- nuclear spallation in collisions with ultra-relativistic particles.

At the beginning, there might be a mixture of H and He, which would then be separated due to the strong gravity at the NS surface, resulting in the so-called *sandwich atmosphere*.

Vacuum gap

The presence of a condensed surface is usually followed by the formation of a *vacuum gap* [21]: charged particles flow from the polar cap region and travel beyond the light cylinder, after which they have to be replenished to maintain the magnetosphere charge density. If $T_{\rm surface}$ and Q_S are such that the particles are tightly bound to the surface, which is commonly the case for high enough B or low enough T, then this does not happen, leaving a gap. The particles can then be accelerated across the gap, affecting the emission properties of the surface.
Figure 3.6 shows the values of T and B needed to form a vacuum gap.

3.2 Polarization

The emission from neutron stars with very strong magnetic fields is expected to be highly polarized. The study of this polarization can give a new and unique insight on the physical conditions of the star surface and magnetosphere, as well as on the geometry of the star, complementing the spectral and timing measurements.

Polarization modes

As anticipated in Section 2.1, photons propagating in strong magnetic fields can be linearly polarized in two normal modes: the ordinary (O) mode with the electric field vector parallel to the plane formed by the photon propagation direction ($\vec{k}$) and the field direction, and the extraordinary (X) mode with the electric field oscillating in the direction perpendicular to the k-B plane. When $\omega < \omega_c$, with ω the photon frequency and ω_c the electron cyclotron frequency, the radiative processes taking place in strong magnetic

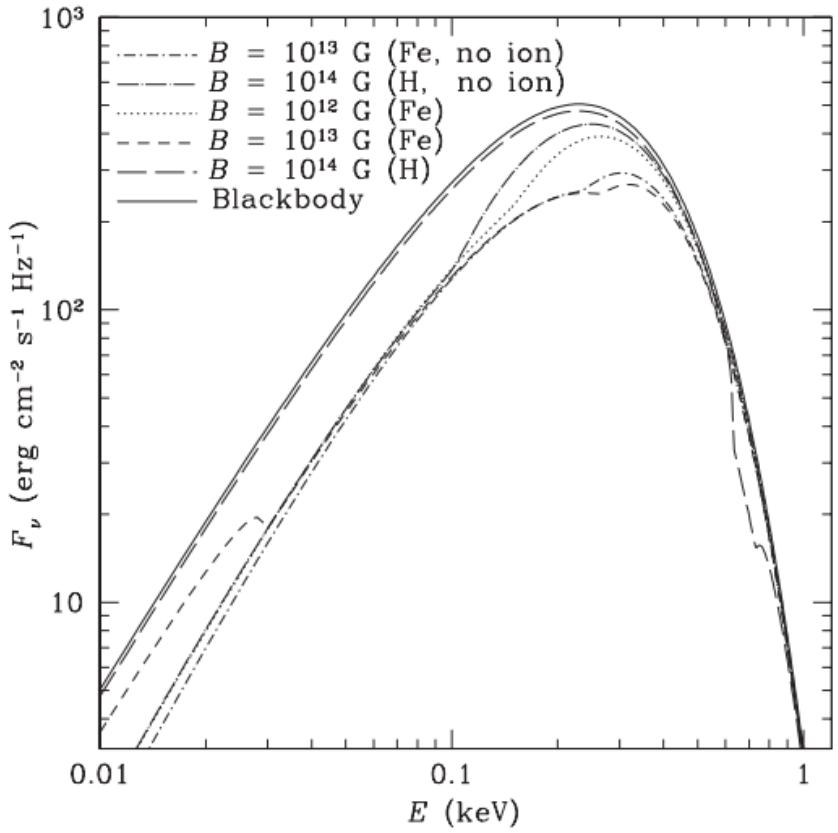

Figure 3.4: From [24], same as Figure 3.3, but showing also the limit of fixed-ions, labelled as 'no ion'. The cases considered are the ones of condensed surfaces made of Fe at $B = 10^{12}$–10^{13} G and H at $B = 10^{14}$ G. The temperature is $T = 10^6$ K. As in Figure 3.3, the blackbody spectrum is also shown for comparison.

fields have an opacity for the X-mode which is typically $\kappa_X \sim \kappa_O(\omega/\omega_c)^2$, where κ_O is the opacity of photons in the O-mode: therefore, far from the cyclotron resonance, the opacity of extraordinary photons is much smaller than the one of the ordinary ones, and the seed thermal radiation is likely to be mostly polarized in the X-mode, when scattering processes are considered. Also, κ_X decreases for stronger magnetic field strengths, while κ_O does not.

Many effects play a role in determining the final polarization state of the emitted radiation from magnetars. One of these is RCS, described in Section 2.1: upon scattering, the photons initially in the O-mode can turn into the X-mode, while the extraordinary photons are more likely to retain their original polarization mode, with the scattering cross sections being [25]:

$$\begin{aligned} \sigma_{O-O} &= \frac{1}{3}\,\sigma_{O-X} \\ \sigma_{X-X} &= 3\,\sigma_{X-O}\,, \end{aligned} \tag{3.20}$$

where the first subscript index refers to the incident photon and the second index to the scattered one.

Vacuum polarization

A magnetized plasma around a neutron star is anisotropic and birefringent, influencing the polarization state of radiation. Specifically, QED predicts the effect of *vacuum polarization*, which influences the photon propagation at high frequencies: the photon temporarily converts into virtual electron-positron pairs, which are then "polarized" by the external magnetic field. As a consequence, the magnetized vacuum

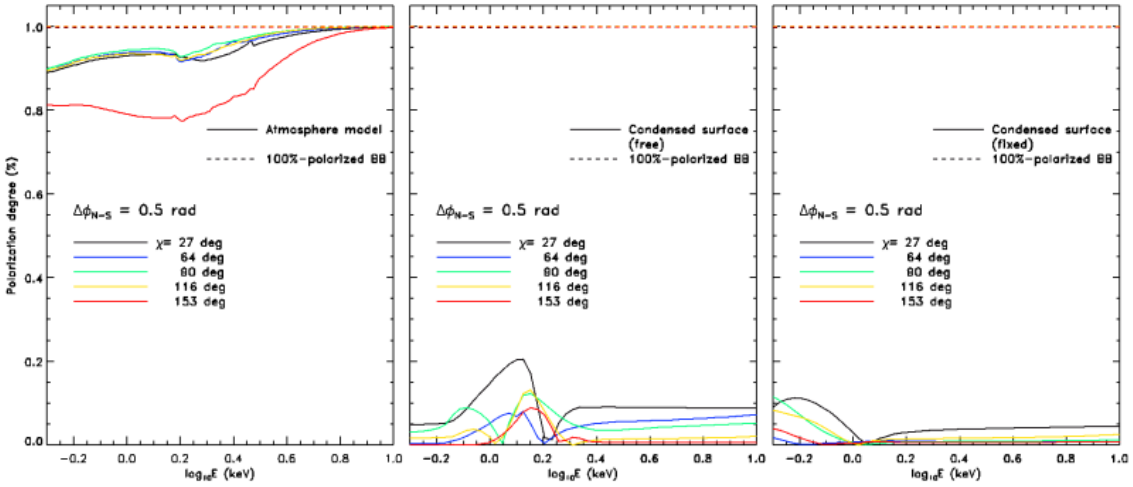

Figure 3.5: From [22], the linear polarization degree at the surface as a function of the photon energy, in the case of an atmosphere (left panel), a condensed surface in the free-ions limit (middle) and in the fixed-ions limit (right). The external magnetic field is a globally-twisted dipole, with $B_{\rm P} = 5 \times 10^{14}$ G and $\Delta\phi_{_{N-S}} = 0.5$ rad, aligned with the star's rotation axis. The star is seen at different inclinations χ, for which the polarization degrees are shown in different colours. The dashed lines show the intrinsic polarization for BB and completely polarized seed photons.

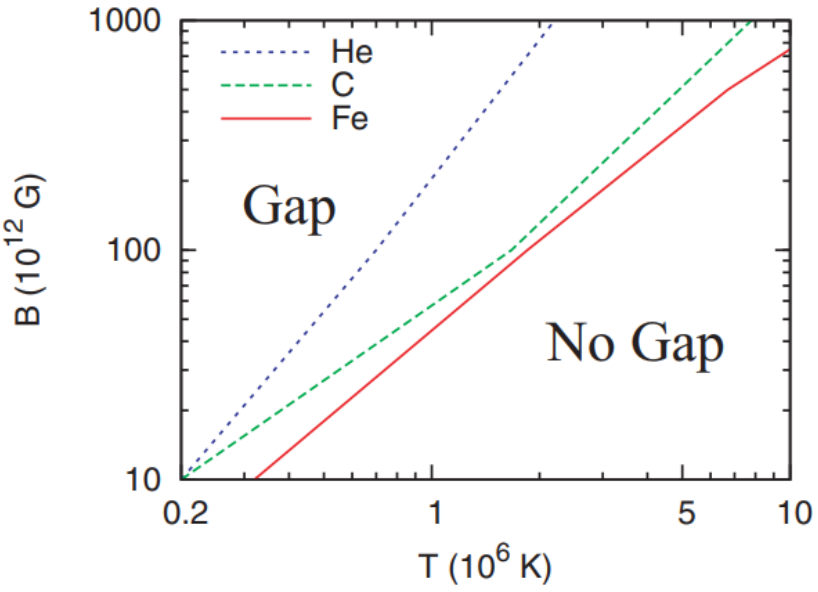

Figure 3.6: This diagram from [21] shows the condition for the formation of a vacuum gap above a condensed NS surface made of He, C and Fe. The gap is formed for a certain surface composition in the region above the corresponding line. In this case, $\Omega \cdot B_P < 0$, with Ω the rotation rate of the NS, and the magnetosphere is said to be *positive* over the poles.

is described by non-trivial dielectric and magnetic permeability tensors. If the vacuum polarization is weak, i.e. $B \lesssim B_{\rm QED}$, then its effect is linearly added to the plasma polarization.

Vacuum polarization effects dominate over plasma ones for densities below the *vacuum resonance density* ρ_V, which is usually the case for magnetar magnetospheres. Away from the vacuum resonance, the vacuum and the plasma act in linearizing the polarization: the vacuum tends to maintain the original

state, while the effect of plasma is to change the polarization mode. As a consequence, at $\rho \sim \rho_V$ the normal modes tend to have a circular polarization. When the photons traverse this resonance, they undergo a mode conversion, as shown in Figure 3.7: the O modes become X modes and viceversa, and there is a 90° rotation of the polarization ellipse. The mode conversion has an effect on the radiative transfer, because of the different opacities associated with the polarization states as described above, becoming therefore a signature of vacuum polarization.

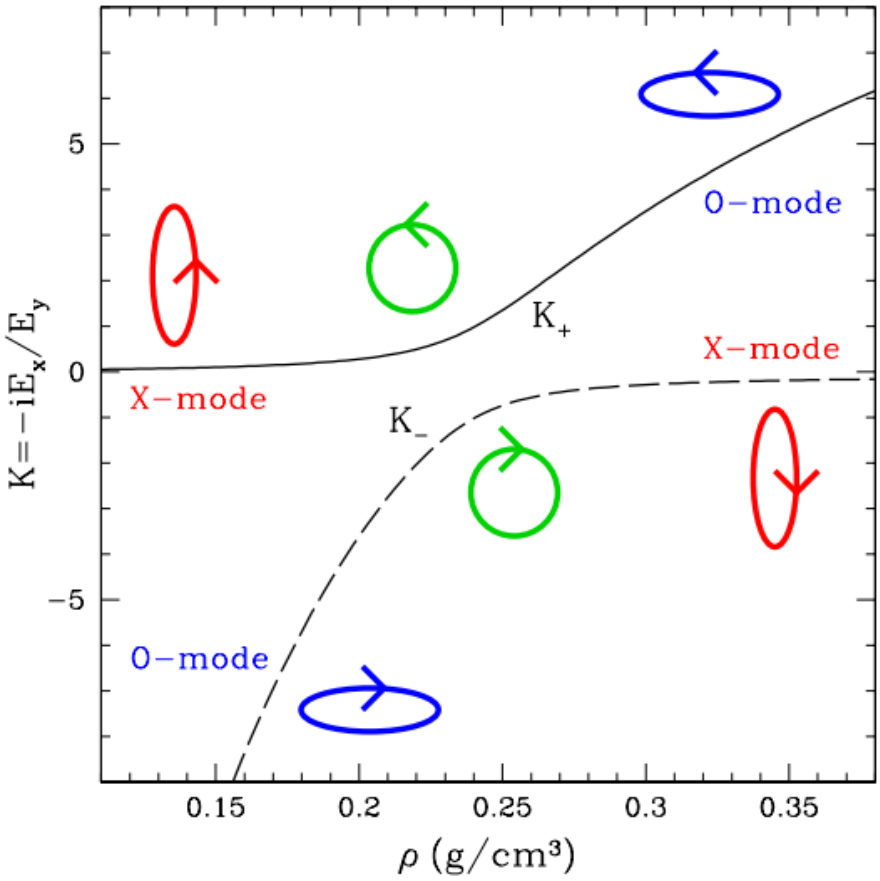

Figure 3.7: This diagram, from [10], shows the ellipticity of the photon mode as a function of the plasma density close to the vacuum resonance, for $B = 10^{13}$ G forming an angle of 45° with the photon propagation direction, $E_{ph} = 5$ keV and $A = Z$. The ellipticity is given by $K = -iE_x/E_y$, with E_x and E_y the electric field components of the photon respectively along and perpendicular to the k-B plane.The O-mode is characterized by $|K| \gg 1$ and the X-mode $|K| \ll 1$. We can see that, away from the resonance, the modes are almost linearly polarized and their polarization ellipses are orthogonal to each other; instead, at $\rho = \rho_V$ both modes become circularly polarized. At higher densities, the modes of the photons change and the polarization ellipses are rotated by 90° with respect to the original ones.

As described in [26], the electric field associated to a photon with energy $\hbar\omega$ can be written as $\vec{E} = \vec{A}(z)\exp[i(k_0 z - \omega t)]$, with $k_0 = \omega/c$. $\vec{A}$ is the complex amplitude of the electric field, i.e., in the reference frame defined above,

$$\vec{A} = (A_x, A_y) = (a_x e^{-i\varphi_x}, a_y e^{-i\varphi_y})\,. \tag{3.21}$$

Substituting Equation 3.21 inside the wave equation we get differential equations for the amplitude, which

describe the evolution of the polarization modes in the magnetized vacuum:

$$\frac{dA_x}{dz} = \frac{ik_0\delta}{2}(MA_x + PA_y)$$
$$\frac{dA_y}{dz} = \frac{ik_0\delta}{2}(PA_x + NA_y)\,, \tag{3.22}$$

with $\delta \sim 3 \times 10^{-10} B_{11}^2$ and M, P and N coefficients which depend on the magnetic field (see Appendix A of [17]).

An important effect of vacuum polarization is the continuous adaptation of the electric field direction to the magnetic field one, in strong magnetic fields. From Equations 3.22 one derives that the scale-length along which the electric field's amplitude varies is:

$$l_A \sim \frac{2}{k_0\delta} \propto B^{-2}\,; \tag{3.23}$$

instead, the magnetic field varies along a distance:

$$l_B \sim \frac{B}{|\vec{k}\cdot\nabla B|}\,, \tag{3.24}$$

which has a slower growth with B with respect to l_A. Near the surface of the star, where the magnetic field is very strong, $l_A \ll l_B$. This means that the direction along which the electric field oscillates adapts instantaneously to the direction of the magnetic field, so the photons maintain their initial polarization states. Because the adaptation of the electric field direction is practically instantaneous, the propagation of the photons is said to be *adiabatic*. As B decreases and l_A increases faster than l_B, $\vec{E}$ follows the direction of the magnetic field less and less instantaneously, until $l_A \sim l_B$. This condition is met at the so-called *adiabatic radius*, which for a dipolar field is given by:

$$r_{ad} \sim 4.8\Big(\frac{B_P}{10^{11}\,\mathrm{G}}\Big)^{2/5}\Big(\frac{E}{1\,\mathrm{keV}}\Big)^{1/5}\Big(\frac{R_{\mathrm{NS}}}{10\,\mathrm{km}}\Big)^{1/5} R_{\mathrm{NS}}\,. \tag{3.25}$$

Outside, where $l_A \gg l_B$, the electric field freezes and the polarization modes start to deviate significantly with respect to the original ones, as the magnetic field direction changes. Figure 3.8 shows how the adiabatic radius changes as a function of the magnetic field and the photon energy.
Equations 3.22 should be integrated from the surface up to where the amplitude components A_x and A_y are nearly constant, but a simplified approach, which allows to reduce the computational time, considers a sharp edge between the adiabatic region and the external region: in this way, from a polarization point of view, it is as if the photons were emitted at the adiabatic radius, so the topology of the magnetic field that matters is the one at r_{ad}.

Polarization observables

The polarization observables are the *polarization degree* Π_{pol} and the *polarization angle* χ_{pol}. In general, they depend on the geometrical angles χ, between the photon propagation and the spin axis, and ξ, between the spin axis and the magnetic field direction, as well as on the physical process which determines the emission of photons at the surface. In the specific case of magnetars, with a twisted magnetosphere, these observables can be also dependent on the twist angle, defined in Equation 2.15, and on the motion of the charges in the magnetosphere. Up to now, the study of the X-ray radiation emitted from neutron stars has been carried on through spectral analyses. However, these are often degenerate for what concerns the emission mechanism, since, as discussed in Chapter 3.1, both the atmosphere and the condensed surface produce BB-like spectral components. This degeneracy can be removed thanks to polarimetric studies.

The polarization observables are more conveniently expressed through the Stokes parameters [26], which are additive. In the reference frame (x,y,z), defined above, they are defined as:

$$\mathcal{I} = a_x^2 + a_y^2$$
$$\mathcal{Q} = a_x^2 - a_y^2$$
$$\mathcal{U} = 2a_x a_y \cos(\varphi_x - \varphi_y)$$
$$\mathcal{V} = 2a_x a_y \sin(\varphi_x - \varphi_y) \tag{3.26}$$

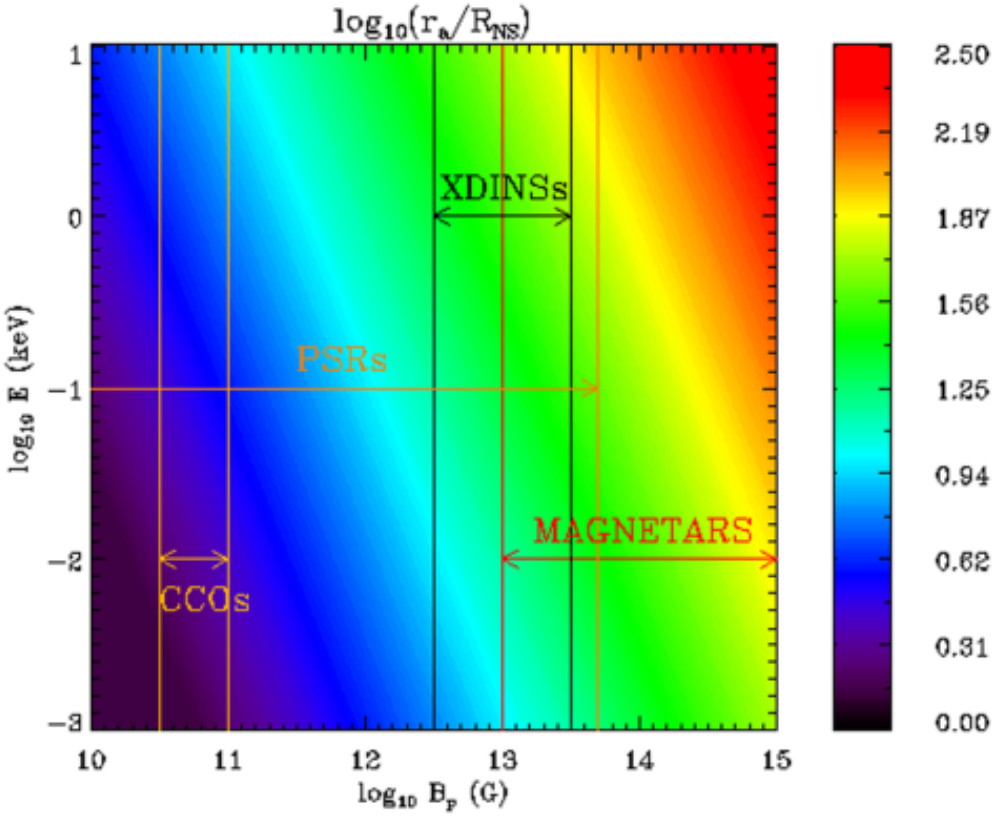

Figure 3.8: This contour plot from [26] shows the dependence of r_{ad} on the polar magnetic field strength and on the photon energy. The figure also shows the typical ranges of B_P for some classes of neutron stars: CCOs, PSRs, XDINSs and magnetars.

where $\mathcal{I}$ is the total intensity, $\mathcal{Q}$ and $\mathcal{U}$ define the linear polarization and $\mathcal{V}$ the circular one ($\mathcal{V} = 0$ when completely linearly polarized emission is considered, as is our case). The Stokes parameters satisfy the condition $\mathcal{I}^2 \geq \mathcal{Q}^2 + \mathcal{U}^2 + \mathcal{V}^2$, with the equal sign corresponding to 100% polarization or to monochromatic radiation.
Normalizing to the total intensity, we can describe the photons polarized in the two modes through specific Stokes vectors:

$$\begin{pmatrix} \bar{\mathcal{Q}} \\ \bar{\mathcal{U}} \\ \bar{\mathcal{V}} \end{pmatrix}_X = \begin{pmatrix} -1 \\ 0 \\ 0 \end{pmatrix}, \begin{pmatrix} \bar{\mathcal{Q}} \\ \bar{\mathcal{U}} \\ \bar{\mathcal{V}} \end{pmatrix}_O = \begin{pmatrix} 1 \\ 0 \\ 0 \end{pmatrix}. \tag{3.27}$$

The definition of the Stokes parameters in 3.26 depends on the frame of reference (x,y,z), where the direction of the x- and y-axis on the polarization plane depends on the direction of B at emission. The photons that are gathered by the detector are each emitted from different parts of the surface: since the magnetic field changes in general from point to point, the orientation of the axes also varies, resulting in the Stokes parameters relative to the single photons being defined in different reference frames. In order to sum the Stokes parameters associated with the single photons, they need to be defined in the same reference frame: they are therefore rotated, considering a fixed frame of reference, which usually coincides with the focal plane of the detector. This geometrical effect causes a depolarization and it is important when the magnetic field is not uniform across the emission region. The angles of rotation of each frame are α_i with respect to the line of sight (LOS): they depend on the field geometry, on the adiabatic radius and on the energy and position of the emitted photons [26].

The rotation to be applied on the parameters results in:

$$\begin{aligned} I_i &= \bar{\mathcal{I}}_i \\ Q_i &= \bar{\mathcal{Q}}_i \cos(2\alpha_i) + \bar{\mathcal{U}}_i \sin(2\alpha_i) \\ U_i &= \bar{\mathcal{U}}_i \cos(2\alpha_i) - \bar{\mathcal{Q}}_i \sin(2\alpha_i) \,. \end{aligned} \tag{3.28}$$

The Stokes parameters of the radiation collected at infinity, considering that the emitted photons are polarized either in the O- or in the X-mode, are therefore:

$$\begin{aligned} Q &= \sum_{i=1}^{N_X} \cos(2\alpha_i) - \sum_{j=1}^{N_O} \cos(2\alpha_j) \\ U &= \sum_{j=1}^{N_O} \sin(2\alpha_j) - \sum_{i=1}^{N_X} \sin(2\alpha_i) \,, \end{aligned} \tag{3.29}$$

with N_X and N_O the number of photons polarized in the X- or O-mode respectively.

We can now define the polarization observables. In the case of linear polarization:

$$\begin{aligned} \Pi_L &= \frac{\sqrt{Q^2 + U^2}}{I} \\ \chi_{pol} &= \frac{1}{2} \arctan\left(\frac{U}{Q}\right) . \end{aligned} \tag{3.30}$$

If the magnetic field is uniform, for example when the emitting region is very small, the angles of rotation for the Stokes parameter frames are all equal to the same value α_0. The polarization observables can then be expressed as:

$$\begin{aligned} \Pi_L &= \frac{|N_X - N_O|}{N} \\ \chi_{pol} &= \alpha_0 \,. \end{aligned} \tag{3.31}$$

For what concerns the angle of polarization, we can see from Equation 3.31 that it is linked to the distribution of the angles of rotation of the reference frames. Therefore, a measurement of the angle α_0 can, in principle, be used to obtain information on the topology of the magnetic field.

Vacuum polarization is also important for aligning the polarization vectors of photons emitted from different patches of the neutron star. In general, when considering an extended emitting region near the surface, where the direction of the magnetic field changes from point to point, the angles α_i are different and the resulting polarization fraction is reduced with respect to the intrinsic one, i.e. $(N_X - N_O)/N$. In the case of magnetars, when vacuum polarization is effective, the photons retain their initial polarization state until a great distance from the surface of the star (see Figure 3.8): at the adiabatic radius, then, the magnetic field is quite uniform, and the angles α_i are similar to each other, with a much smaller reduction factor with respect to Equation 3.31. This effect therefore grants an appreciable net polarization fraction at the observer, if the radiation was polarized when emitted. Hence, if radiation comes reasonably from a large area on the surface, the detection of a high degree of X-ray polarization can be symptomatic of a large adiabatic radius, and can be interpreted as a indirect probe of the presence of a strong field. The effect is dependent on the extent of the radiating region, so that the presence or absence of QED-related properties can only be tested for emitting areas of significant extension.

Chapter 4

Numerical tools

This chapter presents the numerical tools used to compute the emission properties of a condensed surface. It is divided into two parts. The first deals with the computation of the emissivity of the naked surface, following [27]. The second illustrates the ray-tracing technique which allows us to compute the observed properties of the source. The latter is based on the calculations originally presented in [28] and then in [26].

4.1 Spectral properties of condensed magnetized surfaces

Potekhin et al. [27] studied the emission from neutron stars with a condensed surface, in both the limiting cases of free and fixed ions. The same study was first carried out by [29], [24] and [30]. [27] reprised the numerical method of [24] and improved it.
The task of modelling and interpreting the spectra, complicated by the wide variety of theoretical possibilities, was facilitated by using the approximate treatment introduced in 2010 by [31], where the local spectra are fitted by simple analytic functions. This approach was also improved by [27], by using more accurate fitting formulae and by considering the dependence of the reflectivity also on the magnetic field and on the angle ϕ, i.e. the angle between the plane of incidence of radiation and the plane containing the normal to the surface and the magnetic field lines.

The final method used by [27] considers a condensed Fe-surface, so $Z = 26$ and $A = 56$, with $\eta = 1$ (see Equation 3.17), which enter in the expression for the density:

$$\rho = 8.9 \times 10^3 \, \eta \, A \, Z^{-0.6} \, B_{13}^{1.2} \text{ g cm}^{-3} \, . \tag{4.1}$$

The temperature is $T \sim 10^6$ K.
The surface element considered for the calculations is small, with the variation of the magnetic field strength and of its inclination across the element being neglected. This element is treated as a plane, with z perpendicular to it and the magnetic field lying on the x-z plane; the y-axis is then taken as perpendicular with respect to x and z. The angle θ_B is between the field direction and the z-axis, while θ_k is the angle between z and the direction of the reflected beam. The angle between the field direction and the propagation direction is denoted as α_i for the incident beam and α_r for the reflected one, while ϕ is the angle in the x-y plane made by the projection of the reflected wave vector. A scheme illustrating the frame of reference (x,y,z) and the different angles is shown in Figure 4.1. The direction of B is shown, as well as those of incidence (wave vector $\vec{k}_i$) and of reflection ($\vec{k}_r$).
The angles characterizing the direction of the photons are defined by:

$$\cos \alpha_\text{i,r} = \sin \theta_B \sin \theta_k \cos \phi \mp \cos \theta_B \cos \theta_k \, , \tag{4.2}$$

with the minus and plus sign referring to the incident and reflected waves, respectively.

The monochromatic intensity of the emitted radiation is:

$$I_{E,j} = J_j \frac{B_E}{2} \, , \tag{4.3}$$

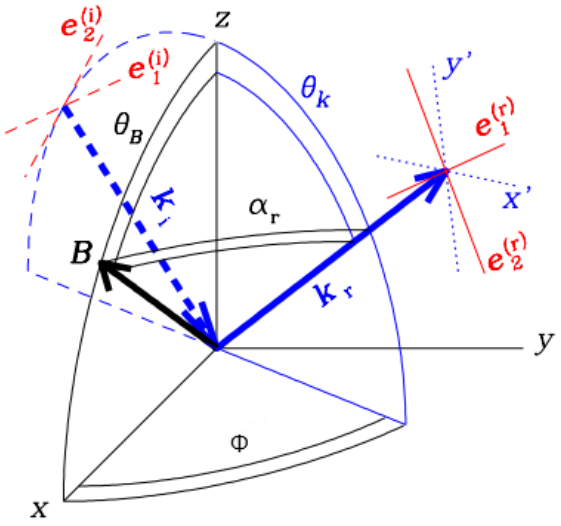

Figure 4.1: The frame of reference described in the text from [27]. The figure also shows the polarization vectors, both for incidence, $\mathbf{e}_{1,2}^{(i)}$, and reflection, $\mathbf{e}_{1,2}^{(r)}$, perpendicular to the respective wave vector ($\vec{k}_i$ and $\vec{k}_r$). $\mathbf{e}_1^{(i,r)}$ are parallel to the surface, while $\mathbf{e}_2^{(i,r)}$ lie in the perpendicular plane; the axes denoted as x' and y' lie in the plane made by $\mathbf{e}_1^{(r)}$ and $\mathbf{e}_2^{(r)}$, with x' aligned to the plane $\vec{B}$-$\vec{k}_r$.

where the index j refers to a linear polarization parallel to the incident plane ($j = 1$) or perpendicular to it ($j = 2$). The function B_E is:

$$B_E = \frac{B_\nu}{2\pi\hbar} = \frac{E^3}{4\pi^3\hbar^3c^2(e^{E/k_BT} - 1)}\,, \tag{4.4}$$

with B_ν the Planck function. J_j is the dimensionless emissivity:

$$J_j = 1 - R_j\,, \tag{4.5}$$

with R_j the effective reflectivity, which depends on the chemical composition, the photon energy E, the magnetic field strength, the angle θ_B and the direction of photon propagation. In the case of non-polarized radiation, the reflectivity can be approximated by its mean value:

$$R = \frac{R_1 + R_2}{2}\,. \tag{4.6}$$

Emissivity calculation

A numerical code was developed to reproduce the emissivity behaviour for a condensed surface in the free- and fixed-ions limits, according to the fitting formulae by [27].
In the first part of the code, the emissivity is calculated for different photon energy ranges in the free-ions limit: $E < E_{\rm ci}$, $E_{\rm ci} \lesssim E \lesssim E_{\rm c}$ and $E > E_{\rm c}$, where:

$$\begin{aligned} E_{\rm ci} &= \frac{\hbar ZeB}{Am_uc} = 0.0635\,\frac{Z}{A}B_{13}\,\text{keV} \\ E_{\rm pe} &= 0.0288\sqrt{\frac{\rho Z}{A}}\,\text{keV} \\ E_{\rm ce} &= 115.77\,B_{13}\,\text{keV} \\ E_{\rm c} &= E_{\rm ci} + \frac{E_{\rm pe}^2}{E_{\rm ce}}\,. \end{aligned} \tag{4.7}$$

Here $E_{\rm ci}$ is the ion cyclotron energy, with m_u the atomic mass unit, $E_{\rm pe}$ is the electron plasma energy and $E_{\rm ce}$ the electron cyclotron energy.

Before the emissivities are calculated, we give some definitions. The angles $\alpha_{\rm i,r}$ are derived from Equation 4.2 and α is defined as the minimum between these two values. Then, two *effective energies* are introduced:

$$\begin{aligned}\tilde{E}_{\rm pe} &= E_{\rm pe}\sqrt{3-2\cos\theta_k}\\ \tilde{E}_{\rm c} &= E_{\rm ci}+\frac{(\tilde{E}_{\rm pe})^2}{E_{\rm ce}}\,.\end{aligned} \tag{4.8}$$

Different definitions are given for the emissivity J, depending on the energy range considered.
At low energies ($E < E_{\rm ci}$), the expression for the emissivity is:

$$J_{\rm A} = [1-A(E)]J_0(E)\,, \tag{4.9}$$

with:

$$\begin{aligned}A(E) &= \frac{1-\cos\theta_B}{2\sqrt{1+B_{13}}}+\left[0.7-\frac{0.45}{J_0(0)}\right](\sin\theta_k)^4(1-\cos\alpha)\\ J_0(0) &= 4\left(\sqrt{E_{\rm c}/E_{\rm ci}}+1\right)^{-1}\left(E_{\rm ci}/E_{\rm c}+1\right)^{-1}\\ J_0(E) &= 1-\frac{1}{2}\left(R_-^{(0)}+R_+^{(0)}\right)\\ R_\pm^{(0)} &= \left|\frac{n_\pm^{(0)}-1}{n_\pm^{(0)}+1}\right|^2\\ n_\pm^{(0)} &= \left[1\pm\frac{E_{\rm pe}^2}{E_{\rm ce}(E\pm E_{\rm ci})}\right]^{1/2}\,.\end{aligned} \tag{4.10}$$

At $E_{\rm ci} \lesssim E \lesssim \tilde{E}_{\rm c}$, the emissivity is:

$$J_{\rm B} = \left(\frac{E}{\tilde{E}_{\rm c}}\right)^p J(\tilde{E}_{\rm c})\,, \tag{4.11}$$

where:

$$p = \frac{\ln[J(\tilde{E}_{\rm c})/J(E_{\rm ci})]}{\ln(\tilde{E}_{\rm c}/E_{\rm ci})} \tag{4.12}$$

and

$$\begin{aligned}J(\tilde{E}_{\rm c}) &= \frac{1}{2}+\frac{0.05}{1+B_{13}}(1+\cos\theta_B\sin\theta_K)-0.15\,(1-\cos\theta_B)\sin\alpha\\ J(E_{\rm ci}) &= \frac{2\,n_0}{(1+n_0)^2}\left(1+\frac{\cos\theta_B-\cos\theta_k}{2\,(1+B_{13})}\right)\\ n_0 &= \left(1+\frac{E_{\rm pe}^2}{2\,E_{\rm ce}E_{\rm ci}}\right)^{1/2}\,.\end{aligned} \tag{4.13}$$

Finally, for the higher energies ($E > \tilde{E}_{\rm c}$):

$$J_{\rm C} = \frac{4\tilde{n}}{(1+\tilde{n})^2} \tag{4.14}$$

with

$$\tilde{n}^2 = 1+\frac{\tilde{E}_{\rm pe}^2}{E_{\rm ce}(E-E_{\rm ci})}\,. \tag{4.15}$$

The emissivity experiences a suppression at $E \sim E_{\rm pe}$, whose exact position, width, and depth depend on the geometry of the problem. The consequence is the presence of a line, described by:

$$L = \left[\frac{0.17\, E_{\rm pe}/E_{\rm c}}{1+X^4} + 0.21\, {\rm e}^{-(E/E_{\rm pe})^2} \right] (\sin\theta_k)^2\, W_L\,, \tag{4.16}$$

with

$$\begin{aligned} X &= \frac{E-E_L}{2\,E_{\rm pe} W_L} (1-\cos\theta_k)^{-1} \\ E_L &= E_{\rm pe} \Big[1 + 1.2\,(1-\cos\theta_k)^{3/2} \Big] \Big[1 - \frac{1}{3} (\sin\theta_B)^2 \Big] \\ W_L &= 0.8 \Big(\frac{\tilde{E}_{\rm c}}{E_{\rm pe}} \Big)^{0.2} \sqrt{\sin(\alpha/2)} \big[1 + (\sin\theta_B)^2 \big]\,. \end{aligned} \tag{4.17}$$

When the radiation is parallel to the magnetic field, i.e. $\alpha \sim 0$, L goes to zero; however, a remnant of the line is observed and it becomes appreciable as the field inclination becomes large, $\theta_B > \pi/4$.

An approximation for the emissivities in each of the two polarization modes ($j = 1$ and $j = 2$, defined above) is also given:

$$\begin{aligned} J_1 &= \begin{cases} J_{\rm A1} & \text{for } E < E_{\rm ci} \text{ and } J_{\rm A} > J_{\rm B} \\ J_{\rm B1}(1-J_{\rm C}) + J_{\rm C}(R_L) & \text{for } E > E_{\rm ci} \text{ and } J_{\rm A} < J_{\rm B} \end{cases} \\ J_2 &= 2\,J - J_1\,, \end{aligned} \tag{4.18}$$

where

$$R_L = (\sin\theta_B)^{1/4} \Big[2 - (\sin\alpha)^4 \Big] \frac{L}{1+L} \tag{4.19}$$

describes the line alongside L. From the second of Equations 4.18 we find that the total emissivity J is equal to the sum of the emissivities in the two polarization modes, divided by two.

The emissivities that appear in Equations 4.18 are defined by:

$$\begin{aligned} J_{\rm A1} &= (1-A_1) J_{\rm A} \\ J_{\rm B1} &= \left(\frac{E}{\tilde{E}_{\rm C}} \right)^{p_1} J_1(\tilde{E}_{\rm C})\,, \end{aligned} \tag{4.20}$$

where

$$p_1 = \frac{\ln\big[J_1(\tilde{E}_{\rm c}) / J_1(E_{\rm ci}) \big]}{\ln(\tilde{E}_{\rm c}/E_{\rm ci})} \tag{4.21}$$

and

$$\begin{aligned} A_1 &= \frac{a_1}{1 + 0.6\, B_{13} (\cos\theta_B)^2} \\ a_1 &= 1 - (\cos\theta_B)^2 \cos\theta_k - (\sin\theta_B)^2 \cos\alpha \\ J(\tilde{E}_{\rm c}) &= \frac{1}{2} + \frac{0.05}{1+B_{13}} + \frac{\sin\theta_B}{4} \\ J(E_{\rm ci}) &= (1-a_1) J(E_{\rm ci}) \end{aligned} \tag{4.22}$$

The central part of this code is dedicated to the actual computation of the emissivity for each of the energy ranges defined above. In particular, we define the total emissivity and that of mode 1 as:

- $\begin{cases} emiss = J_{\rm A} \\ emiss_1 = J_{\rm A1} \end{cases}$
  for $E < E_{\rm ci}$, if $J_{\rm A} > J_{\rm B}$;

- $\begin{cases} emiss = J_{\rm B} \\ emiss_1 = J_{\rm B1} \end{cases}$
  for $E_{\rm ci} \lesssim E \lesssim \tilde{E}_{\rm c}$;
- $\begin{cases} emiss = J_{\rm B}(1-J_{\rm C}) + \dfrac{J_{\rm C}}{1+L} \\ emiss_1 = J_{\rm B1}(1-J_{\rm C}) + J_{\rm C}(1-R_L) \end{cases}$
  for $E > \tilde{E}_{\rm c}$.

Then, the emissivity in the other polarization mode is simply $emiss_2 = 2\,emiss - emiss_1$, from the second of Equations 4.18.
The emissivities in the extraordinary and ordinary polarization modes can be defined by a rotation of the emissivities in the polarization modes 1 and 2 around $\vec{k}$, through the expressions:

$$\begin{aligned} emis_{\rm X} &= (x'_{\rm r}\cdot e^{\rm r}_1)^2 emiss_2 + (x'_{\rm r}\cdot e^{\rm r}_2)^2 emiss_1 \\ emis_{\rm O} &= (y'_{\rm r}\cdot e^{\rm r}_1)^2 emiss_2 + (y'_{\rm r}\cdot e^{\rm r}_2)^2 emiss_1\,, \end{aligned} \tag{4.23}$$

where

$$\begin{aligned} x'_{\rm r}\cdot e^{\rm r}_1 &= \frac{\sin\theta_B \sin\phi}{\sin\alpha_{\rm r}} \\ x'_{\rm r}\cdot e^{\rm r}_2 &= \cos\theta_B \sin\theta_k - \frac{\sin\theta_B \cos\theta_k \cos\phi}{\sin\alpha_{\rm r}} \\ y'_{\rm r}\cdot e^{\rm r}_1 &= \cos\theta_B \sin\theta_k - \frac{\sin\theta_B \cos\theta_k \cos\phi}{\sin\alpha_{\rm r}} \\ y'_{\rm r}\cdot e^{\rm r}_2 &= -\frac{\sin\theta_B \sin\phi}{\sin\alpha_{\rm r}}\,. \end{aligned} \tag{4.24}$$

The total emissivity, as anticipated above, is then given by:

$$emis_{\rm TOT} = \frac{emis_{\rm X} + emis_{\rm O}}{2}\,. \tag{4.25}$$

In the fixed-ions case, $E_{\rm ci}$ is formally set to zero, so only two energy ranges are considered: $E \le \tilde{E}^{\rm fx}_{\rm c}$ and $E > \tilde{E}^{\rm fx}_{\rm c}$, where:

$$\tilde{E}^{\rm fx}_{\rm c} = \frac{\tilde{E}^2_{\rm pe}}{E_{\rm ce}}\,. \tag{4.26}$$

At low energies, the behaviour of the emissivity in the fixed-ions limit is given by:

$$J^{\rm fx}_{\rm B} = \frac{J(\tilde{E}_{\rm c})}{1 - p^{\rm fx} + p^{\rm fx}(\tilde{E}_{\rm c}/E)^{0.6}}\,, \tag{4.27}$$

where

$$p^{\rm fx} = 0.1\,\frac{1+\sin\theta_B}{1+B_{13}} \tag{4.28}$$

and by:

$$J^{\rm fx}_{\rm B1} = \frac{J_1(\tilde{E}_{\rm c})}{0.1 + 0.9\,(\tilde{E}_{\rm c}/E)^{0.4}}\,. \tag{4.29}$$

At the higher energies, instead:

$$J^{\rm fx}_{\rm C} = \frac{4\,\tilde{n}^{\rm fx}}{(1+\tilde{n}^{\rm fx})^2}\,, \tag{4.30}$$

with

$$\tilde{n}^{\rm fx} = \sqrt{1 + \frac{\tilde{E}^2_{\rm pe}}{E_{\rm ce}\,E}}\,. \tag{4.31}$$

In this case:

- $E \lesssim \tilde{E}_{\rm c}^{\rm fx}$: the emissivities are given by:
$$\begin{cases} emiss^{\rm fx} = J_{\rm B}^{\rm fx} \\ emiss_{\rm 1}^{\rm fx} = J_{\rm B1}^{\rm fx} \end{cases};$$
- $E > \tilde{E}_{\rm c}^{\rm fx}$:
$$\begin{cases} emiss^{\rm fx} = J_{\rm B}^{\rm fx}(1 - J_{\rm C}^{\rm fx}) + \dfrac{J_{\rm C}^{\rm fx}}{1 + L^{\rm fx}} \\ emiss_{\rm 1}^{\rm fx} = J_{\rm B1}^{\rm fx}(1 - J_{\rm C}^{\rm fx}) + J_{\rm C}^{\rm fx}(1 - R_L^{\rm fx}) \end{cases}.$$
Here:
$$L^{\rm fx} = \left[\frac{0.17 E_{\rm pe}/E_{\rm c}^{\rm fx}}{1 + X^{\rm fx^4}} + 0.21 e^{-(E/E_{\rm pe})^2}\right](\sin\theta_k)^2 W_L^{\rm fx}$$
$$R_L^{\rm fx} = (\sin\theta_B)^{1/4}\Big[2 - (\sin\alpha)^4\Big]\frac{L^{\rm fx}}{1 + L^{\rm fx}}\,, \tag{4.32}$$
with
$$X^{\rm fx} = \frac{E - E_L}{2\,E_{\rm pe} W_L^{\rm fx}}(1 - \cos\theta_k)^{-1}$$
$$W_L^{\rm fx} = 0.8\Big(\frac{\tilde{E}_{\rm c}^{\rm fx}}{E_{\rm pe}}\Big)^{0.2}\sqrt{\sin(\alpha/2)}\big[1 + (\sin\theta_B)^2\big]\,. \tag{4.33}$$

The rest of the calculation of the emissivities is then the same of the case of free ions, with the *fixed* quantities just defined in place the of the respective ones in the free-ions limit.

Luminosity

The main code is used for the calculation of the luminosity for a specified energy range and for a chosen number of values of the energy and angles θ_k and ϕ. The values of θ_B and B are assigned and remain fixed throughout the calculation. The emissivities are called from the previously-described part of the code and are then integrated in energy and in the angle θ_k, together with the Planck function normalized to $\sigma_{\rm SB}T^4$, where $\sigma_{\rm SB} = 5.6704 \times 10^{-5}\,{\rm erg\ s^{-1}\ cm^{-2}\ K^{-4}}$ is the Stefan-Boltzmann constant. The code returns the luminosity in the free- or fixed-ions limit normalized to the blackbody luminosity.

4.1.1 Plots

The emissivity of the sources was studied as a function of the energy and by considering different magnetic field inclinations and photon propagation directions, in both the limits of free and fixed ions. The angle θ_k was kept fixed at $\pi/4$. The energy range was chosen of $E = 0.001$–10 keV, with 10^4 values considered.

In the first case, the inclination of the magnetic field was fixed, with $\theta_B = \pi/4$, and ϕ was varied. Three values for this angle were considered, $\phi = 0.025$, $\phi = \pi/4$ and $\phi = \pi/2$. This first value was chosen instead of $\phi = 0$, as in [27], because of a degeneracy of the extraordinary and ordinary components. This is a consequence of the fact that the code used in this case calculated the total emissivity from those of modes X and O, while [27] used the modes 1 and 2. The condition $\theta_B = \theta_k$ then resulted in a degeneracy for $\phi = 0$: $\vec{k}$ coincides with $\vec{B}$, so that the plane $\vec{k}$-$\vec{B}$ does not exist and the X- and O-mode can not be defined.
The resulting plot is shown in Figures 4.2 and 4.3, for $B = 10^{13}$ G and $B = 10^{14}$ G, respectively. The plots clearly show three different behaviours of the emissivity in the free-ions case, corresponding to the energy ranges defined above, as well as the line feature at high energies describing the emissivity suppression introduced with Equation 4.16. The latter disappears when a stronger B is considered, in agreement with Equations 4.16 and 4.17 describing the emissivity suppression, and with the definitions of the energies in Equation 4.7. The initial trend of the emissivity is constant with energy, independent of the value of the angle ϕ, followed by a quick decrease, which occurs at higher energies if the magnetic

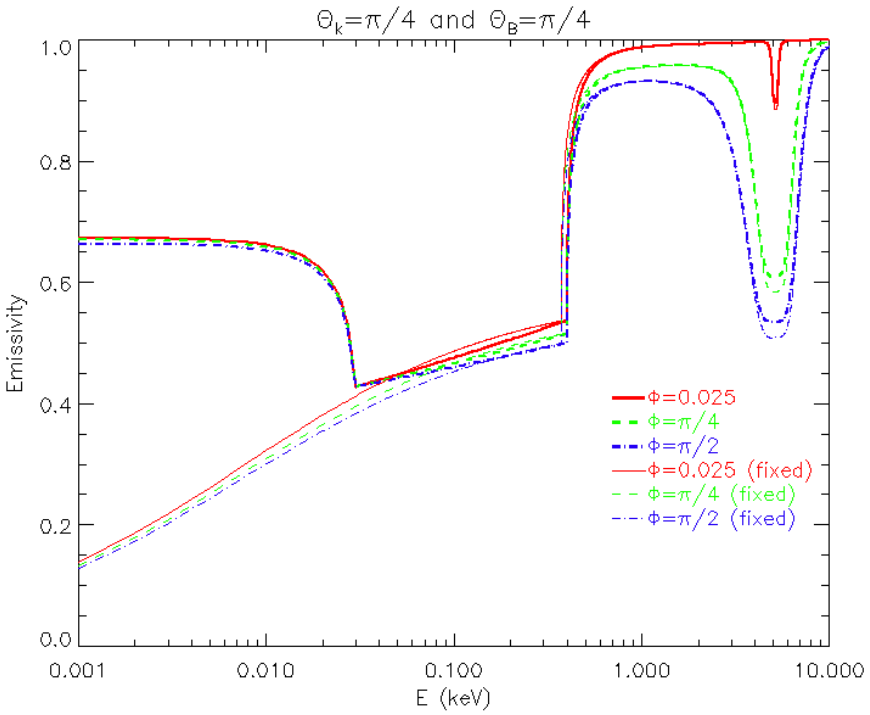

Figure 4.2: The emissivity versus the energy, with $\theta_k = \pi/4$ and $\theta_B = \pi/4$, $B = 10^{13}$ G and three different values of ϕ. The plot is shown for both the free-ions limit (thick lines) and the fixed-ions limit (thin lines). Lines associated to the values of ϕ are depicted with different colors: red for $\phi = 0.025$, green for $\phi = \pi/4$ and blue for $\phi = \pi/2$.

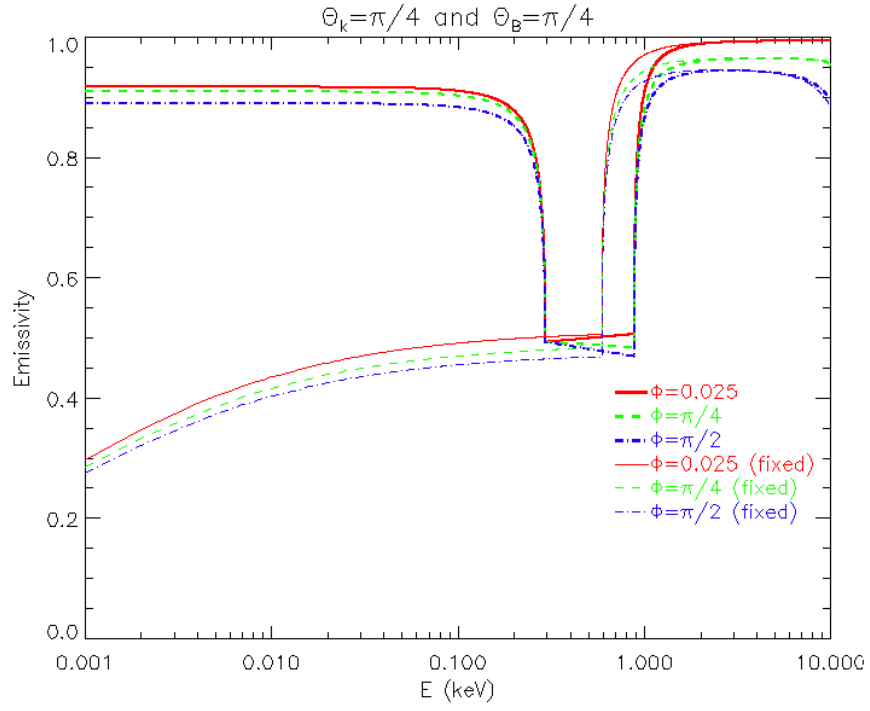

Figure 4.3: Same as Figure 4.3, with $B = 10^{14}$ G.

field is stronger; in the middle energy range the emissivity seems to be, again, roughly constant; at high energies, the emissivity quickly reaches unity independently of the value of B.
In the case of fixed ions, the behaviour of the emissivity at high energies is almost the same as in the free-ions limit, while a substantial difference can be noticed at low energies, as was anticipated in Section 3.1: the emissivity has a smooth increase in the first and second energy ranges, without the sharp edge at $E \sim E_{\rm ci}$ which is evident in the case of free ions.

A second set of parameters was examined, keeping θ_k and ϕ fixed at $\pi/4$ and changing the angle θ_B, with $\theta_B = 0$, $\pi/6$, $\pi/4$ and $\pi/3$. As in the previous case, two values for the magnetic field were considered: Figures 4.4 and 4.5 show the results for $B = 10^{13}$ G and $B = 10^{14}$ G, respectively. The emissivity shows a similar trend as the one described above, but with the low-energy part being more dependent on the change in the angle θ_B.

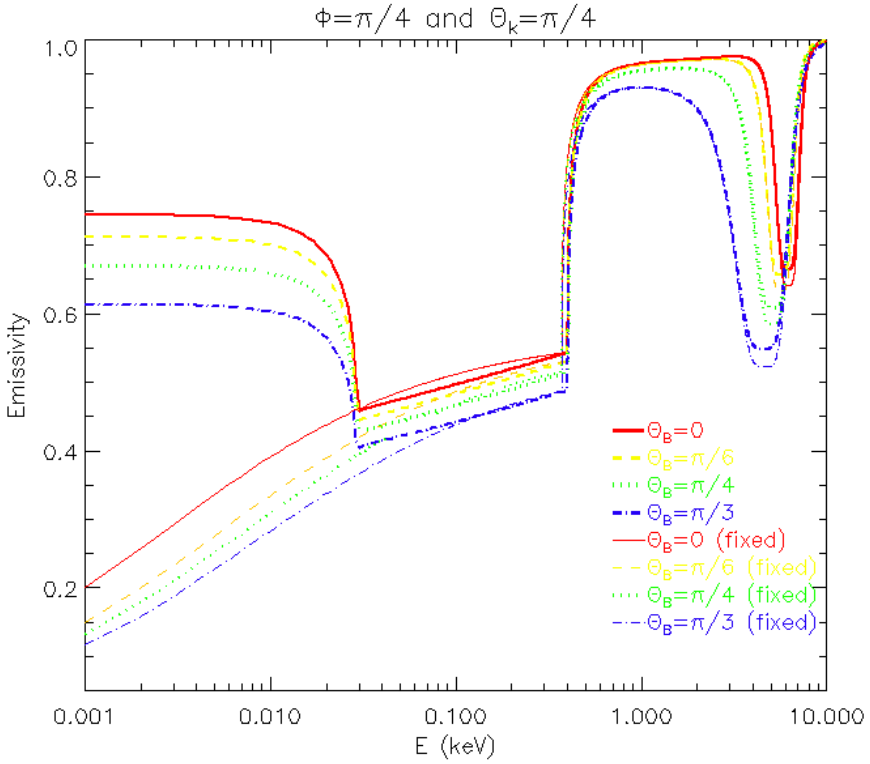

Figure 4.4: The emissivity against energy is shown with $\phi = \pi/4$, $\theta_k = \pi/4$ and $B = 10^{13}$ G. The four values of θ_B are associated with different colors: $\theta_B = 0$ with red, $\pi/6$ with yellow, $\pi/4$ with green and $\pi/3$ with blue. As in the previous example, both limits of free- and fixed-ions are shown, with thick and thin lines, respectively.

The degree of linear polarization can also be analyzed, by considering [27]:

$$\Pi_L = \frac{J_1 - J_2}{2J} = \frac{J_1 - J_2}{J_1 + J_2}\,, \tag{4.34}$$

where J_1 and J_2 are the emissivities called $emiss_1$ and $emiss_2$ above, respectively. The numerical results are shown in the case of fixed θ_B in Figure 4.6, for both cases of free and fixed ions. The polarization mode 1 is responsible for the trend at positive values of Π_L, while mode 2 for the negative part. In the case of free-ions, the polarization degree is constant for energies below ~ 0.3 keV and shows a slight dependence on the angle ϕ. The fixed-ions limit is quite similar to the free-ions limit at higher energies, as expected, both attaining a maximum of $\Pi_L \sim 0.45$; at lower energies, instead, the polarization degree in the fixed-ions case decreases with the energy and its seems to be less dependent on the value of the angle ϕ.

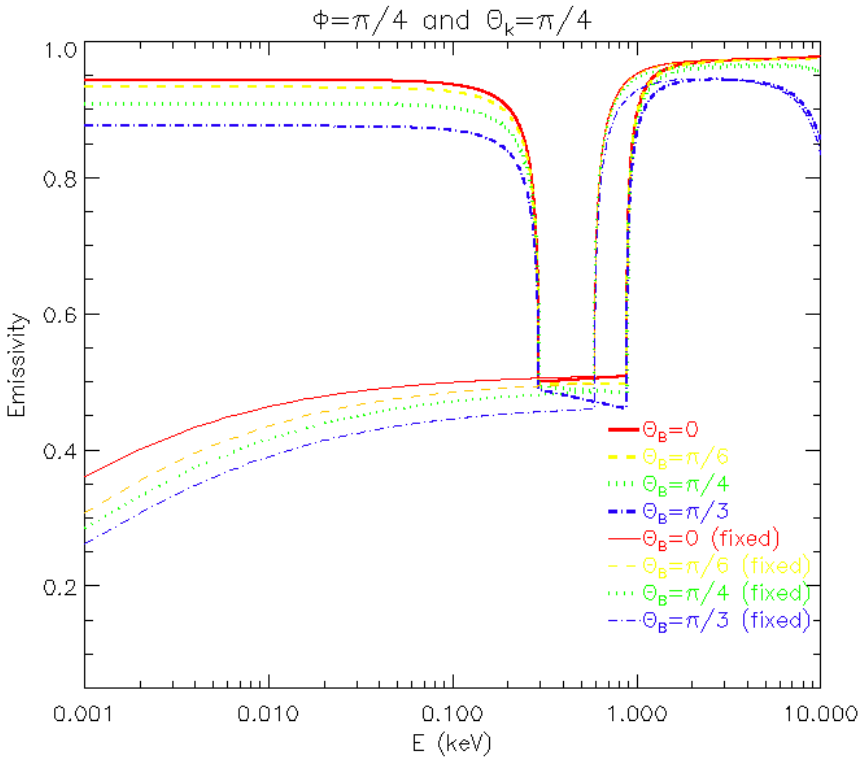

Figure 4.5: Same as Figure 4.4, with $B = 10^{14}$ G.

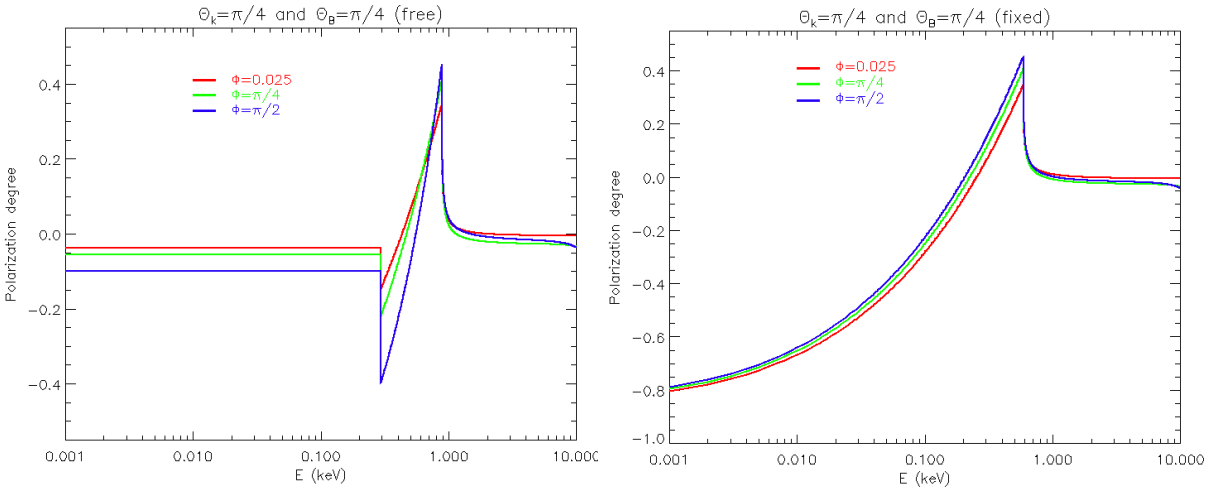

(a) (b)

Figure 4.6: Polarization degree as a function of energy with $\theta_B = \pi/4$, $\theta_k = \pi/4$ and $B = 10^{13}$ G. The same three values of ϕ of Figure 4.2 have been considered: $\phi = 0.025$ (red), $\pi/4$ (green) and $\pi/2$ (blue). Panel (a) shows the results in the free-ions limit, while panel (b) the ones in the fixed-ions case.

Considering, instead, the emissivities in the O- and X-mode ($emiss_{\rm O}$ and $emiss_{\rm X}$), the results are shown in Figure 4.7, again for both the free- and fixed-ions limits and for three different values of the angle ϕ. The behaviour at higher energies ($E \gtrsim 1$ keV) is quite similar to the previous case, with a slightly smaller value of the maximum attained by the polarization degree; as above, the free- and fixed-ions limits show a rather similar behaviour in the high-energy range. At lower energies, the polarization fraction in the

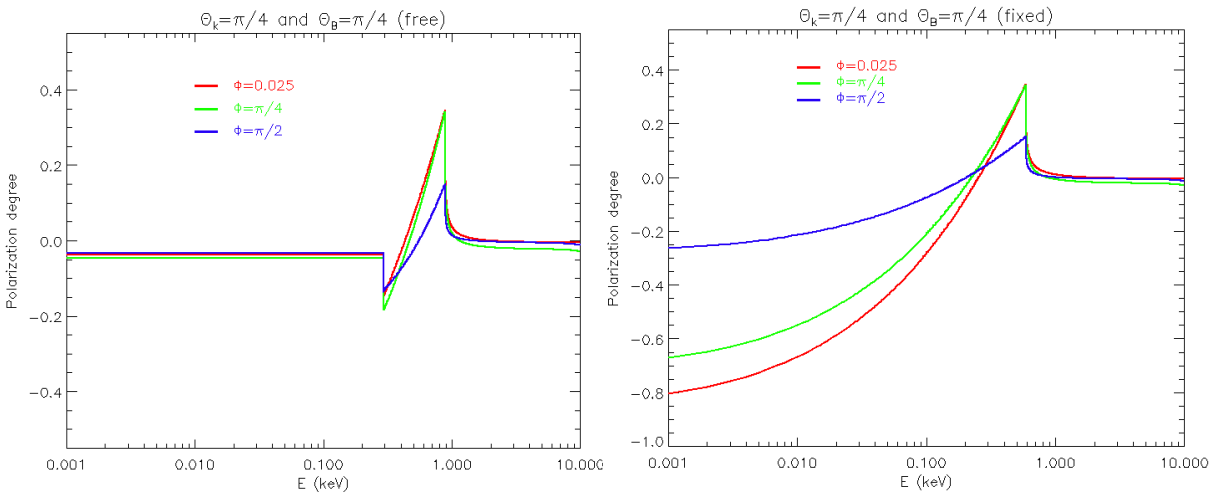

(a) (b)

Figure 4.7: Same as Figure 4.6, but considering the emissivities of modes O and X instead of 1 and 2.

free-ions limit is constant, at $\Pi_L \sim -0.5$, for all values of the angle ϕ; in the fixed-ions limit, instead, there is a dependence of the polarization degree on ϕ, with the case of $\phi = 0.025$ being quite similar to the behaviour of the mode 2, while the other two being closer to zero.

4.1.2 Contour plots

The behaviour of the emissivity was also analyzed by means of contour plots, again considering different sets of parameters.

At first, the emissivity was plotted considering the variation in energy and angle ϕ for $B = 10^{13}$ G, while keeping both θ_k and θ_B fixed at $\pi/4$. The energy range is the same as in the plots described above, i.e. $E = 0.001$–10 keV, while ϕ is in the interval $\phi = [0.025, \pi/2]$. Figures 4.8 and 4.9 show the results in the free- and fixed-ions limits, respectively. The values of the emissivity in these contour plots can be compared with the plot of Figure 4.2, where the angles $\phi = 0.025$, $\phi = \pi/4$ and $\phi = \pi/2$ were considered, resulting in an overall consistency of the trend as a function of both energy and ϕ.

In an analogous way, a contour plot of the emissivity was obtained as a function of the energy and of the angle θ_B, as shown in Figures 4.10 and 4.11. As for the previous case, $B = 10^{13}$ G, the energy is in the range $E = 0.001$–10 keV and θ_k is kept constant at $\pi/4$; instead, $\phi = \pi/4$ and θ_B is considered in the interval $\theta_B = [0, \pi/2]$. The comparison with the plot of Figure 4.4 results, also in this case, in agreement: this can be noticed particularly in the stronger dependence shown at low energies on the angle variation in the case of free ions, which is not present in Figure 4.8.

Finally, the emissivity was examined as a function of the angle θ_B and the magnetic field strength B, while keeping $\theta_k = \pi/4$, $\phi = \pi/4$ and the energy fixed. Three different values of the energy were chosen, $E = 0.001$ keV, $E = 0.1$ keV and $E = 10$ keV: the respective contour plots can be seen in Figures 4.12, 4.13 and 4.14, in both free- and fixed-ions limits. The values considered for the angle θ_B are in the range $\theta_B = [0, \pi/2]$, while the magnetic field strength, in units of 10^{13} G, is in the range $B_{13} = 0.1$–51.1.
These plots can be compared with the ones of Figures 4.4 and 4.5. At low energies, the emissivity increases for stronger B up to reach a value very close to 1 in the free-ions limit and about 0.45 in the fixed-ions case. At $E = 0.1$ keV, the emissivity level increases consistently in the limit of free ions, while it remains below ~ 0.6 and more or less B-independent in the fixed-ions limit. Lastly, the emissivity at high energies appears to be quite similar in the two limits. There is a tendency of the emissivity, common to all energies, to decrease for higher values of θ_B, especially in the presence of smaller magnetic fields.

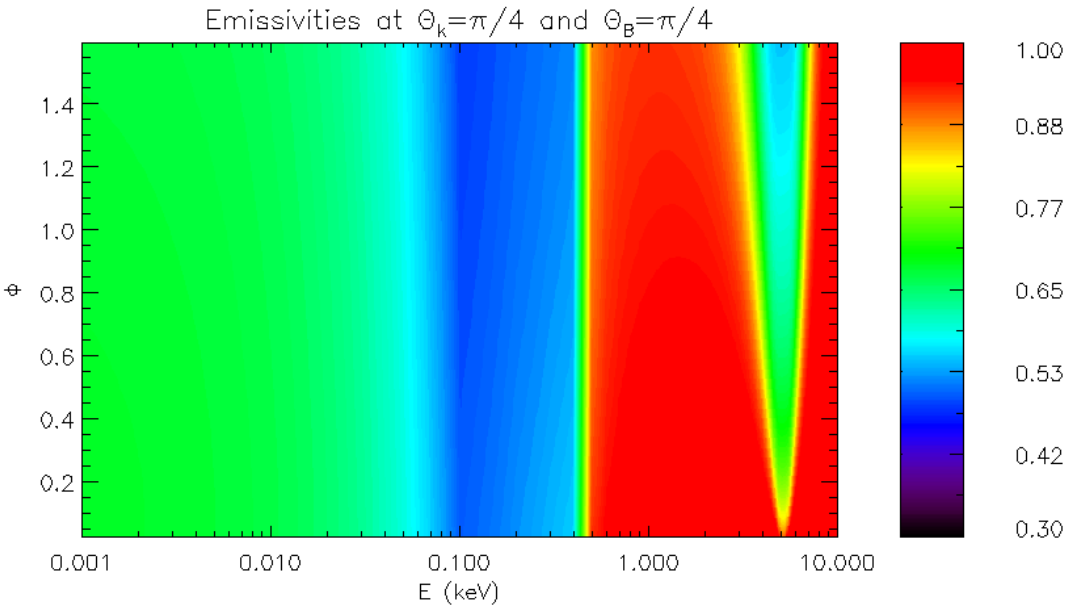

Figure 4.8: The emissivity (free-ions limit) is shown as a function of energy and ϕ, with θ_k and θ_B fixed at $\pi/4$ and $B = 10^{13}$ G.

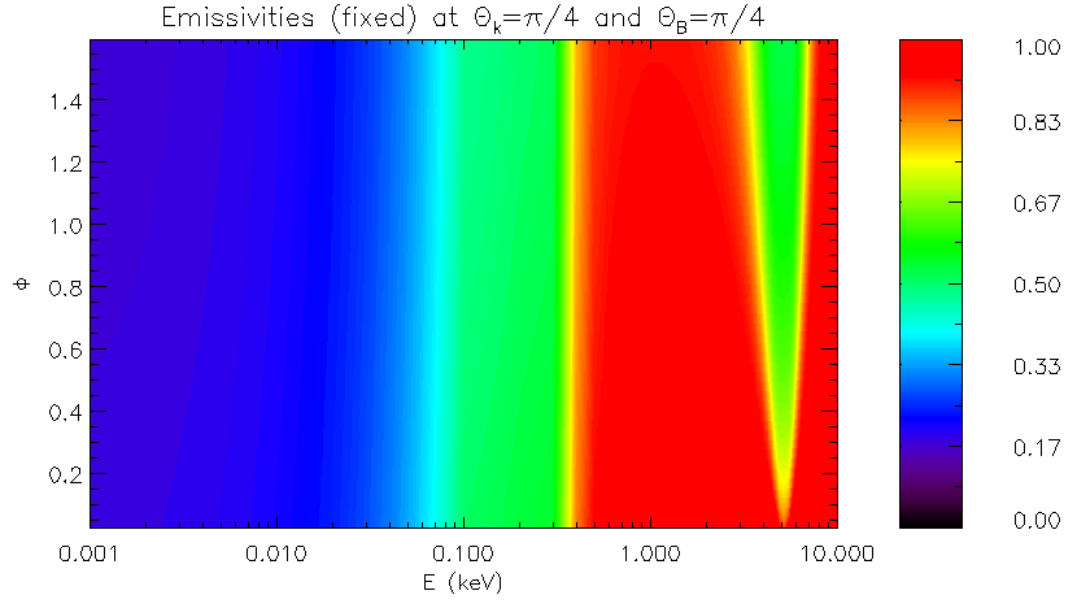

Figure 4.9: Same as Figure 4.8, in the fixed-ions limit.

4.2 Ray-tracer

The main goal of this thesis is a systematic study of the observed spectral and polarimetric properties of highly magnetized neutron stars endowed with a condensed surface. To achieve this, a ray-tracer code was employed: the original code, presented in [28], allows a systematic study of X-ray light curves from cooling neutron stars, accounting for the propagation of the radiation field in a strongly magnetized medium and incorporating the relevant radiative processes. It also allows to select the emission properties (either a blackbody (BB), a bare surface or an atmosphere) and accounts for QED effects (the vacuum birefringence) through the approximated approach illustrated in Section 3.2. In this work, the attention was put on the emission from a condensed surface as compared with the BB emission, so the atmospheric

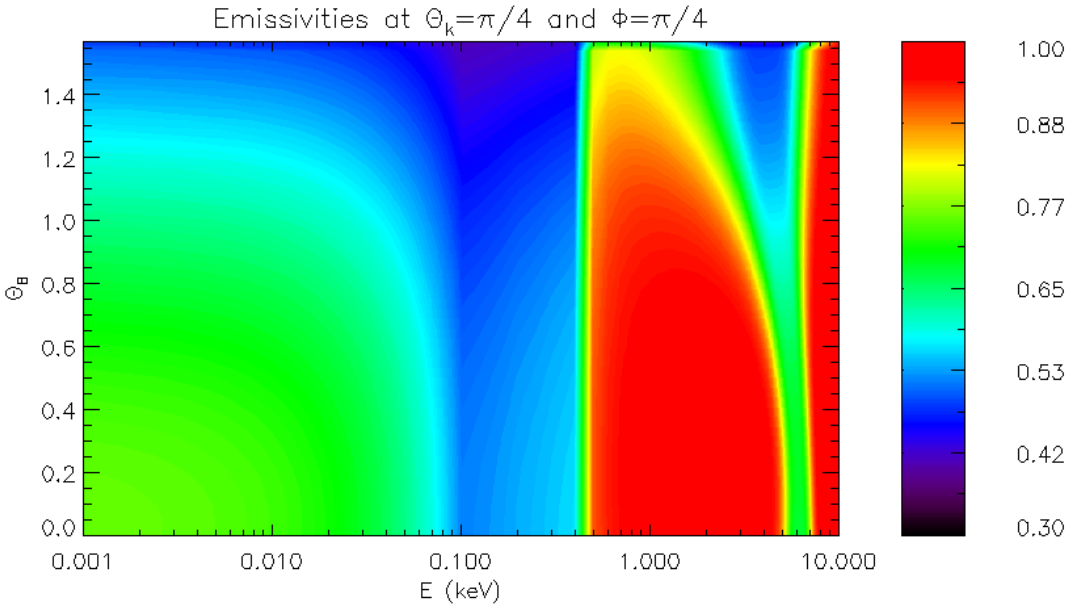

Figure 4.10: This contour plot shows the emissivity as a function of the energy and of the angle θ_B, with $\theta_k = \pi/4$, $\phi = \pi/4$ and $B = 10^{13}$ G, in the case of free ions.

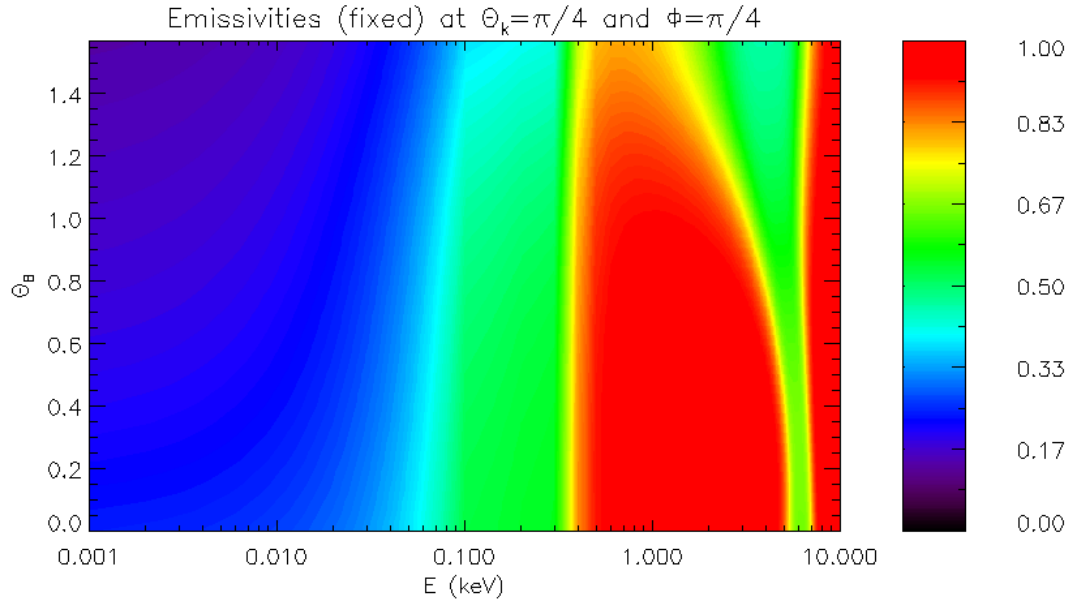

Figure 4.11: Same as Figure 4.10, in the fixed-ions limit.

part of the code was eventually ignored.

Source parameters

After assigning the radius and the mass, taken to be respectively $M = 1.4\,M_\odot$ and $R_{\rm NS} = 12\,$km, the code computes the general relativity corrections. A *compactness parameter* is defined:

$$x_g = \frac{R_{\rm Schw}}{R}\,, \tag{4.35}$$

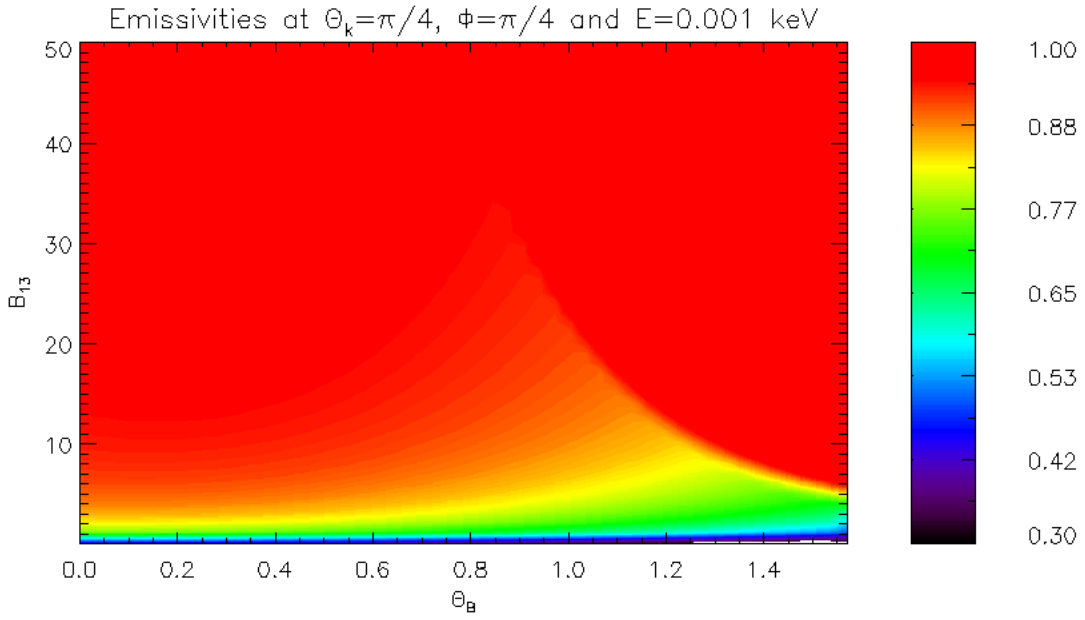

(a)

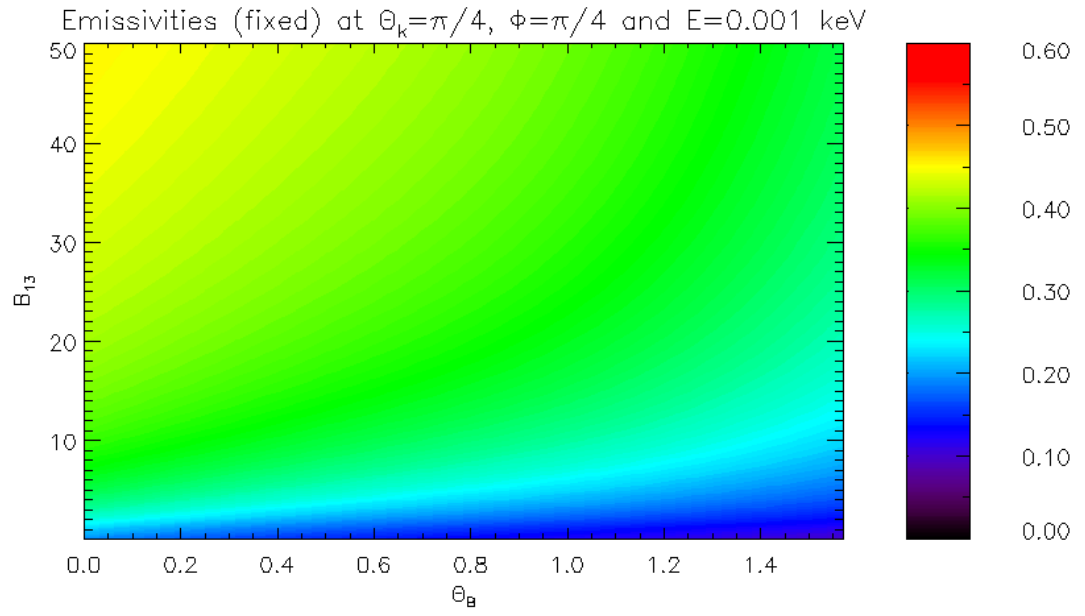

(b)

Figure 4.12: The contour plots for the emissivity as a function of energy and magnetic field strength. B is in units of 10^{13} G. Panel (a) shows the results for the free-ions limit, while panel (b) those for the fixed-ions case.

where $R_{\rm Schw} = 2GM/c^2 \approx 2.98 M/M_\odot$ km is the *Schwarzschild radius*. Since $x_g \sim 1/5$–$1/2$ for neutron stars, GR plays an important role, as discussed in [19]. Because of this, the quantities describing the radiation emitted from these sources, such as energy, temperature and luminosity, are redshifted: they appear to be smaller in the remote observer's reference frame with respect to the local inertial frame. The apparent radius, instead, increases: the effect of *light bending* results in more than half of the star's surface being visible at the same time, affecting the observed emission. The magnetic field is also affected by GR corrections (see [32]). After introducing the redshift parameter $g_{00} = 1 - x_g = 1 - 2.98\, M/R$, and after selecting the value of the polar component of the magnetic field ($B_{\rm P}$) at the surface, the GR

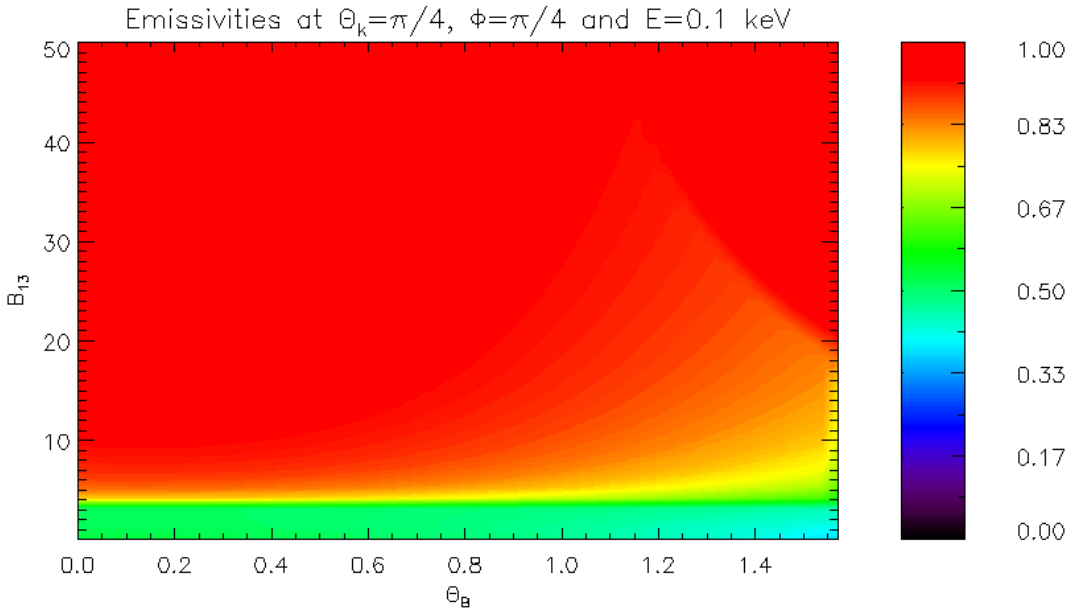

(a)

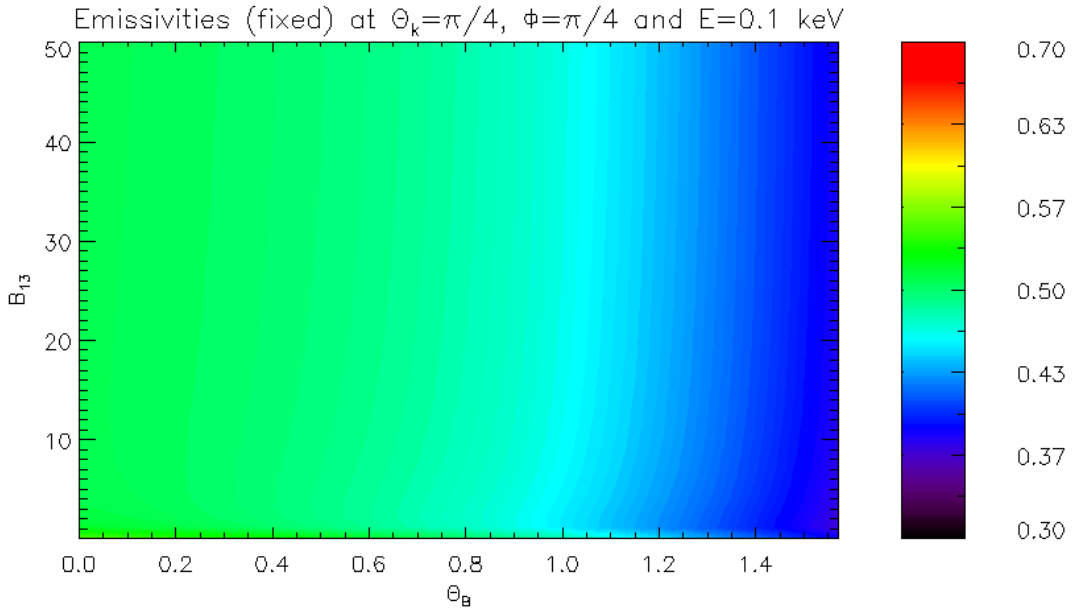

(b)

Figure 4.13: Same as Figure 4.12, but for $E = 0.1$ keV.

correction on the magnetic field can be approximated as:

$$B_{\rm P}^{\rm GR} = \frac{B_{\rm P}}{-3\,x_g^{-3}\left[\log g_{00} + \dfrac{1}{2}x_g(x_g+2)\right]} \tag{4.36}$$

for $r \lesssim 5\,R_{\rm NS}$.
The polarization of the radiation is not affected in a significant way by GR effects, because the scale-length along which the polarization plane rotates due to GR effects is much bigger than the one associated with vacuum birefringence, as described in Section 3.2.

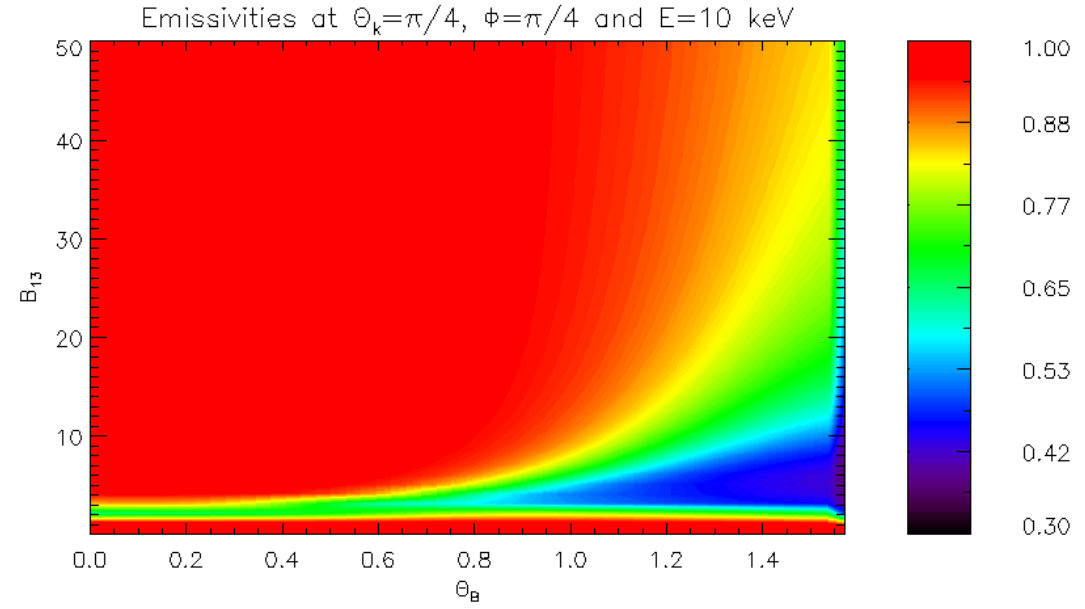

(a)

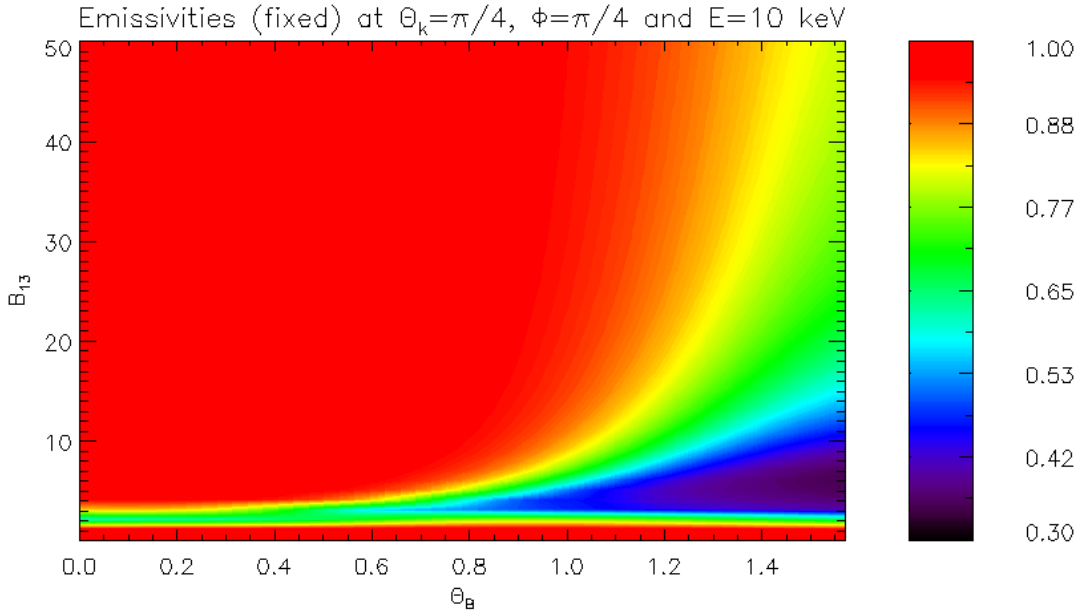

(b)

Figure 4.14: Same as Figure 4.12, but for $E = 10$ keV.

Emission model

The code gives the possibility to limit the region of emission from the surface, either by considering a polar cap or an equatorial belt, specifying the semi-aperture angle. In the case of the equatorial belt, which is the case considered in this study, a limit in the angle ϕ can be chosen as well, resulting in a "broken" belt. When blackbody emission is assumed, the intrinsic polarization fraction is given in input. In this case, it is kept at 100% polarization in the X-mode.
The considered temperature distribution on the surface is the one given by a magnetic dipole, with $T = T_{\rm P} \left(\cos\theta_B\right)^{1/2}$ and the polar value $T_{\rm P}$ specified in input. This profile gives $T = 0$ at the equator, i.e. $\theta_B = 90°$: for this reason, a truncation temperature is given, and the final temperature profile is $T =$

$\max(T, T_{\text{truncation}})$. The rest of the surface is set at a much lower temperature, with $T_{\text{limit}} = 0.05\sqrt{g_{00}}$ keV and $T_{\text{truncation}}$ bigger than this limit.

The working energy range is ~ 0.5–8 keV, with 32 values. The angular grid on the surface is made of 100×100 points in co-latitude and azimuth, with respect to the frame of reference described in Figure 4.15. The phase is sampled in 10 bins. Next, the angles χ and ξ (see Figure 4.15) are given.

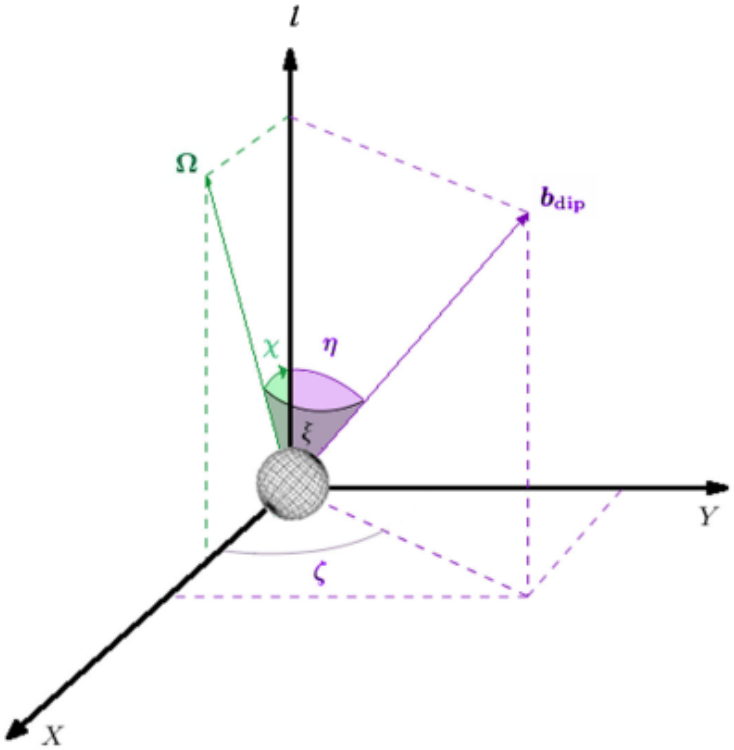

Figure 4.15: From [26]. The Z-axis coincides with the direction of the line of sight (LOS) l. X, coincident with the projection of the rotation axis in the plane of the sky, lies in the plane formed by l and Ω, the star's spin axis, while Y is perpendicular to both X and Z. $\mathbf{b}_{\text{dip}}$ is the unit vector of the magnetic dipole axis, whose direction is fixed by the angles η and ζ, calculated from the Z-axis and the X-axis, respectively. The angle χ is between the spin axis and the LOS, while ξ between Ω and $\mathbf{b}_{\text{dip}}$.

Main

The main code is aimed to calculate the flux, the polarization degree and the polarization angle of the emitted radiation as a function of the energy and of the phase, considering one of the emission models for the condensed surface (blackbody, free-ions limit, fixed-ions limit). This is done in the frame of reference of the LOS, described in Figure 4.15

The components of the unit vector $\mathbf{b}_{\text{dip}}$ are computed at the beginning, in order to obtain the polar and cartesian components of the magnetic field, both in the reference frame of $\mathbf{b}_{\text{dip}}$ and of the LOS. The adiabatic radius is then calculated as described in Equation 3.25 if the QED effects are taken into consideration, or it is taken as $r_{ad} = R_{\text{NS}}$ if they are neglected. The magnetic field is then computed at this radius, together with its components, and the GR corrections are applied to $B(r_{ad})$, if the condition $r_{ad} < 5\,R$ is satisfied.

At this point, the code gives the temperature distribution based on the emission geometry chosen at the beginning, i.e. polar, equatorial or whole surface: in the first two cases, the temperature outside the delimited area is fixed at $T = T_{\text{limit}}$, defined above. The next step is the calculation of the intensity

distribution in the case of a solid surface, which gives the three contributions for the BB emission and the condensed surface in the free- and fixed-ions limit: in the latter case, the code calls the functions described in Section 4.1, giving the total emissivity of the radiation in the two limits.
The calculation for the intensity distribution for the solid surface was implemented so that the radiation coming from outside the emission region (the equatorial belt in this case) would be non-polarized black-body emission: in order to do so, the polarization was fixed at 50 for both the X- and O-mode when the condition $T \leq T_{\rm limit}$ was satisfied. For $T > T_{\rm limit}$, the emissivity was computed as before.

Lastly, the light curves of the emission (Stokes parameter $\mathcal{I}$ as a function of the rotational phase) are computed and the Stokes parameters relative to the linear polarization ($\mathcal{Q}$ and $\mathcal{U}$) are rotated and integrated over the part in view of the surface through the expressions [26]:

$$\begin{aligned} F_Q &= \int_0^{2\pi} d\Phi_S \int_0^1 d(\sin\bar{\Theta}))^2 (n_X - n_O)\cos(2\alpha) \\ F_U &= \int_0^{2\pi} d\Phi_S \int_0^1 d(\sin\bar{\Theta}))^2 (n_X - n_O)\sin(2\alpha)\,, \end{aligned} \tag{4.37}$$

where F_Q and F_U are the "fluxes" of the Stokes parameters [33], and n_X and n_O are the photon intensity in the extraordinary and ordinary modes, respectively: these generally depend on the photon energy E and direction, and on the position on the star surface of the emission point. The angles Φ_S and Θ_S (to which $\bar{\Theta}$ is related) fix the point on the surface from which the photons are emitted.
This allows to compute the polarization observables, through their definition in Equation 3.30. The code returns in output the total flux, polarization degree and polarization angle as a function of energy and phase, as well as the same quantities phase- and energy-integrated.

The original code was later adapted to obtain different results. The first modification allowed to compute the phase average of the polarization degree and angle, at a fixed energy and for different geometries, i.e. as a function of the angles χ and ξ, as is seen in figure 7 of [26].
Then, these observables were integrated also in energy.
Finally, the energy-phase quantities were computed for each pair of angles ξ and χ.

Chapter 5

Results

This chapter illustrates the results of the runs of the ray-tracing code, described in the previous chapter, obtained for different geometrical configurations of the emitting surface, for the two emission models: blackbody radiation and emission from a condensed surface, both in the free-ions and in the fixed-ions limit.

Plots

First of all, the flux, polarization degree and polarization angle obtained from the computation described in Section 4.2 were plotted against energy or against the phase, depending on whether the phase-integrated or the energy-integrated results were considered. Both these scenarios are contained in the same plotting code, where the geometry of the emission region is selected, together with its semi-aperture angle. Afterwards, the temperature profile is given, with $T_{\rm P}$ and $T_{\rm truncation}$, together with the intrinsic polarization fraction of X-mode over O-mode photons for the blackbody case. A completely polarized blackbody model has been used for its simplicity in the implementation and for the possibility of comparison with respect to the more complicated, and physically more consistent, case of the condensed surface. Also, a 100% polarized BB can be considered as a simplified representation of the real scenarios such as magnetized atmospheres, these not being the focus of this work.
All the models have been obtained considering a purely dipolar external magnetic field. Finally, a specific geometry is selected by specifying the angles χ and ξ. We obtain the behaviors of flux, polarization degree and polarization angle for each emission model. Phase-integrated models are plotted in the 0.5–8.0 keV band, while energy-integrated ones in the entire rotation cycle (i.e. $\gamma \in [0, 2\pi]$).

The first analysis was made for an equatorial belt, with an initial semi-aperture of 18° in magnetic colatitude; the temperatures are chosen as $T_{\rm P} = 0.45$ keV and $T_{\rm truncation} = 0.39$ keV; the magnetic field is $B = 5 \times 10^{14}$ G and the blackbody emission is considered to be completely polarized in the X-mode. The geometrical configurations explored are: $\chi = 89°$, with $\xi = 0°$ and 30°, and $\chi = 0°$, with $\xi = 5°$ and 88°.

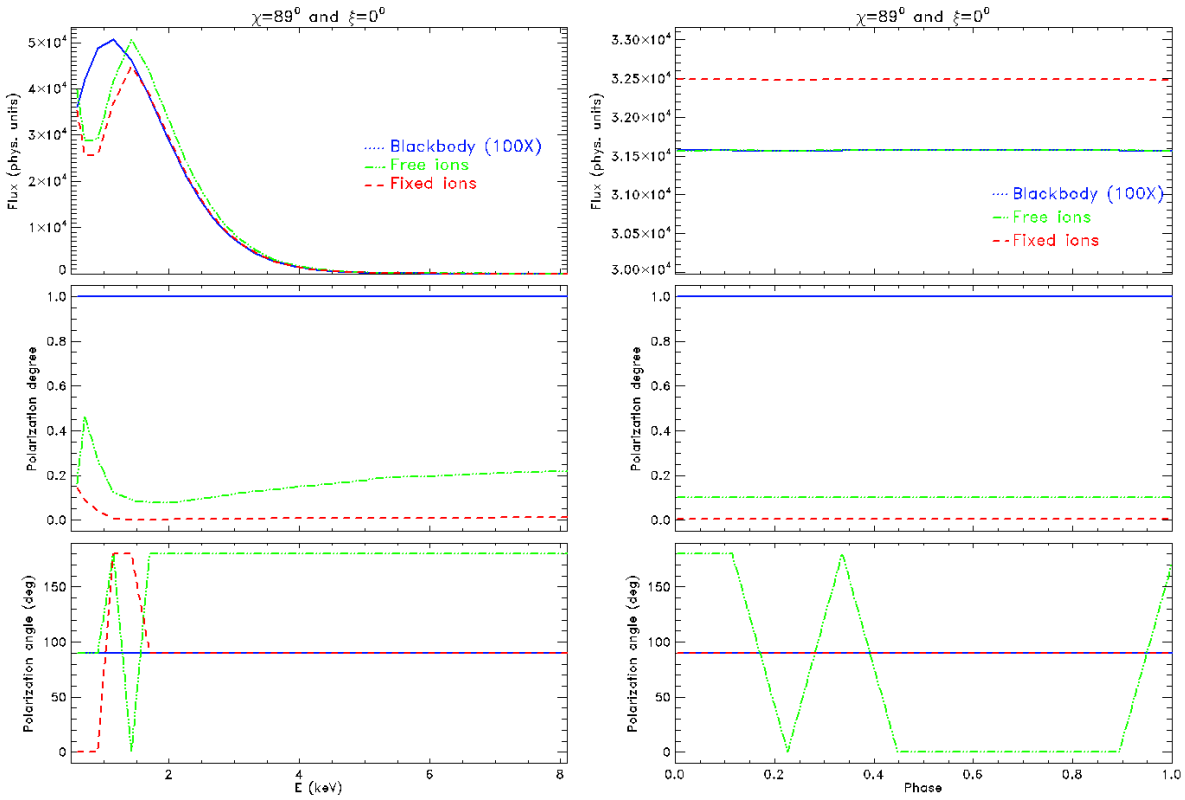

(a) (b)

Figure 5.1: Energy-dependent (panel a) and phase-dependent (panel b) flux, polarization degree and polarization angle for $\chi = 89°$ and $\xi = 0°$. The three emission models are compared: blackbody 100% polarized (dotted blue line), condensed surface in the free-ions limit (dash-dotted green line) and in the fixed-ions limit (dashed red line), in the energy-dependent and phase-dependent cases, in panel (a) and (b), respectively.

The results for $\chi = 89°$ $\xi = 0°$ are presented in Figure 5.1. The energy-dependent plots show that, while the spectrum is rather similar in the three cases (apart for energies below $\sim$ 2 keV), the polarization degree differs substantially: it is equal to 1 for the BB at all energies, and it reaches much lower values in the case of the condensed surface (below 0.5 in the free-ions limit and below 0.15 in the fixed-ions case). For what concerns the polarization angle, it is constant at 90° in the case of the BB, since it is 100% polarized in the X-mode; in the case of free-ions, χ_{pol} is almost constant at 180° (O-mode), apart from the lower energies; in the fixed-ions limit, instead, the initial oscillation is between 0° and 180° (O-mode photons), with $\chi_{pol} = 90°$ at high energies ($E \gtrsim 2$ keV).
In the phase-dependent case, the flux is constant in all three cases, since the magnetic axis coincides with the rotation axis and the magnetic (and rotational) equator of the star is always in view: since the belt is considered to be continuous, the observed spectral properties are expected not to change as the star rotates. For the same reason, the polarization observables are also phase-independent. The polarization degree has very low values in the case of the condensed surface, with $\Pi_L \sim 0.1$ and $\Pi_L \sim 0$ in the free- and fixed-ions limits, respectively. For what concerns the polarization angle, its behaviour shows that photons are polarized in the O-mode in the case of free-ions and in the X-mode in the fixed-ions limit, at all phases.

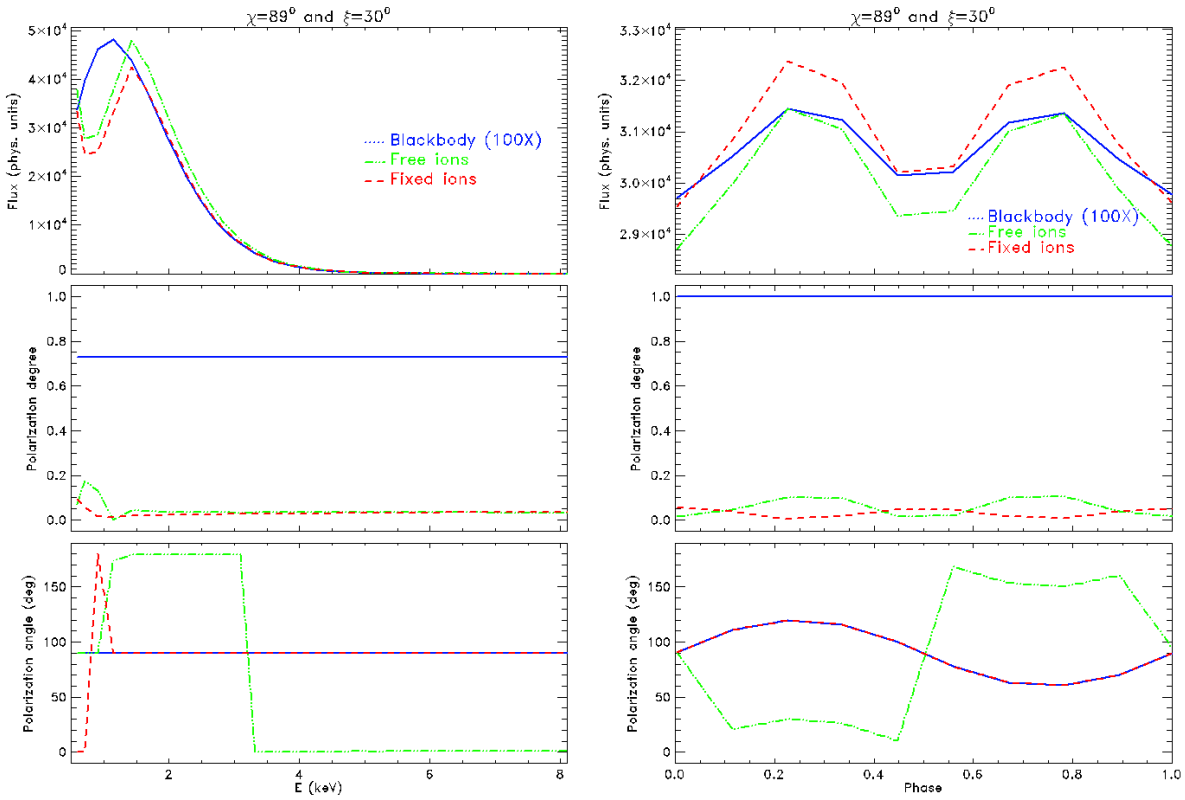

(a) (b)

Figure 5.2: Same as Figure 5.1, but for $\chi = 89°$ and $\xi = 30°$.

In the case of $\chi = 89°$ and $\xi = 30°$, the plots for the energy-dependent and phase-dependent quantities are shown in Figure 5.2.
In the energy-dependent plots, the polarization degree in the case of BB ($\Pi_L \sim 0.75$) is always much higher than for the free- and fixed-ions limits ($\Pi_L < 0.2$ for both). The polarization angle is still constant at 90° (X-mode) for the blackbody emission, and for the fixed-ions limit at high energies, while it mainly attains values between 180° and 0° (O-mode) for the free-ions limit.
The phase-dependent plots show a double-peaked flux in all three cases; the polarization degree is below 0.15 in both the limits of free- and fixed-ions; the polarization angle oscillates smoothly around 90° for both the BB (the reason for which the phase-averaged polarization degree is not exactly 1) and the fixed-ions limit, while it oscillates around 0° in the free-ions case.

The second value of χ chosen was $\chi = 0°$, the rotation axis aligned with the LOS, with $\xi = 5°$ and $\xi = 88°$ the two different inclinations of the magnetic axis with respect to the spin axis. Like for the previous case, we present the three different scenarios for the blackbody, the free-ions and the fixed-ions limit, for both energy-dependent and phase-dependent results.

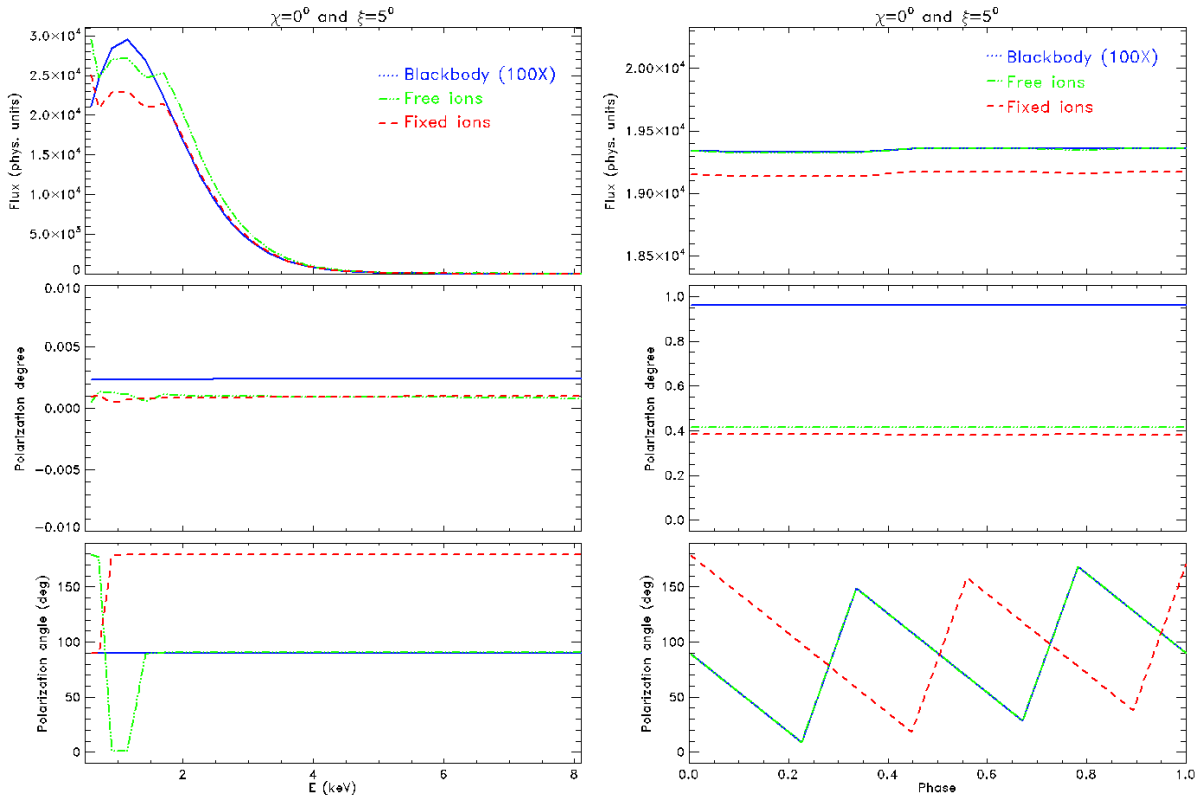

(a) (b)

Figure 5.3: Same as Figure 5.1, but for $\chi = 0°$ and $\xi = 5°$.

In the case of $\xi = 5°$ (Figure 5.3), the energy-dependent polarization degree is close to zero for all emission models, which can be understood from the geometry of the configuration: the star's rotation axis is aligned with the LOS, so it is observed from the rotation pole. Since the emission comes from an equatorial belt, this explains why the phase-averaged polarization fraction is extremely low in all cases. The polarization angle is of 90° for the BB and the free-ions case (except for lower values of the energy), so the photons are in the X-mode, while it quickly reaches 180° (O-mode) in the fixed-ions limit.
The phase-dependent plots show a roughly constant flux for all three cases, again a consequence of the considered geometry; the polarization fraction is close to 1 for the BB, and it is around 0.4 for both limits of free- and fixed-ions. The polarization angle has a *swing* between 0° and 180° in all the three cases.

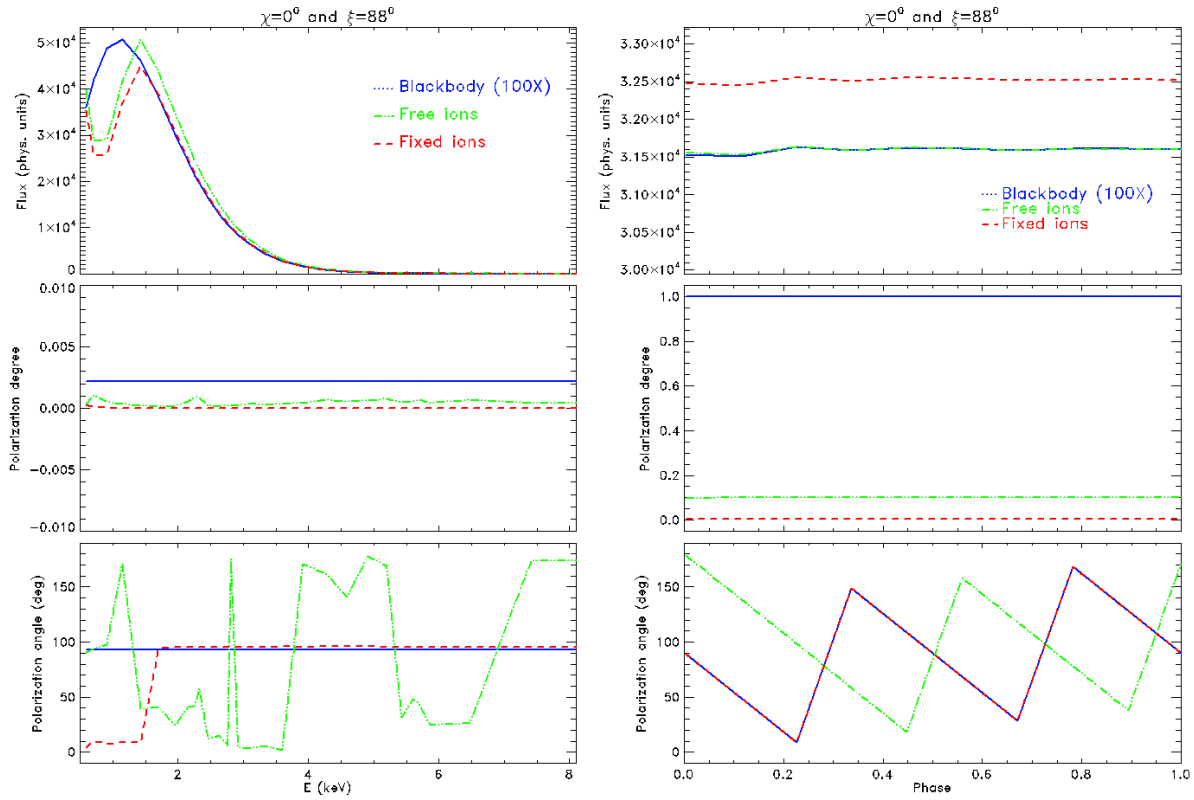

(a) (b)

Figure 5.4: Same as Figure 5.1, but for $\chi = 0°$ and $\xi = 88°$.

Finally, the results in the case of $\chi = 0°$ and $\xi = 88°$ (Figure 5.4) show energy-dependent polarization degrees close to zero: as for the previous scenario, this can be understood when considering the geometry of the configuration, with the rotation axis aligned with the LOS. The polarization angles reaches 90° for the BB and the fixed-ions case (X-mode photons); the free-ions limit is described by a complicated trend of χ_{pol}, as a consequence of the very low polarization degree.
In the case of the phase-dependent results: $\Pi_L = 1$ for the BB and $\Pi_L < 0.1$ for the free- and fixed-ions limits; the polarization angle attains values between 0° and 180° in all cases.

A useful comparison is the one between results obtained with QED effects accounted for and those where they have been neglected. Considering the same aperture of 18° for the equatorial belt, and the angles $\chi = 89°$ and $\xi = 30°$, we can compare the following plots (Figure 5.5), where QED effects are ignored, to the ones of Figure 5.2.

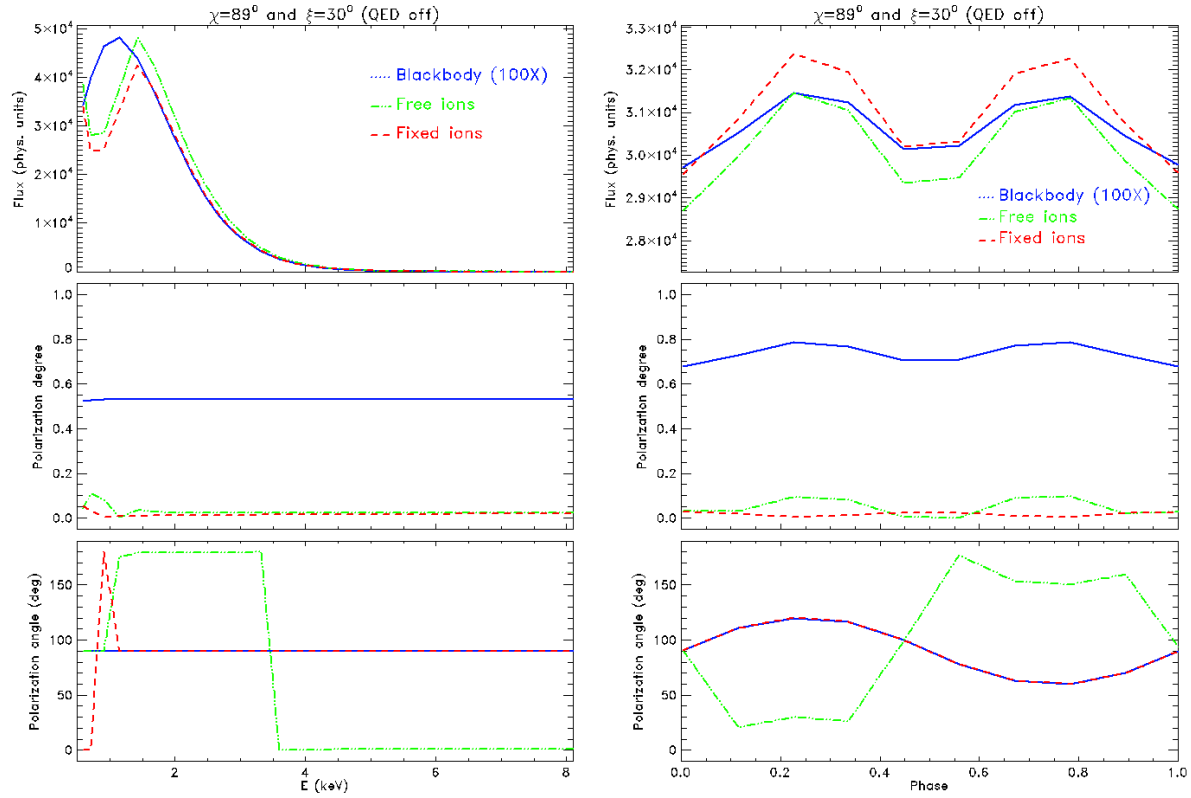

(a) (b)

Figure 5.5: Same as Figure 5.1, but for QED effects not accounted for.

In the energy-dependent case, the most noticeable difference with respect to the plots of Figure 5.2 is in the polarization degree, showing lower values with respect to the case in which QED effects have been accounted for: in the case of the blackbody, in particular, the polarization fraction decreases from $\Pi_L \sim 0.75$ to $\Pi_L \sim 0.5$.
In the same way, the phase-dependent polarization degree decreases in the absence of QED effects, going from $\Pi_L = 1$ to $\Pi_L \sim 0.7$ in the case of the BB.

Another useful comparison can be made between different apertures of the emitting region. Considering a semi-aperture angle of 45° and the same angles $\chi = 89°$ and $\xi = 30°$, we can compare the plots in Figure 5.6 to the ones of Figure 5.2.

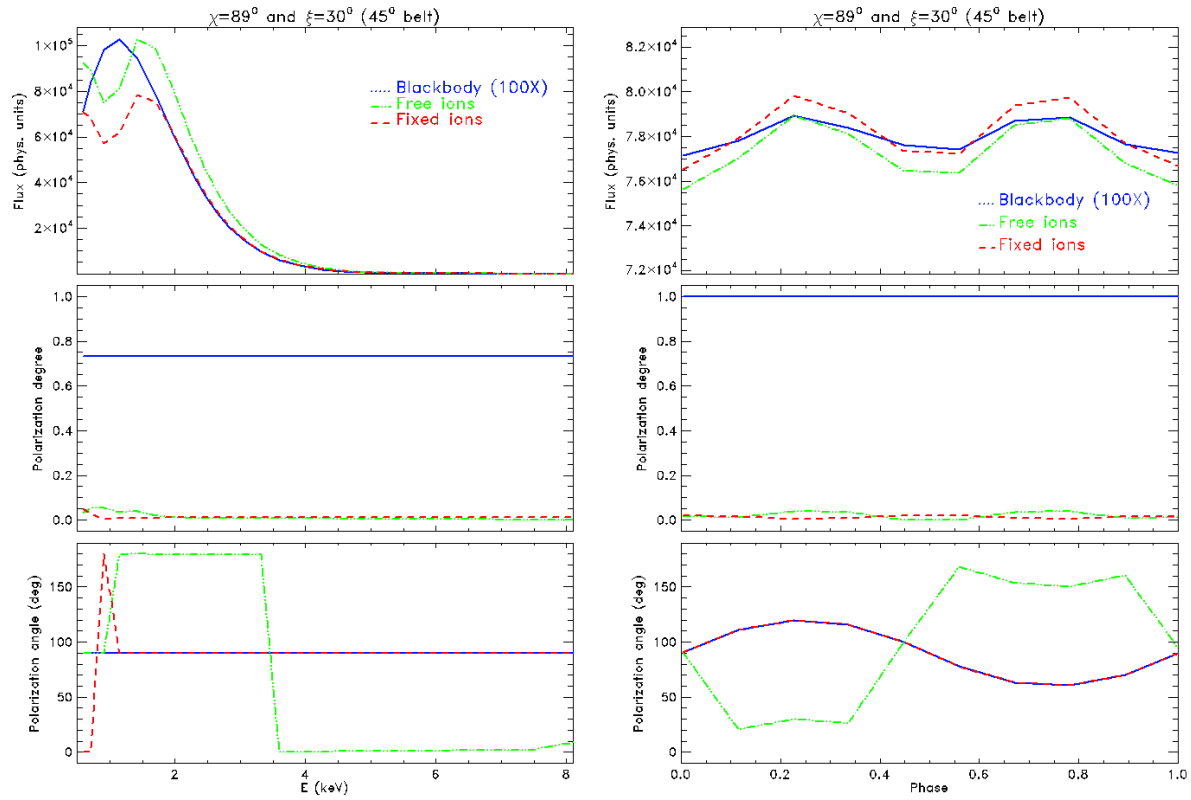

(a) (b)

Figure 5.6: Same as Figure 5.1, but with a semi-aperture angle of 45° for the equatorial belt.

In both cases of energy-dependent and phase-dependent plots, the polarization degree of the blackbody emission is not affected by the increase in the aperture of the equatorial belt; on the other hand, the polarization fraction for the free- and fixed-ions limits decreases when the belt's extension increases, with $\Pi_L < 0.05$ in both cases. Instead, the polarization angle does not change its behaviour.

Finally, another analysis can be made by considering a "broken" belt, with a limit of 30° in the azimuth, with the same values of the angles $\chi = 89°$ and $\xi = 30°$.

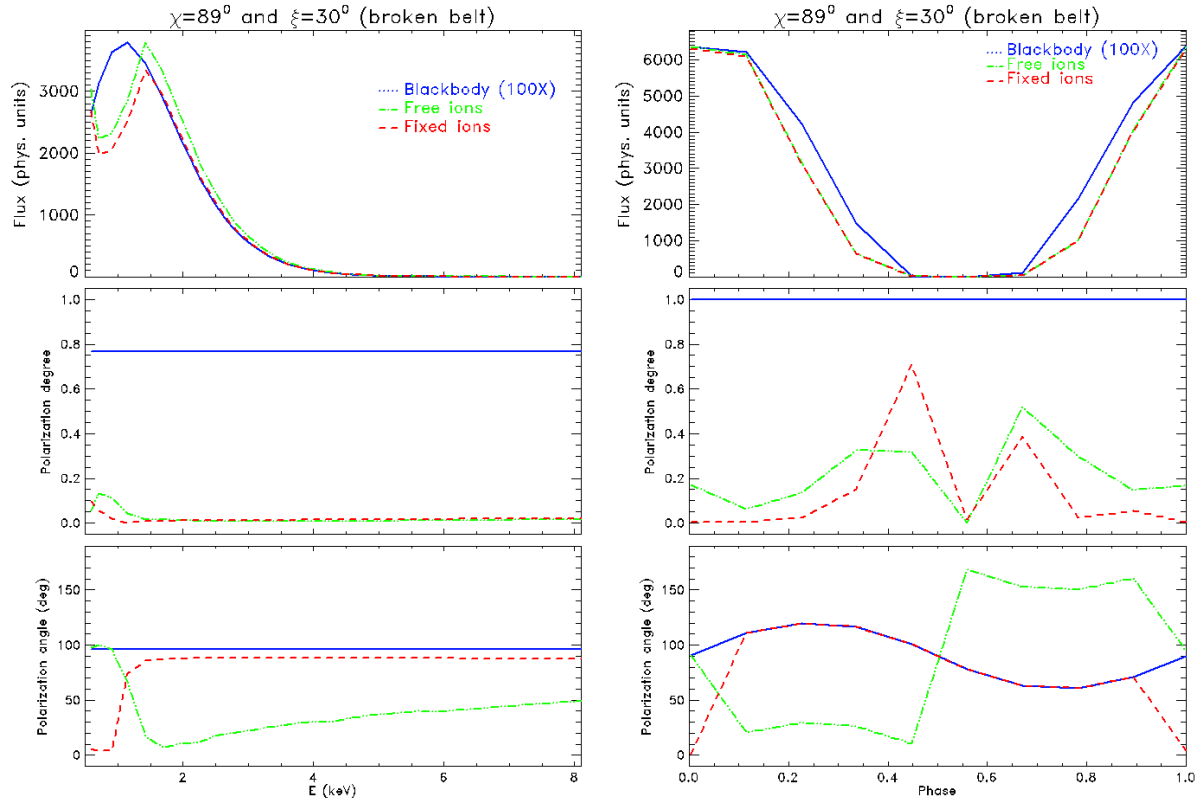

(a) (b)

Figure 5.7: Same as Figure 5.1, but with a limit of 30° in azimuth for the equatorial belt.

Comparing the results of Figure 5.7 to the plots of Figure 5.2, the energy-dependent polarization degree is shown to vary a little between the two configurations: it slightly decreases in the case of blackbody emission, while it has a small increase for the free- and fixed-ions limits. The polarization angle has a roughly similar trend for the BB and for the fixed-ions case; in the free-ions limit, instead, it is close to 90° at low energies, then it has a decreasing trend followed by a slight increase up to $\sim 50°$.
In the phase-dependent case, the flux shows a decrease for certain values of the phase ($\gamma \sim 2.8$–4.1 rad), as a consequence of the presence of a "broken" belt: as the star rotates, the emission region may become completely invisible to the observer. The polarization degree experiences a strong increase in the free-ions limit (up to $\Pi_L \sim 0.5$) and in the fixed-ions limit (Π_L reaches ~ 0.7); the sudden minima are explained by the behaviour of the flux as a function of phase. The polarization angle, on the other hand, has a similar behaviour with respect to the case of the continuous belt.

Contour plots

A further analysis can be made by considering the contour plots of the polarization degree and the polarization angle as functions of both energy and phase, in the same ranges as the ones used in the plots described above. For example, the plots of Figures 5.8–5.10 show the results in the case of $\chi = 89°$ and $\xi = 30°$, which are in agreement with the plots in Figure 5.2. As expected, the polarization fraction for the blackbody emission is very close to 1; the one for the free-ions case shows higher values for low energies (up to even ~ 0.4 at energies below ~ 1 keV) and two peaks in phase; in the same way, the polarization degree in the fixed-ions case, with lower values with respect to the free-ions limit, is slightly bigger at low energies and presents three peaks in phase.

For what concerns the polarization angle, the blackbody emission shows an oscillation in phase around 90° for all energies. In the case of free-ions, the emission from the condensed surface has an oscillation around 90° (X-mode photons) at low energies, while the angle oscillates around 0° or 180° (O-mode) at energies roughly above 1 keV; the outcome is reversed in the fixed-ions limit.

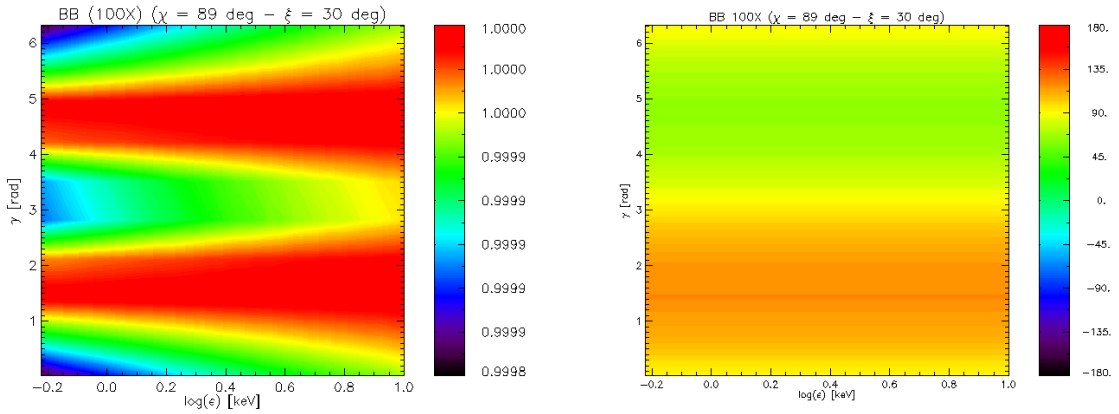

(a) (b)

Figure 5.8: Contour plot of the polarization degree (panel a) and the polarization angle (panel b) as a function of the energy and the phase, in the case of blackbody emission.

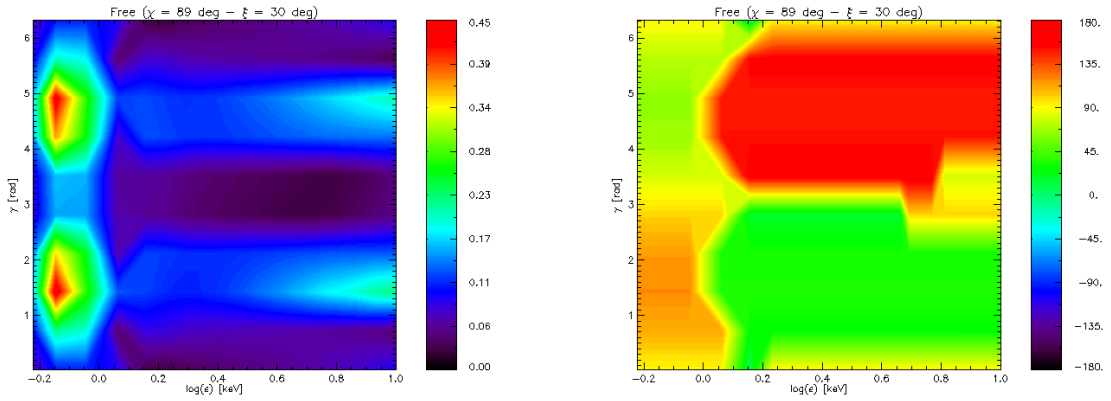

(a) (b)

Figure 5.9: Same as Figure 5.8, but for the condensed surface in the free-ions limit.

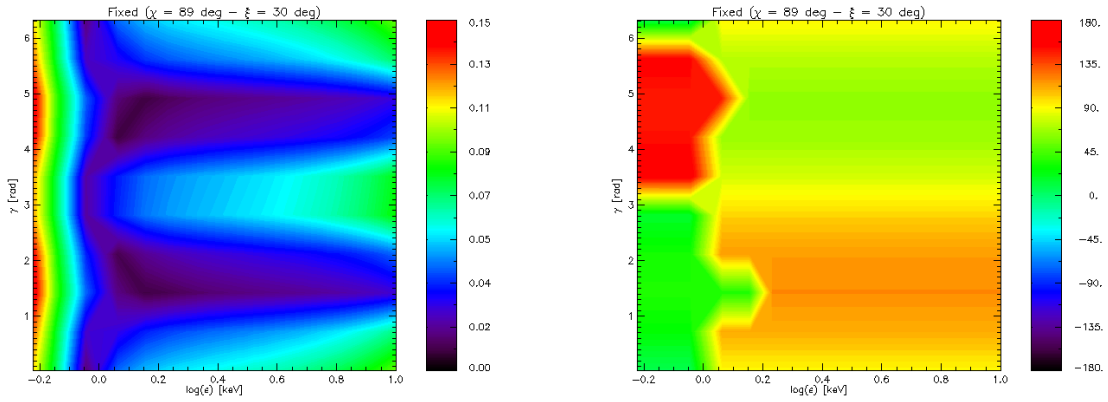

(a) (b)

Figure 5.10: Same as Figure 5.8, but for the condensed surface in the fixed-ions limit.

5.1 Phase-averaged and energy-integrated results

In this section, the results for the phase-averaged calculations are presented, followed by the phase-averaged and energy-integrated plots.
In the first case, the polarization degree and angle are averaged in phase and initially showed at a fixed energy, as functions of the angles ξ and χ, both in the range 0°–90°. Figures 5.11–5.13 show the contour plots of the polarization degree and of the polarization angle, in the case of blackbody, condensed surface in the free-ions limit and in the fixed-ions case.
The polarization degree in the case of blackbody emission is close to 1 for higher values of χ, when the rotation axis is misaligned from the line of sight, and for low and very high values of ξ, when the magnetic axis direction is either very close to or very distant from the spin axis. On the other hand, very low values of the polarization degree are encountered if the magnetic pole enters in view during the star rotation, for all values of inclination of the magnetic field. For what concerns the case of free- and fixed-ions, the polarization degree is generally quite low: it is below 0.4 in the free-ions limit and below 0.2 in the fixed-ions limit. The highest values occur when the magnetic axis is almost aligned to the rotation axis, and the angle between the spin axis and the LOS is in the range $\chi \sim 20°$–$30°$. These results are compatible with the plots described at the beginning of this chapter.
The polarization angle in the case of blackbody emission is close to 180° for lower values of χ with low or high values of ξ, or for high values of both angles. In the case of low values of both angles, this is due to the fact that the polarization degree is close to zero in this case. χ_{pol} is closer to 0° (O-mode photons) for middle values of χ and $\xi > 30°$; for all other values of the angles, $\chi_{pol} = 90°$, so the photons are polarized in the X-mode. The polarization angle exhibits, in general, an almost reversed behaviour in the two cases of free- and fixed-ions: in most configurations, when $\chi_{pol} = 90°$ (X-mode) in one limit, it will reach either 0° or 180° (O-mode) in the other one; also, photons can be polarized in the O-mode (χ_{pol} either 0° or 180°) in both cases. The only ranges of angles for which the photons are polarized in the X-mode in both limits are $\chi \sim 40°$–$50°$ and $\xi \sim 0°$–$20°$, so when the magnetic field axis is almost aligned with the rotation axis, which is in turn inclined roughly 45° from the LOS.

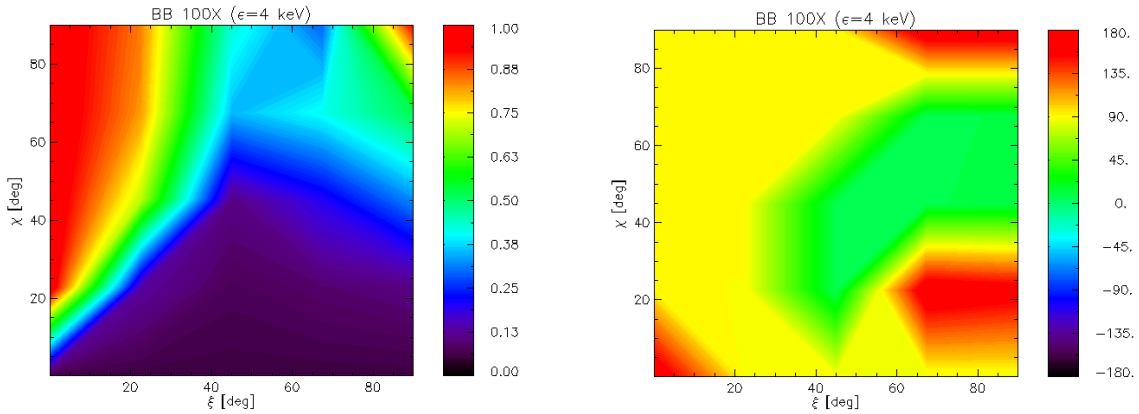

(a) (b)

Figure 5.11: Contour plot of the phase-averaged polarization degree (panel a) and polarization angle (panel b) for the blackbody emission, as a function of the angles ξ and χ, at the fixed energy $E = 4$ keV.

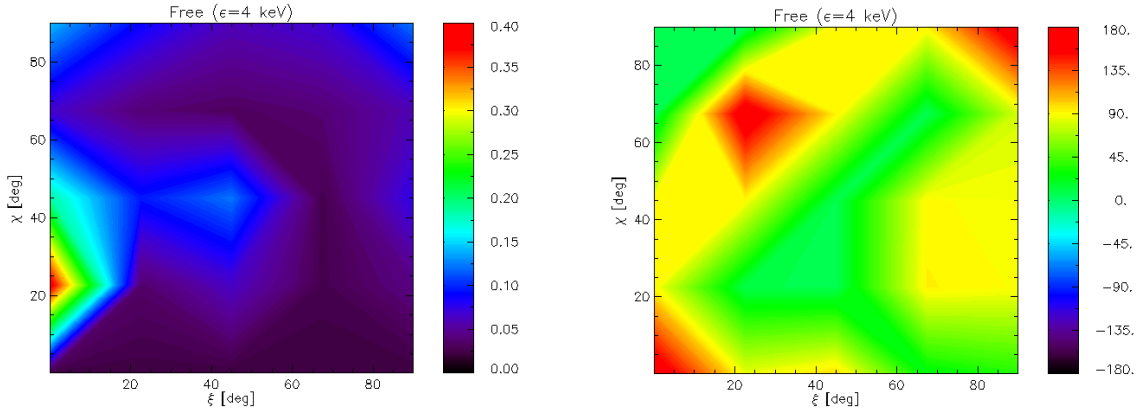

(a) (b)

Figure 5.12: Same as Figure 5.11, but for the condensed surface in the free-ions limit.

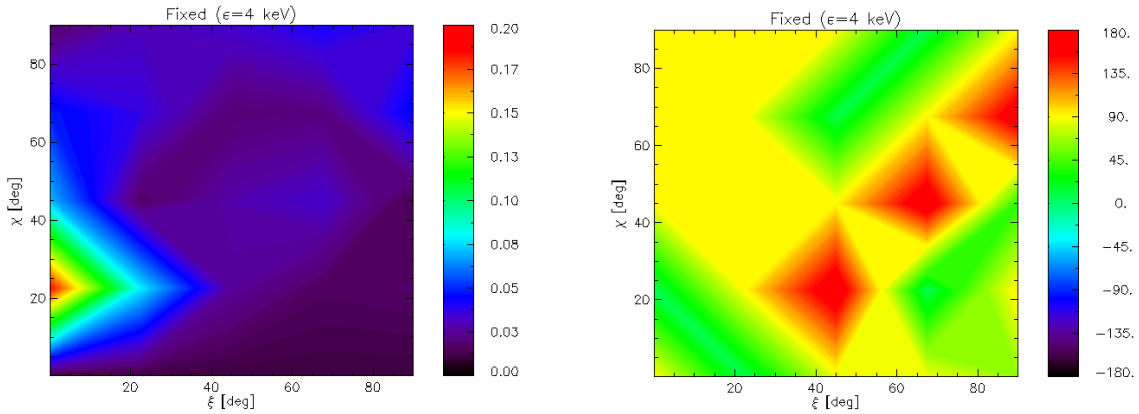

(a) (b)

Figure 5.13: Same as Figure 5.11, but for the condensed surface in the fixed-ions limit.

These results were also considered in an energy range of $E = 2$–8 keV, with the polarization degree and angle being therefore both averaged in phase and integrated in energy. The following figures show the analogous contour plots described above, after integration over the energy.

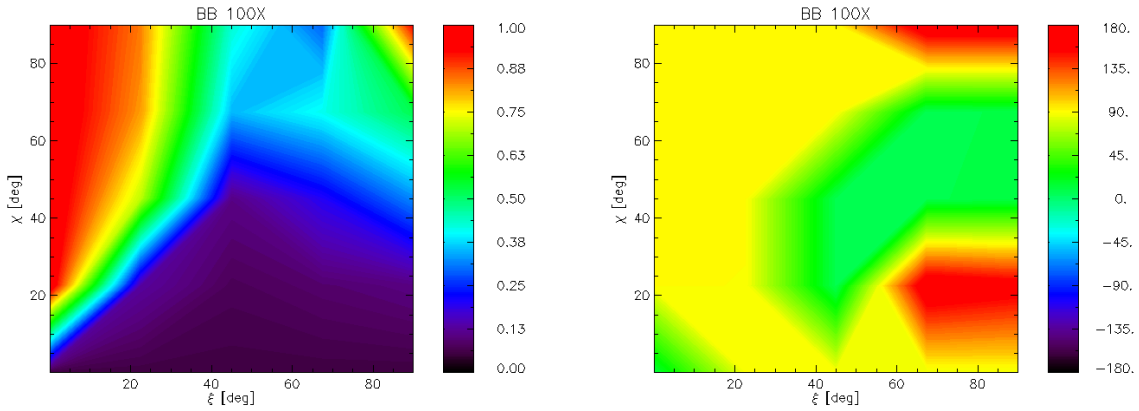

(a) (b)

Figure 5.14: Contour plot of the polarization degree and polarization angle, both averaged in phase and integrated in energy, in the case of blackbody emission and as functions of the angles χ and ξ.

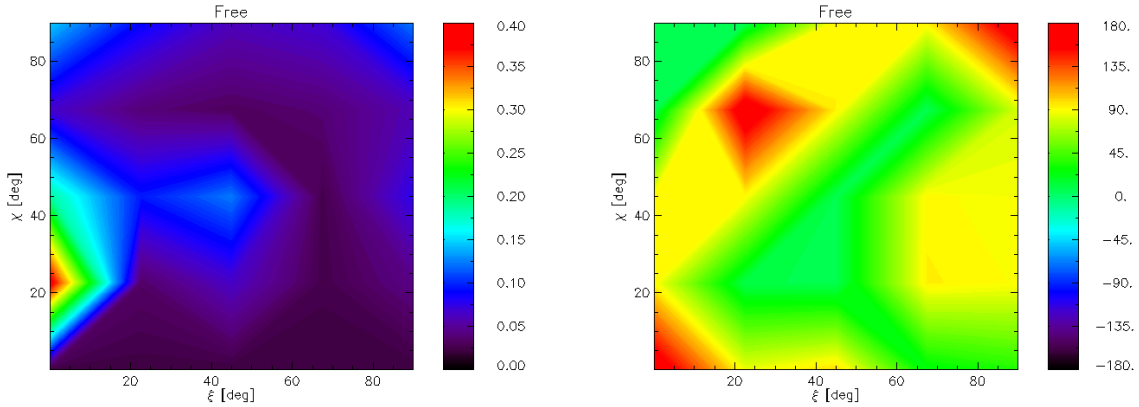

(a) (b)

Figure 5.15: Same as Figure 5.14, but for the condensed surface in the free-ions limit.

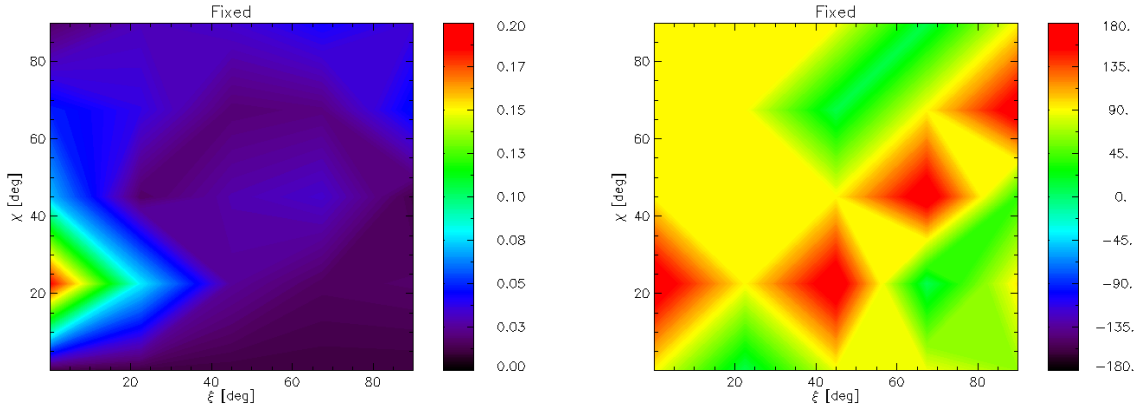

(a) (b)

Figure 5.16: Same as Figure 5.11, but for the condensed surface in the fixed-ions limit.

Chapter 6

Discussion and conclusions

This work has been focused on the radiation emitted from neutron stars endowed with strong magnetic fields, specifically magnetars. For low enough surface temperature and sufficiently high magnetic field, two conditions easily met in magnetar sources, a phase transition sets in the surface layers, turning the gaseous atmosphere into a condensate. Magnetic condensation changes the structure of matter, affecting the spectral and polarization properties of the emitted radiation. These effects were studied by means of some numerical tools, developed in previous works by several authors and slightly modified to perform our systematic analysis. This produced the results shown and described in Section 5, which are now going to be discussed.

The results refer to a star with $M = 1.4\,M_\odot$ and $R_{\rm NS} = 12$ km, and with a dipole magnetic field at the pole of strength $B_{\rm P} = 5 \times 10^{14}$ G. A dipole-induced temperature distribution was considered, with $T_{\rm P} = 0.45$ keV and $T_{\rm truncation} = 0.39$ keV. General relativistic effects are accounted for.
Two emission models were considered: blackbody radiation and emission from a condensed surface, both in the free-ions and the fixed-ions limit. The blackbody photons are assumed to be 100% polarized in the extraordinary mode. A blackbody model was used to mimic the real scenarios of magnetized atmospheres, for which a specific model was not considered, since it goes beyond the goals of this thesis.
The overall conclusion that can be drawn from the results shown in the previous chapter is that the spectral properties are not very sensitive to the surface emission model that is considered: spectral measurements alone are therefore not enough to draw firm conclusions on the physical mechanisms that determine the emission from the surface. On the other hand, the polarization pattern has shown to be strongly affected by the type of emission, since the polarization degree is much lower ($\Pi_L \lesssim 0.4$ overall) for a condensed surface compared with emission from a magnetized atmosphere (modelled in this work by the 100% polarized blackbody model). Hence, performing polarimetric studies together with the spectral ones can be of great value in better understanding the emission model of the observed sources.
This work was focused, in particular, on the effect of the changes of the geometrical configurations on the polarization observables. The polarization degree decreases considerably in the case of a nearly-aligned rotator ($\chi \sim 0°$) viewed along its rotation axis, when the quantities are energy-dependent, for all the emission models: this is due to the fact that the different polarizations are averaged over the phases, resulting in an overall low polarization of the observed radiation. The same configuration in the phase-dependent case, in fact, does not show this decrease. Generally speaking, the phase-dependent analyses can give more information on the intrinsic polarization of the emitted radiation.
On the other hand, the highest values of Π_L in the case of the condensed surface were obtained in the case of the LOS aligned with the equator: since the radiation is emitted from an equatorial belt, and it is always in view to the observer, this results is consistent.
Considering the polarization angle, its value reflects the mode of polarization of the photons: since the code used here considered the X-axis of the reference frame at infinity to be coincident with the projection of the rotation axis in the plane of the sky, the polarization angle is $\chi_{pol} = 90°$ when the photons are polarized in the X-mode, and 0° (or equivalently 180°) for the O-mode. Photons emitted from a condensed surface tend to be mostly polarized in one mode at low energies ($E \lesssim 1$ keV), while the opposite polarization mode dominates for higher values of the energy. The polarization angle only depends on the geometry of the configuration and not on the polarization fraction: in fact, for a given pair of angles χ

and ξ, the oscillation amplitude of the polarization angle swing as a function of the rotational phase is the same regardless of the polarization degree behaviour or of the emission model.
This clear dependence of Π_L and χ_{pol} on the geometrical configuration makes the polarization observables, and therefore polarimetric studies, extremely useful in the understanding of the source geometry, specifically the inclination of the LOS and of the magnetic axis with respect to the rotation one.
Some insight can also be obtained for the extension of the region of emission, as was shown by considering different apertures of the equatorial belt in magnetic colatitude and in azimuth. Specifically, the case of an equatorial belt of 45° of semi-aperture showed a decrease in the polarization degree ($\Pi_L < 0.05$) for the condensed surface, with respect to the configuration where the same angles χ and ξ were considered and the semi-aperture of the belt was of 18°.

A further analysis was done on the effect of QED on the properties of the emitted radiation, noticeable in particular in the behaviour of the polarization degree. In all the cases considered for the emission model, neglecting the effects of QED resulted in a lowering of Π_L, as explained in Section 3.2.

Possible future studies should address in more detail the effect of QED phenomena on the properties of the polarization of emission. In particular, the geometrical depolarization becomes more relevant as the extension of the emitting region increases, so that the effect of QED is stronger in keeping an appreciable polarization fraction at the observer: it could then be of interest to study the relevance of the QED effects as a function of the extension of the region. Additional studies, complemented with data taken with X-ray polarimeters (e.g. IXPE), could therefore provide a test of QED predictions.
In this work, an equatorial belt was taken as the only emitting region from the source: other examples could be investigated, considering polar caps or more complicated configurations. Also, the atmospheric model has been neglected here for simplicity, but more extended analyses could take into account the presence of both a condensed surface and an atmospheric layer, which is likely the case for many sources. Finally, a purely dipolar magnetic field has been considered in this study: further works could include the presence of more complicated magnetic field topologies.
In conclusion, IXPE has made it possible to study polarization between 2 and 8 keV, so future missions, built with different technologies, could explore energy ranges for which no polarimetric measurements have been performed yet, specifically below 2 keV: at these lower energies, the condensed surface is characterized by interesting properties of the polarization observables, e.g. the mode switching, and further studies in this energy range could shed more light on these behaviours.

References

[1] W. Baade and F. Zwicky. Remarks on Super-Novae and Cosmic Rays. *Physical Review*, 46(1):76–77, July 1934.

[2] A. Y. Potekhin, A. De Luca, and J. A. Pons. Neutron Stars—Thermal Emitters. , 191(1-4):171–206, October 2015.

[3] J. Park, C. Kim, J. Woo, H. An, K. Mori, S. P. Reynolds, and S. Safi-Harb. X-Ray Studies of the Pulsar PSR J1420-6048 and Its TeV Pulsar Wind Nebula in the Kookaburra Region. , 945(1):33, March 2023.

[4] M. A. McLaughlin, A. G. Lyne, D. R. Lorimer, M. Kramer, A. J. Faulkner, R. N. Manchester, J. M. Cordes, F. Camilo, A. Possenti, I. H. Stairs, G. Hobbs, N. D'Amico, M. Burgay, and J. T. O'Brien. Transient radio bursts from rotating neutron stars. , 439(7078):817–820, February 2006.

[5] S. A. Olausen and V. M. Kaspi. The McGill Magnetar Catalog. , 212(1):6, May 2014.

[6] A. I. Ibrahim, C. B. Markwardt, J. H. Swank, S. Ransom, M. Roberts, V. Kaspi, P. M. Woods, S. Safi-Harb, S. Balman, W. C. Parke, C. Kouveliotou, K. Hurley, and T. Cline. Discovery of a Transient Magnetar: XTE J1810-197. , 609(1):L21–L24, July 2004.

[7] A. Y. Potekhin, J. A. Pons, and D. Page. Neutron Stars—Cooling and Transport. , 191(1-4):239–291, October 2015.

[8] L. Ferrario and D. Wickramasinghe. Modelling of isolated radio pulsars and magnetars on the fossil field hypothesis. , 367(3):1323–1328, April 2006.

[9] R. Turolla, S. Zane, and A. L. Watts. Magnetars: the physics behind observations. A review. *Reports on Progress in Physics*, 78(11):116901, November 2015.

[10] A. K. Harding and D. Lai. Physics of strongly magnetized neutron stars. *Reports on Progress in Physics*, 69(9):2631–2708, September 2006.

[11] D. G. Yakovlev and C. J. Pethick. Neutron Star Cooling. , 42(1):169–210, September 2004.

[12] D. De Grandis, R. Turolla, R. Taverna, R. Lucchetta, T. S. Wood, and S. Zane. Three-dimensional Magnetothermal Simulations of Magnetar Outbursts. , 936(2):99, September 2022.

[13] R. C. Duncan and C. Thompson. Formation of Very Strongly Magnetized Neutron Stars: Implications for Gamma-Ray Bursts. , 392:L9, June 1992.

[14] V. M. Kaspi and A. M. Beloborodov. Magnetars. , 55(1):261–301, August 2017.

[15] C. Thompson, M. Lyutikov, and S. R. Kulkarni. Electrodynamics of Magnetars: Implications for the Persistent X-Ray Emission and Spin-down of the Soft Gamma Repeaters and Anomalous X-Ray Pulsars. , 574(1):332–355, July 2002.

[16] M. Lyutikov and F. P. Gavriil. Resonant cyclotron scattering and Comptonization in neutron star magnetospheres. , 368(2):690–706, May 2006.

[17] R. Taverna, F. Muleri, R. Turolla, P. Soffitta, S. Fabiani, and L. Nobili. Probing magnetar magnetosphere through X-ray polarization measurements. , 438(2):1686–1697, February 2014.

[18] D. Lai. Matter in strong magnetic fields. *Reviews of Modern Physics*, 73(3):629, July 2001.

[19] A. Y. Potekhin. Atmospheres and radiating surfaces of neutron stars. *Physics Uspekhi*, 57(8):735–770, August 2014.

[20] A. K. Harding. Physical Processes in Strong Magnetic Fields of Neutron Stars. In G. Cusumano, E. Massaro, and T. Mineo, editors, *Pulsars, AXPs and SGRs Observed with BeppoSAX and Other Observatories*, pages 127–138, July 2003.

[21] Z. Medin and D. Lai. Condensed surfaces of magnetic neutron stars, thermal surface emission, and particle acceleration above pulsar polar caps. , 382(4):1833–1852, December 2007.

[22] R. Taverna, R. Turolla, V. Suleimanov, A. Y. Potekhin, and S. Zane. X-ray spectra and polarization from magnetar candidates. , 492(4):5057–5074, March 2020.

[23] Z. Medin and D. Lai. Density-functional-theory calculations of matter in strong magnetic fields. II. Infinite chains and condensed matter. , 74(6):062508, December 2006.

[24] M. van Adelsberg, D. Lai, A. Y. Potekhin, and P. Arras. Radiation from Condensed Surface of Magnetic Neutron Stars. , 628(2):902–913, August 2005.

[25] L. Nobili, R. Turolla, and S. Zane. X-ray spectra from magnetar candidates - II. Resonant cross-sections for electron-photon scattering in the relativistic regime. , 389(2):989–1000, September 2008.

[26] R. Taverna, R. Turolla, D. González-Caniulef, S. Zane, F. Muleri, and P. Soffitta. Polarization of neutron star surface emission: a systematic analysis. , 454(3):3254–3266, December 2015.

[27] A. Y. Potekhin, V. F. Suleimanov, M. van Adelsberg, and K. Werner. Radiative properties of magnetic neutron stars with metallic surfaces and thin atmospheres. , 546:A121, October 2012.

[28] S. Zane and R. Turolla. Unveiling the thermal and magnetic map of neutron star surfaces though their X-ray emission: method and light-curve analysis. , 366(3):727–738, March 2006.

[29] R. Turolla, S. Zane, and J. J. Drake. Bare Quark Stars or Naked Neutron Stars? The Case of RX J1856.5-3754. , 603(1):265–282, March 2004.

[30] J. F. Pérez-Azorín, J. A. Miralles, and J. A. Pons. Thermal radiation from magnetic neutron star surfaces. , 433(1):275–283, April 2005.

[31] V. Suleimanov, V. Hambaryan, A. Y. Potekhin, M. van Adelsberg, R. Neuhäuser, and K. Werner. Radiative properties of highly magnetized isolated neutron star surfaces and approximate treatment of absorption features in their spectra. , 522:A111, November 2010.

[32] D. Page and A. Sarmiento. Surface Temperature of a Magnetized Neutron Star and Interpretation of the ROSAT Data. II. , 473:1067, December 1996.

[33] G. G. Pavlov and V. E. Zavlin. Polarization of Thermal X-Rays from Isolated Neutron Stars. , 529(2):1011–1018, February 2000.

Ringraziamenti

Il primo dovuto ringraziamento va al Professore Roberto Turolla e al Professore Roberto Taverna per il loro indispensabile supporto e per avermi seguita in modo costante in questi sei mesi di lavoro.

Un altro doveroso ringraziamento va alla Prof. Rossit, che con la sua preziosa dedizione per l'insegnamento mi ha trasmesso la passione per le materie scientifiche, e senza la quale non avrei mai intrapreso questa strada.

Grazie a tutta la mia famiglia per il loro entusiasmo e per avermi fatto sempre sentire la loro vicinanza.

Grazie a tutti gli amici.
Alle amiche di una vita, Giulia e Anna, che in un modo o nell'altro hanno fatto costantemente parte della mia vita.
Alle amiche del liceo, che sono diventate tra le persone più care. Stefania, con cui ho condiviso mille avventure e che è stata un punto di riferimento negli ultimi anni: grazie per avermi sempre spronata ad essere la migliore versione di me. Alessia e Sofia, le mie SDM, che dalla prima superiore sono parte essenziale della mia vita: grazie per i ricordi che abbiamo costruito in questi dieci anni di amicizia, per tutti i viaggi e tutti i pasti che abbiamo condiviso.
A tutti i coinquilini e i compagni di università che, chi più e chi meno, hanno percorso con me parte di questo viaggio, per aver reso un po' più affrontabili anche i momenti meno sereni.

Grazie a mamma e papà, per essermi stati accanto amorevolmente, per aver sempre sostenuto le mie scelte e per tutti i preziosi consigli, di cui, anche quando non sembrava, ho sempre fatto tesoro.
A mio fratello, per essere sempre stato, forse anche inconsciamente, un modello da seguire.
Ad Alessia, per essere stata la più preziosa aggiunta a questa famiglia e per il suo incondizionato affetto nei miei confronti.

Grazie a Caby, che è stata al mio fianco da che ne ho memoria e che è di fatto parte della famiglia. Grazie per essere la persona che più mi capisce e per essere il mio porto sicuro in ogni momento in cui ne ho bisogno.